2022

Investigation of Geomechanical Behavior of Laminated Rock Mass Through Experimental and Numerical Approach

Qingwen Shi
West Virginia University, qs0003@mix.wvu.edu

INVESTIGATION OF GEOMECHANICAL BEHAVIOR OF LAMINATED ROCK MASS THROUGH EXPERIMENTAL AND NUMERICAL APPROACH

Qingwen Shi

Dissertation submitted to the
Benjamin M. Statler
College of Engineering and Mineral Resources
West Virginia University
In partial fulfillment of the requirements
for the degree of

Doctor of Philosophy
in
Mining Engineering

Brijes Mishra, Ph.D., Chair
Ihsan B. Tulu, Ph.D.
Hassan Amini, Ph.D.
Department of Mining Engineering
West Virginia University

Bruce S. Kang, Ph.D.
Department of Mechanical & Aerospace Engineering
West Virginia University

G.S. Esterhuizen, Ph.D.
Office of Mine Safety and Health Research
National Institute for Occupational Safety and Health

Morgantown, West Virginia
April 2022

Keywords: Laminated rock, roof failure, geomechanical behavior, biaxial and triaxial test, synthetic laminated rock, lamination properties, DEM-FDM coupling

ABSTRACT

Investigation of Geomechanical Behavior of Laminated Rock Mass Through Experimental and Numerical Approach

Qingwen Shi

Roof failure in the Appalachian underground coal fields occurs often in laminated shale. Laminated shale roof in coal mines fails in unique ways, such as cutter failure or delamination failure. Extensive studies have investigated the influential factors that cause laminated roof failure, which include in-situ stress, entry layout, roof span, and roof support. However, cutter failure continues to occur frequently and erratically. This is due to the lack of in-depth understanding of the inherent properties of the laminations, such as bedding plane strength, matrix strength, and bedding plane spacing, which in turn influence the geomechanical behavior of the laminated rock. These inherent properties vary and are therefore the significant factors influencing entry and support design. The objective of this dissertation is to discover the effect of lamination properties on the geomechanical behavior of laminated rocks through experimental and numerical analysis.

The experimental approach included the development of synthetic laminated rock (SLR). The SLR included three different cohesive strengths (C_p). This research conducted biaxial tests and triaxial tests on the cubic laminated rock with a special platen. We analyzed the strength, failure mode, and deformation of laminated specimens with various C_p under varied stress conditions. The experimental results showed that C_p significantly influenced the SLR strength, modulus, and failure modes in biaxial stress conditions. Application of confining stress reduced the damage of SLR specimens and constrained the effect of C_p on SLR behavior. The results from the tests on SLR supported the development of a series of numerical models of underground coal mines with laminated roof. To simulate the laminated roof at different scales, this research used FLAC3D based on the finite difference method (FDM) and PFC3D based on the discrete element method (DEM).

Next, this research developed the coal mine entry model with the laminated roof in the PFC program using laboratory data and investigated the effect of bedding plane spacing, bedding plane strength, and support pressure on roof stability. The results from the numerical analysis showed that the roof stability and stress magnitude inside the roof increased with both bedding plane

spacing and bedding plane strength, and this effect was sensitive to these two properties. PFC then modeled the delamination process of laminated rock under various stress conditions. The results demonstrated that the delamination of an unconfined laminated rock initiates in the inner section of the bedding. Cutter failure initiated with damages that distributed extensively in the roof. We then developed a panel scale longwall model in PFC3D which was then coupled with FLAC3D for analyzing crack propagation in roof as well as understanding large scale failure behavior. Numerical results from the FLAC3D-PFC3D coupled model showed that the bedding plane strength significantly influenced the roof deformation and also modified the fracturing mechanism of the laminated roof. These effects are sensitive to the extraction activity of the entries and panels. These findings will advance knowledge on laminated roof failure and improve entry and support design.

Keywords: Laminated rock, roof failure, geomechanical behavior, biaxial and triaxial test, synthetic laminated rock, lamination properties, DEM-FDM coupling

ACKNOWLEDGEMENT

I would like to thank all the people who have contributed to the initiation and completion of my doctoral study. It was their help that made the completion of this dissertation possible.

Firstly, I would like to express my sincere gratitude to my advisor Dr. Brijes Mishra for his continuous support of my doctoral research, both financially and academically. Dr. Mishra has been a mentor and also a friend throughout my doctoral study. He showed great patience and provided valuable advice on my research. I would like to thank him for his guidance and support during my research at West Virginia University.

I would like to thank my committee members Drs. Ihsan Berk Tulu, Hassan Amini, Bruce Kang, and G.S.(Essie) Esterhuizen for their insightful comments and invaluable suggestions. I would like to express my special thanks to Dr. G.S.(Essie) Esterhuizen for providing valuable field data to verify our coupling models. I would also like to thank Dr. Yi Luo, although he is no longer with us, for his help in revising my research proposal. I appreciate the valuable time they have spent on my graduate committee.

This work was performed under a project funded by the National Institute for Occupational Safety and Health (NIOSH). I would like to thank them for their support and funding.

I would like to thank my friends and colleagues at the Department of Mining Engineering at WVU.

Additionally, I would like to thank Karen Centofanti and Genette Chapman for providing administrative support throughout my time at WVU.

Finally, I would like to thank my parents, sister, and brother for their endless love and constant support. Thanks to my nephews and nieces for encouraging me frequently online.

Thanks for all your support and encouragement!

Table of Contents

List of Figures

Chapter 1

Chapter 2

Chapter 3

Chapter 4

Chapter 5

Chapter 6

List of Tables

Chapter 3

Chapter 4

Chapter 5

Chapter 6

CHAPTER 1 INTRODUCTION

1.1 Introduction

Roof falls have historically been a leading hazard for underground coal mining industries, accounting for nearly 33% of all fatalities in underground coal mines as shown in Fig. 1- 1 (Centers for Disease Control and Prevention, 2021). Although the fatalities dropped significantly in recent years due to the mechanization and utilization of roof bolts (Mark et al., 2020), as shown in Fig. 1- 2, roof and rib falls were still responsible for 94 underground fatalities from 2000 to 2019, more than all other causes combined. These roof and rib fall accidents pose great safety threats to workers, mining equipment, and production plans.

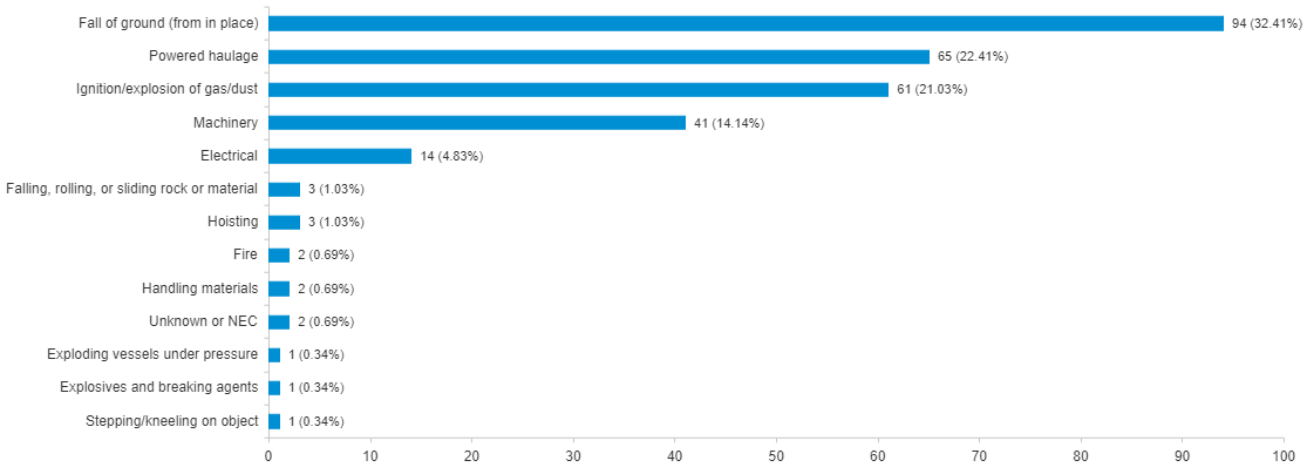

Fig. 1- 1 Number and percentage of fatalities by accident class at underground mining locations, 2000-2019 (Centers for Disease Control and Prevention, 2021)

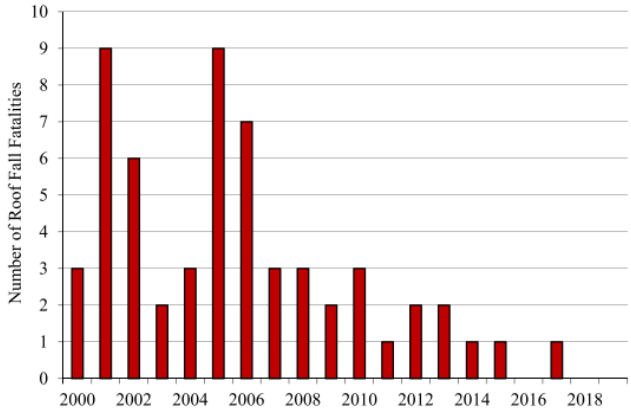

Fig. 1- 2 Two decades of roof fall fatalities in US coal mines (Mark et al., 2020)

In the past decades, studies have investigated the influential factors of roof fall, such as in-situ stress, entry layout, and surrounding rock properties; these studies have utilized various techniques,

including empirical observation, theoretical analysis, numerical modeling, and laboratory tests. However, when it comes to particular geological conditions, such as entries with laminated roof, the efficiency of ground control practice is limited.

Appalachian coal mines in the Pittsburgh coal seam that experience roof fall are mostly characterized by laminated shale roofs (Shi and Mishra, 2020). Fig. 1- 3 shows that the Illinois Basin and Central/Northern Appalachian regions have the highest non-injury roof fall rates. With multiple parallel bedding planes, the shale roof frequently presents a particular mode of failure, known as kink or cutter roof failure. Fig. 1- 4 shows cutter failure caused by the laminated roof. Cutter failure has also caused numerous fatalities in the underground mining industry (Esterhuizen and Bajpayee, 2012; Hill, 1986; Kuznetsov and Trofimov, 2012; Molinda and Mark, 2010; Murphy, 2016; Xue and Mishra, 2017). Historically, cutter roof failure occurred in each of the major coal basins of the United States that practiced underground mining (Hill, 1986). The weak roof in these coal mines consisted primarily of shale. Stack rocks are also common in coal measures strata in southern West Virginia. These rocks share similar structures and geological behaviors, as they belong to the laminated rock mass. It is imperative to investigate the geomechanical behavior of laminated surrounding rock of underground entries to provide basic guidance for entries and support system design. However, multiple research questions concerning laminated rock/roof failure remain unsolved:

- The influence of lamination properties on the laminated rock failure when subjected to various stress conditions
- The delamination failure process of the laminated rock in various stress conditions
- The influence and sensitivity of longwall panel extraction on the laminated roof failure

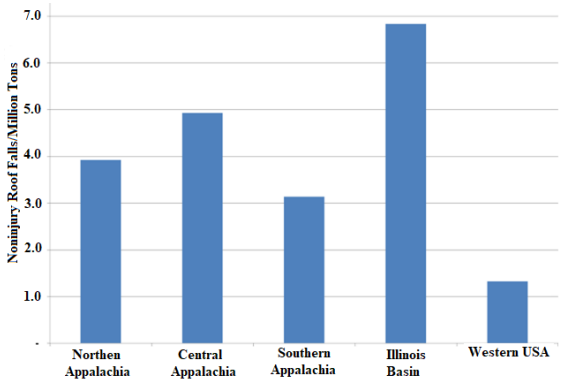

Fig. 1- 3 Non-injury roof fall rates by US region from 1983 to 2013 (Murphy, 2016)

Fig. 1- 4 Cutter roof failure of shale roof (Molinda and Mark, 2010; Murphy, 2016)

1.2 Research questions

Cutter roof failure occurs with crushing or local buckling of thinly laminated roof beds near the corners of excavation as shown in Fig. 1- 5 (Gao and Stead, 2013; Hill, 1986). The failure usually initiates at the roof-rib section and develops upward through the laminated roof with an angle greater than 60° (Esterhuizen and Bajpayee, 2012), shown in Fig. 1- 5a. In addition, delamination failure occurs when the bedding planes are extremely weak. The laminated roof fractures into layers and bedding separations occur, as shown in Fig. 1- 5b. The delamination develops at various depths and separated roof rocks continue to bend under gravity until the cutter roof failure finally occurs. In these circumstances, the support system fails frequently even if designed with extreme caution. The frequent failure is attributed to our poor understanding of several key research questions, including the effect of the bedding plane's properties, delamination process, and excavation-caused abutment stress.

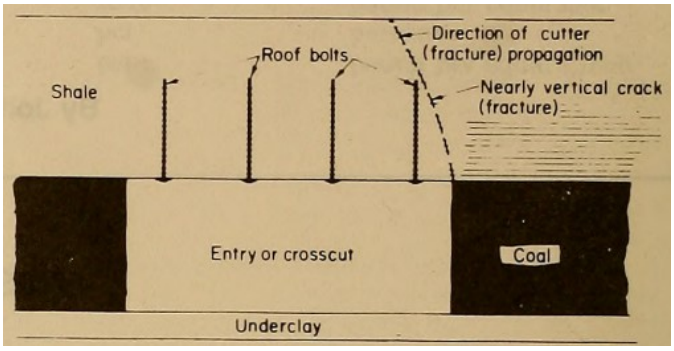

a. Initial cutter roof failure

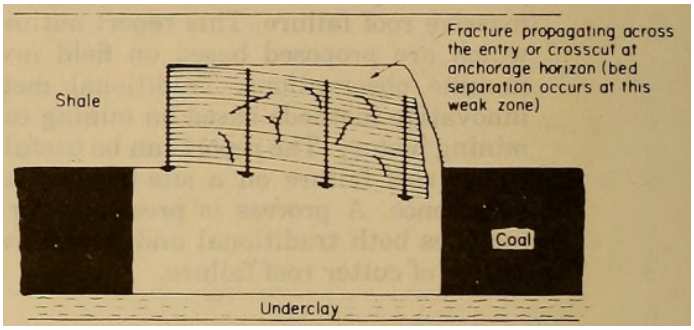

b. Propagation of cutter roof failures

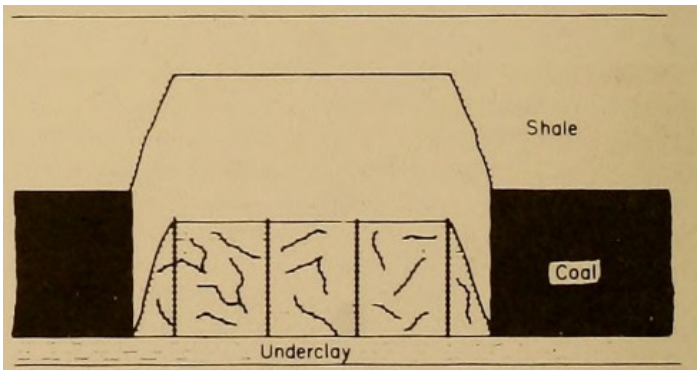

c. Cutter fail

Fig. 1- 5 Cutter roof failure sequence (Hill, 1986)

First, the bedding planes introduce special failure characteristics of laminated rocks, but the detailed effect of bedding plane properties is still unclear. Shale roof rock is a typical laminated rock and studying shale roof stability starts from the basic understanding of lamination failure. Previous studies recognized that the lamination properties determined the strength and fracturing behavior of laminated rocks, both theoretically (Jaeger, 1960a; Jaeger et al., 2009) and experimentally (Bai and Tu, 2020; Chong et al., 2017; Tan et al., 2015). Field observation also noticed that the anisotropy introduced by bedding planes poses a significant effect on the stability of large-scale laminated rock mass. For instance, researchers have widely adopted coal mine roof rating (CMRR), an index for evaluating jointed rock in US coal mines, for providing basic information on laminated rock supporting system design (Mark and Molinda, 2007). Despite these efforts to understand the anisotropy of laminated rock, laminated rock failure still occurs frequently. This is likely because our current knowledge of laminated rock is still unable to reflect their failure mechanisms, since the fundamental role of bedding planes in determining lamination failure is still obscure. For example, the theoretical Jaeger's Plane of Weakness model (Jaeger, 1959, 1960b; Jaeger et al., 2009) turned out to be incapable of reflecting real cases of how bedding plane strength affects rock mass strength (Park et al., 2018).

Second, delamination occurs in the underground entry roof when the bedding planes are extremely weak. In-depth observation of the delamination process before failure is necessary to guide for controlling this failure pattern. Nevertheless, this is difficult to achieve in the field due to the lack of effective methods. Researchers have regularly used Brazilian tests in the laboratory to study the damage characteristics of laminated rocks (Bai and Tu, 2020; Chong et al., 2017; Tan et al., 2015). In Brazilian tests, the laminated rocks have unconstrained sides which makes it easier for observing failure. These attempts recognized that the failure occurs predominantly along the weak bedding planes. However, it is difficult to explain laminated roof failure problems using the Brazilian test since the stress environment of a Brazilian splitting test is different from that of a laminated roof. Triaxial tests on laminated rocks can better reproduce the stress conditions under which the underground laminated roof fails. Because the experimental process is encapsulated by the triaxial cell, researchers have never observed the propagation of inner cracks. This demonstrates the necessity of a comprehensive study on the delamination behavior of laminated rocks in different stress conditions.

Finally, instead of staying in an unchanged in-situ stress environment, laminated roofs in underground coal mines normally experience multiple different stress conditions (Esterhuizen et al., 2019; Esterhuizen and Bajpayee, 2012; Shi et al., 2021). For instance, laminated rock mass in entry roofs in longwall coal mines normally experience in-situ stresses, entry advance-caused stresses, and multiple panel extraction-caused stresses in sequence. The changing stress introduces a cycling loading and unloading stress condition to the laminated roof rock, which could pose an effect on the failure mechanism and delamination process of the laminated roof rock. Replicating these changing stress conditions in the laboratory is difficult, and therefore researchers have not yet studied the effect of the changing stress conditions and the sensitivity of the lamination to this effect.

1.3 Objectives

The main objective of this research is to understand the fundamental mechanism behind the failure of laminated rock using experiments and numerical approaches. The results from this research aim to provide an in-depth understanding of the laminated roof failure in underground coal mines which will improve mine health and safety. This research accomplished these broader objectives using the following set of detailed tasks.

First, this research investigated the effect of bedding plane properties on the failure behavior of laminated rock with an experimental method, paying particular attention to the bedding plane strength. In this task, we fabricated synthetic laminated rock in the laboratory and varied the bedding plane strength. We then observed the failure behavior, including failure strength, failure model, and deformation characteristic, of the synthetic laminated rocks with different bedding plane strengths in comparison. The specially designed platen then replicated the stress conditions similar to excavation-caused stress. This task then investigated the sensitivity of the effect of bedding plane strength by comparing failure behavior variation under different loading conditions. This task also included an extension to similar research on a numerical laminated entry roof. It also implemented a study of the effect of bedding plane strength on roof response in a numerical entry model.

The second task focused on studying the delamination process of laminated rock by a numerical approach. This task investigated cracking propagation in numerical laminated rocks under unconfined compressive stress, confined compressive stress, and stress conditions similar to those experienced by the entry roof. We then compared the delamination process under various stress conditions with field observation and reported data.

The final task investigated the laminated roof response with different bedding plane strengths as it experienced entry advancing and multiple panel extraction with a coupling numerical method. This task included the creation of a large-scale model, including two longwall panels, two yield pillars, and one abutment pillar, using a coupling finite difference and discrete element method for the first time; it also included a comparison of the numerical results to those observed in a US coal mine. We captured the large-scale panel extraction and micro-cracking process of the laminated roof simultaneously with an affordable computational cost.

1.4 Outline of the dissertation

To achieve the objectives discussed above, the following five chapters contain the research work of this dissertation.

The second chapter presents the literature review incorporating topics related to the research questions, such as general shale rock failure, laminated roof failure in underground coal mines, delamination and fracturing process of laminated rocks, and investigation of the effect of lamination properties, to determine the current research status in these areas. The summary

following the review discusses the research methods that the present study can adopt and the gap between previous studies and practical applications.

The third chapter contains the study of the effect of lamination properties on the geomechanical behavior of laminated rock subjected to various stress conditions in the laboratory. This study particularly focuses on the effect of bedding plane strength. This involved fabricating synthetic laminated rocks (SLR) with different bedding plane strengths and developing a loading platen capable of applying biaxial and triaxial tests on the specimens, as well as comparing the failure characteristics. The obtained test results demonstrate that bedding plane strength poses a significant effect on the geomechanical behavior of the SLR and that this effect is stress condition dependent.

The fourth chapter extends the laboratory scale to an entry scale study that varied lamination properties, including bedding plane strength, bedding plane spacing, and cohesion-to-tension ratio, in order to observe their effect on the laminated roof stability. This study adopted DEM. This study established the entry model based on laboratory test data on actual shale and validated it by comparing laminated roof failure and intact roof failure based on empirical observations. The simulation results show the pronounced influence of the lamination properties on the laminated roof. In addition, the simulation applied the supporting pressure to the roof line. The results signify that the effect of lamination properties on roof stability depends on the support pressure.

The fifth chapter is the numerical study of fracturing behavior and delamination process of laminated rock incorporating weak bedding planes. This study created bonded particle material (BPM) based on laboratory test results, including compressive results of brittle rock and direct shear results of extremely weak bedding planes. This study conducted all tests in laboratory-scale models, adapting different loading paths to apply unconfined compressive stress along the bedding planes respectively and analyzing their delamination process in comparison. Then, this study simulated models with different stress conditions to observe the delamination process, including unconfined and confined compressive models and unsupported roof models. Numerical models show important characteristics that cannot be observed in the field. Overall, the stress magnitude that causes delamination differs with stress conditions and loading path. Delamination process observation shows that it begins on the inside beddings instead of the outer, and it propagates and connects gradually until a massive failure occurs.

The sixth chapter contains a large-scale modeling investigation to consider the panel extraction-caused abutment pressure and its effect on the interaction between lamination properties and roof stability. For the first time, this research used the DEM-FDM coupling method for simulating longwall panel extraction-caused roof stability problems. We compared different coupling strategies based on a uniaxial compressive test on sandstone to find an appropriate strategy for large-scale modeling. This study created the laminated roof with a transversely isotropic material using PFC3D, while simulating the rest of the model using FLAC3D, including overburden competent roof, longwall panels, and floor. This study validates the numerical coupling model by showing a good match with field observation in a US coal mine. By varying the bedding plane properties such as bedding plane strength and cohesion-to-tensile ratio, this study can observe their effect on the laminated roof stability. We then compared this effect in different stress conditions introduced by the development of entries, single panel extraction, and double panel extraction respectively.

Finally, the closing summary includes the overall conclusions of the research and possibilities for future study.

CHAPTER 2 LITERATURE REVIEW

This research addresses various rock mechanics problems, including the effect of lamination properties, delamination process, and sensitivity of the effect of lamination properties to abutment pressure in underground coal mines. This chapter discusses and summarizes previous studies on these topics.

For decades, studies have investigated laminated roof failure as a primary cause of underground roof falls from an in-situ stress point of view. Various methods, such as case studies, numerical models, and laboratory tests, have researched the failure mechanism, influential factors, and prevention methods. These studies have discovered important clues concerning this topic. These conclusions are still applicable to the laminated rock behavior in underground coal mines and are thus reviewed first.

Understanding laminated roof failure starts by investigating the fundamental failure mechanism of laminated rock or similar laminated materials. In addition to underground mining, researchers focusing on civil or petroleum implemented significant studies related to shale or other laminated rocks with various methods, including laboratory tests, numerical simulations, and theoretical analysis. These studies have reported important findings on the laminated rock failure mechanism and the sensitivity to stress conditions. These findings shed light on investigating the effect of bedding plane strength and are discussed in Section 2.2.

In addition, the laminated rock failure involves crack propagation. Studying the cracking process and characteristics helps to reveal the mechanism of rock failure. Though observing crack propagation in the field is difficult, researchers developed multiple strategies to study this topic in the laboratory and numerical models. The strategies and findings benefit our efforts to observe the delamination process of laminated rock and laminated roofs in the field. Section 2.3 summarizes reported research concerning this topic.

Coal extraction-caused abutment stress poses a changing stress condition for laminated roofs. Studying the effect of the changing stress condition on laminated roof failure and its interaction with lamination properties requires a large-scale model while focusing on roof crack propagation simultaneously. Coupling the finite difference method and discrete element method provides an ideal tool for this topic. Section 2.4 reviewed previous research on the application of this method.

2.1 Laminated roof failure in Underground Coal Mines

Bajpayee et al. (2014) compiled data from approximately 11,600 noninjury roof fall incidents reported to MSHA (Mine Safety and Health Administration) by more than 800 mines from 1999 through 2008. The analysis showed that laminated roof significantly affected roof failure in underground coal mines. Researchers have developed several approaches in the past to reduce roof failure, which included field observations, laboratory tests, numerical simulations, and theoretical analysis. Based on these efforts, researchers successfully used the orientation of mine layout, panel orientation, cable bolts, and cribs to mitigate roof failure in coal mines.

Researchers have observed cutter roof failure, a typical laminated roof failure in underground entries, in underground engineering as early as the 1940s. Roley (1948) provided the first well-reported cutter roof failure. Roley termed the cutter roof failure as "pressure cutting" and described the characteristics of this fall based on cutter failure cases in the Illinois Basin in the United States. Since then, there have been increasing reports of cutter roof failure cases worldwide (Aggson, 1978; Bauer, 1990; Mark, 1991a, 1991b; Mark et al., 2004a; Mark and Molinda, 1994; Su and Peng, 1987; Wang et al., 1974). Canada, India, and the United Kingdom have also reported cutter roof failure (Barron and Baydusa, 1999; Jeremic, 1981; Kent et al., 1998; Kushwaha et al., 2003; Meyer et al., 1999; Sheorey, 1994). In most of the literature, in-situ stress was the main influential factor that triggered cutter roof fall under certain conditions. Researchers developed several control methods to mitigate cutter failure.

Hill (1986) defined cutter roof failure as follows: "Cutter roof failure in mine roof rock is a failure process that initially begins as a fracture plane in the roof rock parallel to, and located at, the roof-rib intersection," and "the fracture propagates upward into the roof over the mine opening at an angle usually steeper than 60° from the horizontal." Su and Peng (1987b) investigated the mechanism behind cutter roof failure through a case study, laboratory investigation, and numerical modeling. They concluded that high vertical stress associated with thick overburden along with a directional horizontal stress field was responsible for a series of cutter roof failures in the longwall development entries. Molinda and Mark (2010) pointed out that the cutter roof is a compression failure. Esterhuizen and Bajpayee (2012) looked at the laminated roof as a beam with a typical beam theory. Their results demonstrated that the confining pressure contributed to constraining roof failure by acting as minor principal stress. Esterhuizen and Bajpayee (2012) also numerically

demonstrated that the existence of lamination changed the minor principal stress distribution and consequently caused cutter roof failure, as shown in Fig. 2- 1. In addition, they found that the interface properties affected the failure mode of the laminated roof directly. Their numerical simulation results showed that typical cutter failure occurs under low strength/low stiffness interfaces. Inclined shear planes predominately occur when the interface strength/stiffness increases.

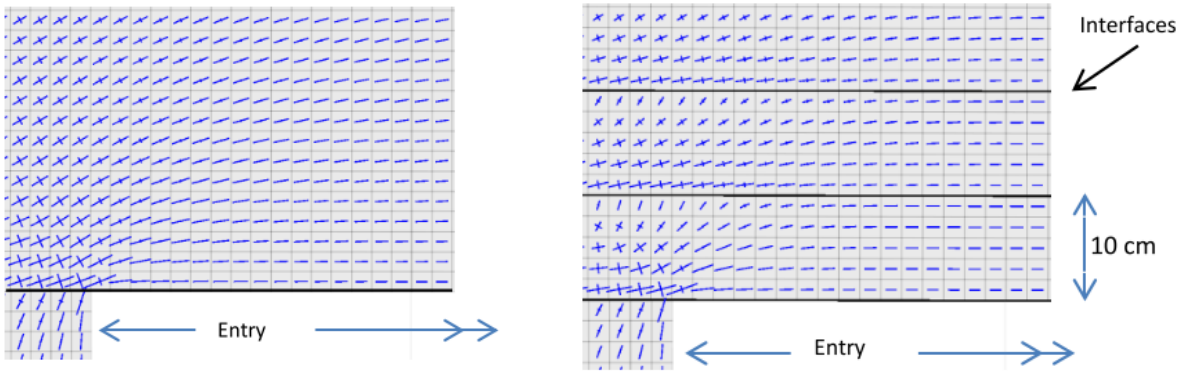

(a) Massive roof (b) Laminated roof

Fig. 2- 1 Change in stress orientation and magnitude caused by the presence of lamination interfaces near the corner of an entry (Esterhuizen and Bajpayee, 2012)

Previous studies have used numerous approaches to study failure in laminated roof fall. Hill (1986) considered the shape and size of openings, in-situ stress, and bedding roof stiffness as the influential factors of cutter roof failure. Gao and Stead (2013) simulated cutter failure using bonded particle material (BPM). They demonstrated that the smooth joint model in PFC3D has the capacity to simulate bedding planes in the laminated roof. Garg (2018) simulated the effect of bedding thickness on roof deflection with FLAC2D. He found that the decrease in bedding thickness reduces the overall bending stiffness of the roof beam and therefore results in tensile failure at the top corner of each layer. Mark (2004b) stated that cutters or kink zones often occurred in the advancing face. In addition, this case study indicated that the thickness of the shale roof and the overlying sandstone roof affect the roof fall rate. Using numerical simulation, Bai and Tu (2020) showed that bedding planes and vertical joints governed the progressive failure of the laminated and jointed roof.

In addition to the optimization of the layout of entries and panels, primary and secondary support served as the main method of controlling roof fall. Mark (2004b) found that flexure of the outer layers of the roof can reduce the effectiveness of roof bolts. Skin control with mesh (or even straps

or large plates) can therefore reduce the number of roof falls while also protecting miners from falling rock. Esterhuizen and Bajpayee (2012, 2017) argue that support pressures would have to be impractically high to prevent horizontal stress-related damage to the laminated roof rocks. Ghabraie et al. (2013) studied the mechanism of truss bolt systems and showed that this type of support reduces the horizontal movement of rock layers and prevents shear crack propagation by repositioning the natural reinforced arch and reducing the area of loosened rock above the roof. Abousleiman et al. (2020) conducted a sensitivity analysis of influential factors of the self-stability of the bedded roof using UDEC. They showed that the self-supporting capacity is influenced by entry depth and fine-scale bedding. In addition, intact material properties such as stiffness and strength also affect the self-supporting capacity. Bai and Tu (2020) numerically validated the effect of confinement provided by roof skin support with a metal mesh to restrict progressive spalling in a laminated roof.

From the literature review, we conclude that various factors affect laminated roof stability, such as in-situ stress, rock properties, lamination properties, and support systems. However, research efforts have not been directed towards understanding the lamination properties themselves. Therefore, it is imperative to investigate the influence of lamination properties on roof stability. Studies have used various research methods including theoretical analysis, laboratory testing, field observation, and numerical models to study the mechanism and prevention of laminated roof falls.

2.2 Laminated rock (shale) failure

Various types of rocks can be categorized as laminated rocks, such as slate, shale, gneiss, and graphitic schist. Both laboratory tests and numerical simulations have investigated the effect of the bedding plane orientation on the anisotropy and strength of shale. Researchers conducted these investigations mostly through indirect tensile strength and compressive strength tests. Their results showed that the orientation of the weak bedding planes has a large effect on both fracture propagation and strength of the shale specimens (Dou et al., 2019a; Heng et al., 2015; Sherizadeh and Kulatilake, 2016; Tan et al., 2015; Yang et al., 2019). Morgan and Einstein (2014) conducted uniaxial compression tests on Opalinus shale with flaw pairs under different bedding plane inclinations. They found that crack propagation involved tensile cracks and shear cracks along the bedding planes in the shale. Loong et al. (2013) simulated the effect of a single joint angle under uniaxial and triaxial compression with 3DEC. Their results were in good agreement with the

theoretical results (Swift and Reddish, 2005) and validated the feasibility of using DEM to investigate the jointed rock mass. Oh et al. (2017) studied the effect of inclination on shear strength and failure mode in a direct shear test. Chong et al. (2017) studied the sensitivity of the effect of bedding plane properties on the fracturing behavior of shale with different bedding plane orientations using PFC2D. They utilized a smooth joint model in PFC, and their results show that bedding plane strength affects the shale strength while the shear-to-tensile strength ratio controls the failure pattern. Feng et al. (2020) experimentally studied the mechanical behavior of a shale disc in the indirect tensile test under different bedding plane orientations and various loading rates. They defined the ability of shale to resist elastic deformation as Brazilian split modulus and the applied energy to a shale sample until its failure as the absorbed energy. Their results showed that both the split modulus and the absorbed energy had the minimum values when the inclination equaled 45°, and indirect tensile strength, split modulus, and absorbed energy of shale gradually increased with the increase in loading rate.

Researchers have also reported the effect of weak plane mechanical parameters with numerical methods. For example, Lambert and Coll (2014) assessed the shear strength of a weak plane using numerical models that included joints with weak plane surface asperities and shape with the smooth-joint contact model in PFC. Yang et al. (2019) and Dou et al. (2019) conducted parametric studies on Brazilian test discs and three-point flexural test blocks, respectively. Their results showed the importance of interlayer strength on the anisotropic behavior of the shale. Sherizadeh and Kulatilake (2016) used 3DEC to assess the effect of bedding plane parameters on roof performance, such as the intensity of shear and tensile failures along bedding planes. Chong et al. (2017) used numerical models and found that the ratio of cohesion to the tensile strength of smooth joints mainly affects the number of cracks formed leading to different failure modes (He et al., 2018; Heng et al., 2015; Jia et al., 2017).

Previous researchers have also used synthetic rocks for investigating the behavior of laminated rocks. Einstein and Hirschfeld (1973) tested gypsum plaster models with a single joint and multiple joints using triaxial tests. Several researchers used both experimentally and numerically non-persistent joints models (Yang et al., 2016) and reproduced the mechanical properties of the bedding plane, i.e. the cohesion, stiffness, and frictional coefficient, as shown in Fig. 2- 2. Jia et al. (2017) studied the failure mechanism of a horizontal borehole in a transversely isotropic shale

gas reservoir using PFC2D. They simulated the laminated rock by assigning different properties to the matrix and bedding planes. Their results showed that the cracking of the laminated model concentrated along bedding planes. Arora and Mishra (2015) observed the typical failure of shale subjected to horizontal stress using a modified biaxial testing device, as shown in Fig. 2- 3. They found that triaxial stress causes conjugate shear failure while flexure failure occurs in unconfined tests, which is in good agreement with field observations.

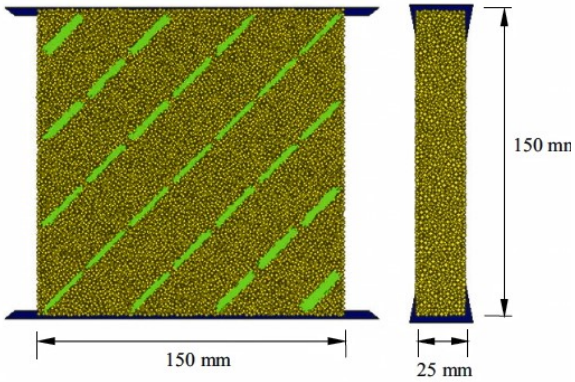

Fig. 2- 2 Non-persistent model (Yang et al., 2016)

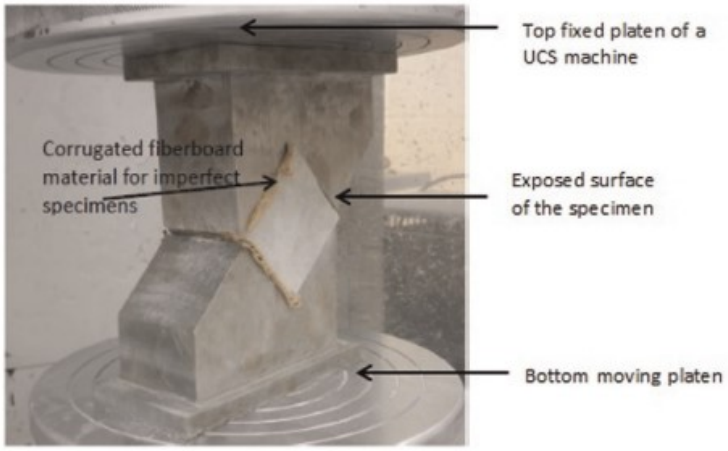

Fig. 2- 3 Modified biaxial device used by Arora and Mishra (2015)

In summary, researchers have conducted a significant amount of investigation into the laminated rock failure mechanism and the effect of bedding planes, especially the effect of the bedding plane orientation. Almost all research focused on Brazilian discs or uniaxial cylinders, where the stress status is far different from the in-situ stress in the field. Also, there is limited research available on the effect of bedding plane strength on laminated rock.

2.3 Measurement of crack development and propagation in rock

Failure of a rock mass initiates by crack development and propagation at the microscopic level (Hoek and Martin, 2014). Roof fall occurrence is intrinsically a process of crack initiation, propagation, and final failure. Therefore, observing crack propagation becomes a vital topic when studying the failure mechanism of laminated roof.

Researchers have used the strain gauge, a device more commonly used to measure surface strain, to observe rock crack development in the laboratory. The most common usage of this method is in impact testing on pre-cracked specimens (He et al., 2021; Liu et al., 2019; Wang et al., 2020, 2019; Zhao et al., 2016). For example, Li et al. (2020) adopted the strain gauge method to measure the Mode I crack propagation in the rock under directional fracture blasting in a pre-cracked hole in the laboratory, as shown in Fig. 2- 4. In their research, the crack propagation velocity and dynamic stress intensity factor validated the feasibility of the strain gauge method. Their results supported that the strain gauge method can approximately record the whole process for dynamic rock crack propagation. Liu et al. (2019) used the strain gauge and high-speed photography to determine the crack propagation behavior of Mode I interlaminar crack in composites. Researchers have also used strain gauges when observing the cracking of a flexural beam. Hadi and Yuan (2017) observed the fracture propagation in flexural behavior of a composite beam with naked eyes, wherein they used the strain gauge as validation. Souici (2013) compared the mechanical behavior of steel-concrete composite beams bonded with various connections and adhesives. In their experiment, they mounted the strain gauges at the bottom face of the upper layer, the lower concrete slab, and along the composite specimen height. The measurements showed that the slip and strain distribution is different in composite beams with different bonding methods.

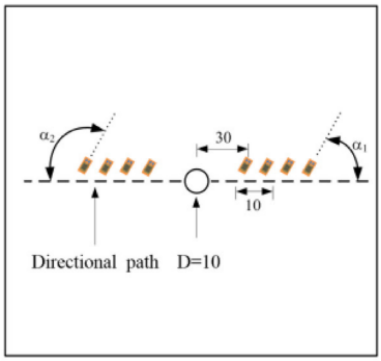

Fig. 2- 4 Strain gauge method for recording dynamic I cracks in rocks

Researchers have also used newly developed methods such as laser gap gauge (Dai et al., 2010) and digital image correlation (DIC) (Munoz et al., 2016; Schreier et al., 2009; Xing et al., 2018) to observe cracks in rock. The laser gap gauge measures gap opening distance and the opening velocity of the fractured specimens. The DIC is a non-contact optical method to measure the deformation and strains on the surface of objects (Garg et al., 2020; Hedayat et al., 2014). For example, Xing et al. (2018) used 3D-DIC to examine full-field strain and strain-rate fields of rock materials under dynamic compression applied by a split Hopkinson pressure bar. They observed the crack propagation using visual observation and DIC, as shown in Fig. 2- 5. The strain localization captured by DIC was in good agreement with the naked-eye observation results. Munoz (2016) used 3D-DIC to measure the full-field strain and compared it with direct measurement methods, such as the strain gauge methods, LVDT, and extensometer method. He showed the advantages of using this non-contact optical method to instrument strain. However, for crack growth observation, this method failed to show advantages in comparison to the direct methods mentioned above.

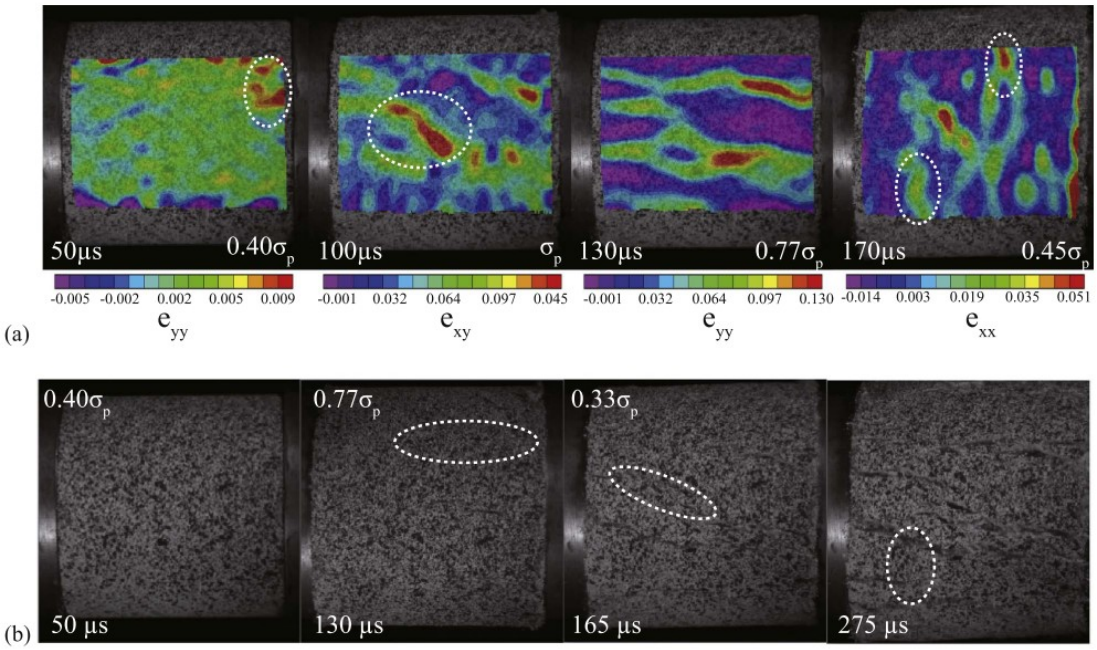

Fig. 2- 5 DIC acts as a supplementary method of visibility when observing cracks (Xing et al., 2018)

Research has regularly used numerical analysis for simulating crack development and propagation. This includes many efforts to simulate the crack distribution and propagation on pre-cracked specimens (Haeri et al., 2014; Manouchehrian and Marji, 2012; Saadat and Taheri, 2019; Sarfarazi and Haeri, 2016; Xi et al., 2020), as well as the crack growth laws and influential factors.

Manouchehrian and Marji (2012) studied the confinement effect on the crack development process under compression. Previous research has included numerical studies of the effect of dynamic load on crack propagation (Ai et al., 2019; Zhou and Wang, 2016). Crack propagation in laminated rocks can be found mostly in hydraulic fracturing for natural gas extraction (Cherian et al., 2014; Shan et al., 2018; Zhou et al., 2016). These results validated the usability of numerical methods for understanding crack developments and propagation in laminated rocks. In contrast, research rarely investigated underground laminated rocks. Bai and Tu (2020) showed the initiation and propagation of microcracks and macroscopic fractures and the development of the associated damage, stress, and deformation in laminated and jointed roof using a 2D discrete element model. Their simulation showed four stages of the damage process. Zhang et al. (2014) proposed a fracture mechanics-based model for simulating the flexural performance of layered cementitious composite-concrete composite beams. They obtained the complete crack growth of the layered beam, and the model results showed a comprehensive application of simulating crack propagation in laminated beams.

In summary, though various methods have been applied to observe crack initiation and propagation, the most effective way is still the numerical method, while other approaches can serve as a supplementary tool.

2.4 Roof stability modeling with coupling DEM/FDM

Previous studies adopted continuum-based numerical methods to understand roof failure in underground coal mines (Clifford, 2004; Coggan et al., 2012; Gadde, 2003; Wang et al., 1974; Zipf, 2006). However, researchers stated that the continuum-based numerical methods used oversimplified assumptions (Abousleiman et al., 2020; Gao and Stead, 2013; Sherizadeh and Kulatilake, 2016; Wang et al., 2021). Their research showed that previous studies modeled roof behavior using unrealistic conditions because roof rocks such as shale and sandstone consist of fine grains with granular behavior. Furthermore, the large deformation and fracture propagation are difficult to interpret in continuum approaches.

In contrast to continuum-based methods, the discrete element method (DEM) explicitly takes into account the discrete nature of granular material (Breugnot et al., 2016). This method achieved this by using an assembly of particles interacting together through contacts based on simple physical laws. Cundall first introduced bonded particle material, one of the DEM (1979a, 1971). This

program naturally adapts the granular behavior of rocks and considers the rotation moments acting between particles. This program performs well in observing the fracture development by recording the failure contacts between particles. Researchers have widely employed the DEM in roof fall studies after developing the method for decades (Abousleiman et al., 2020; Gao, 2013; Sherizadeh and Kulatilake, 2016; Wang et al., 2021). Gao (2013) used both PFC and 3DEC to investigate the effect of horizontal stress on roof fracturing behavior, as well as observing cutter roof failure. Their research shows that the DEM is capable of reproducing the stress and deformation characteristics in the field. Sherizadeh (2016) used 3DEC to simulate the influential factors of roof stability, such as horizontal stress, rock mass mechanical parameters, and bedding plane parameters, in a room and pillar mine in Pennsylvania. This study assessed the intensity of the cutter roof failures, shear and tensile failures along bedding planes, and normal and shear displacements. Abousleiman et al. (2020) conducted a parametric sensitivity analysis of factors influencing coal mine roof behavior using 3DEC. Their results validated that beds play a significant role in determining the self-supporting capacity of bedded and jointed sedimentary roofs. Wang (2021) used PFC3D to investigate the pressure arch formed by bolting gravel-shape particles. In summary, the DEM is capable of simulating roof failure in coal mine entries.

However, the DEM also has a significant drawback, which is due to particle characteristics. For large engineering problems, a large number of particles are necessary to represent the complete model, which significantly increases computational time. However, a reduction in particle size decreases the computational time, but also reduces accuracy. Considering the limitations and advantages of each type of approach, researchers argued that the DEM should not serve as a substitute for continuum methods. The most ideal scenario is that the DEM will act as a supplement for continuum methods (Gholaminejad et al., 2020; O'Sullivan, 2011).

In the past few years, researchers extensively used coupled discrete and continuous approaches for problems with flow behavior. In this approach, researchers used the DEM in the area of interest while using the continuum approach in the far-field where strains and displacements are much smaller. Through this coupling strategy, researchers can preserve the computational time without sacrificing the accuracy of the parameters of interest. Felippa and Park (1980) proposed the first coupling method. Indraratna et al. (2015, 2016) developed a coupled model of the DEM and FDM based on PFC2D and FLAC to model the interaction between stone columns and surrounding clay.

They simulated the columns with BPM and simulated the surrounding clay by elastic materials in the frame of FLAC, as shown in Fig. 2- 6. The coupling model treated the finite difference nodal displacements as velocity boundary conditions for the discrete elements, and it applied the forces acting on the discrete elements as the force boundary conditions to the finite difference grids. Using this approach, they achieved the coupling between the DEM and FDM at the soil-column interface. They then compared the vertical stress and lateral deformation of the DEM column to the reported data, and their results showed that the coupled model captured the load-displacement behavior of the targeted objects.

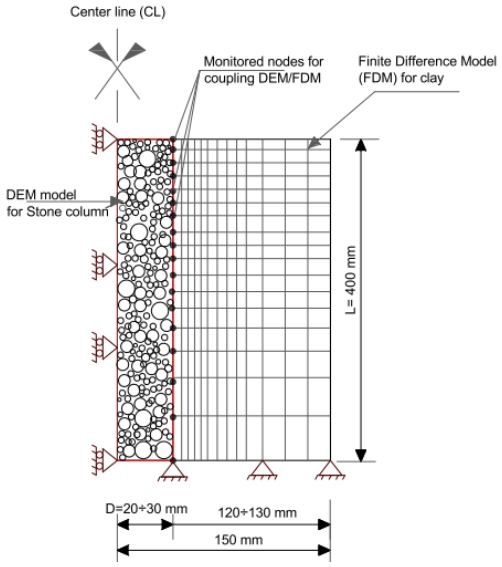

Fig. 2- 6 Conceptual model of soft clay reinforced with a stone column using coupled discrete–continuum method (Indraratna et al., 2015)

Studies have extensively reported on applications of coupling PFC and FLAC in civil engineering (Gholaminejad et al., 2020, 2019; Ngo and Indraratna, 2020; Shi et al., 2020; Tran et al., 2021; Xu et al., 2021). Jia et al. (2020) presented coupled algorithms that have been used with PFC3D and FLAC3D models (Fig. 2- 7). The discrete subdomain serves as the stress boundary for the continuum subdomain, while the continuum subdomain provides displacement/velocity constraints to the discrete subdomain. They examined the continuity of stresses at the discrete–continuum interface and vertical displacement of the monitoring point in order to validate the coupled model.

Ma et al. (2019) simulated a tunnel across an active fault with PFC3D and FLAC, calibrating the parameters with laboratory tests. However, they did not validate the complete model response with

additional data. Huo (2020) used coupled PFC and FLAC to model the top coal caving law. Zhang et al. (2018) used coupled 3DEC and FDM to simulate the overburden strata movement and near-surface stress change in a longwall coal mine.

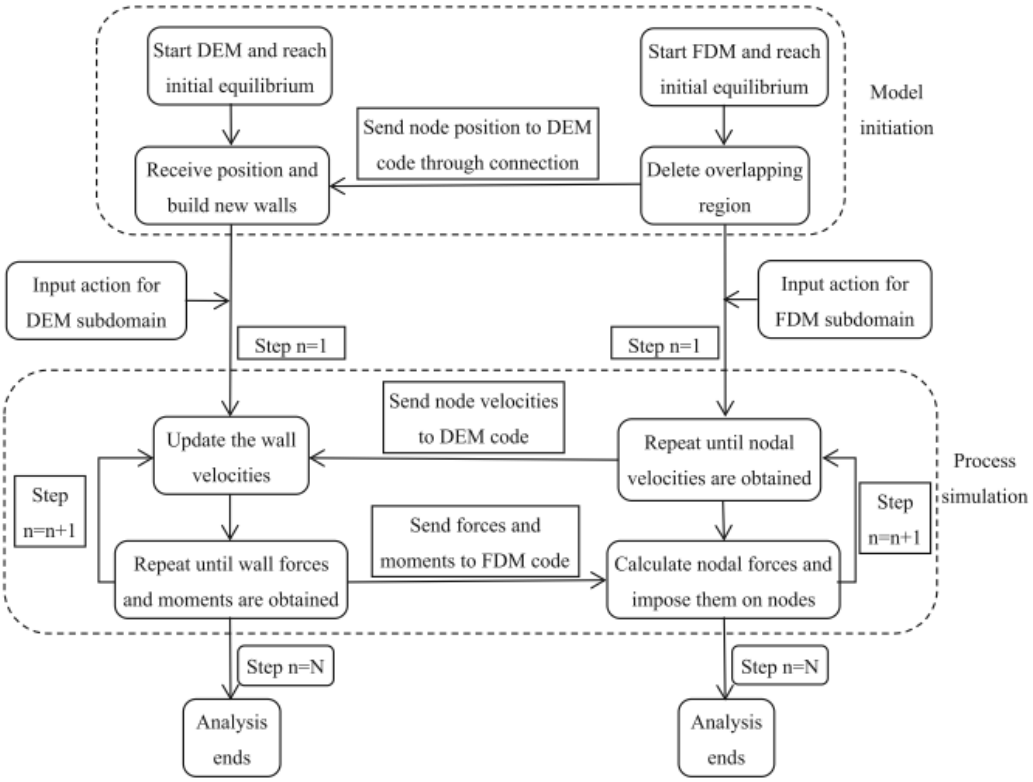

Fig. 2- 7 Flowchart of the DEM-FDM coupling (Jia et al., 2020)

In general, it is easily concluded that the application of coupling FDM and DEM is a promising approach when probing fracturing and large deformation problems of large-scale rock engineering problems. However, its application in coal measures strata is still uncommon. Furthermore, researchers have not yet reported its application in studying laminated roofs and extraction-caused abutment pressure.

2.5 Summary

Several factors influence laminated roof stability. Some factors, such as in-situ stress, bedding plane properties, bedding properties, and geological conditions, affect delamination propagation and laminated roof stability. Based on the literature review, this research can further pursue at least three aspects of work to understand the mechanism and influential factors of laminated roof failure,

the effect of lamination properties, the delamination process, and the effect of abutment stress caused by coal extraction.

Laboratory and numerical approaches serve as ideal tools to implement this research work. First, research should investigate the effect of lamination properties on the geomechanical behavior of laminated rock and large-scale laminated roof in detail. Though previous studies have thoroughly investigated the transverse anisotropy caused by laminations with respect to the bedding orientation, they have rarely reported on the effect of bedding plane strength on the geomechanical behavior of laminated rock. This review demonstrated the necessity of studying the effect of lamination properties in both laboratory and numerical models. Second, research should study the failure process and delamination propagation in the laminated rock/roof. Literature reviews provide good insight on approaching this topic using DEM numerical methods. Finally, research should study laminated roof failure behavior under the effect of extraction-caused abutment pressure. This is hard to investigate in the field due to the number of influential factors. Numerical simulation with coupling DEM and FDM serves as an effective way to move this topic forward.

CHAPTER 3 THE MECHANICAL BEHAVIOR OF SYNTHETIC LAMINATED ROCKS WITH DIFFERENT BEDDING PLANE COHESIVE STRENGTHS SUBJECTED TO BIAXIAL AND TRIAXIAL STRESSES

3.1 Introduction

In the past few decades, researchers have conducted extensive investigations on the influential factors for the failure of laminated rock. Many have considered the orientation of the bedding planes to be one of the key influential factors in the mechanical behavior of laminated rocks (Dou et al., 2019a; Heng et al., 2015; Sherizadeh and Kulatilake, 2016; Tan et al., 2015; Yang et al., 2019). In a typical US underground entry, principal stresses in the surrounding rock are nearly parallel to the bedding plane and the failure tends to occur predominantly along the bedding planes (Gadde and Peng, 2005; Gao and Stead, 2013). Researchers have replicated this phenomenon in both laboratory tests and numerical simulations (Bai and Tu, 2020; Morgan and Einstein, 2014; Shi et al., 2021). In addition, the confinement provided by roof skin support restricts progressive spalling in a laminated roof (Bai and Tu, 2020), indicating the potential function of confinement to constrain laminated roof failure.

Substantial research has considered bedding plane strength properties as imperative influential factors, mainly from the perspective of numerical and analytical perspectives. Research has found bedding plane strength parameters, including tensile strength and cohesive strength, to present a dominant impact on the mechanical behavior of laminated rock (Chong et al., 2017; Dou et al., 2019b; Yang et al., 2019). Moreover, research found numerically that the cohesive-to-tensile ratio controls the failure pattern in some loading conditions such as indirect tension (Chong et al., 2017; He et al., 2018) and three-point bending (Dou et al., 2019b). In addition to strength parameters, bedding plane spacing and lamination thickness affect the degree of damage of laminated rock when studying wellbore stability (Jia et al., 2017). On the other hand, analytical solutions, including Jaeger's Plane of Weakness model (Jaeger, 1960b, 1959; Jaeger et al., 2009) and transversely isotropic deformability model (Amadei, 1982; Amadei and Goodman, 1982), provided a quantitative knowledge of the relationship between bedding plane strength and mechanical behavior of laminated rock in an ideal condition. It is noted that most of these studies

investigated the effect of bedding plane strength under uniaxial compressive or tensile stress conditions. Due to the difficulty in obtaining laminated rock with different bedding plane strengths while keeping their matrix properties constant, researchers have not sufficiently reported experimental analyses on this topic.

Therefore, this chapter includes the development of synthetic laminated rock (SLR) specimens with bedding planes to investigate laminated rock behavior. This research conducted serial parametric tests to determine the effect of the bedding plane cohesive strength (C_p) on geomechanical behavior of laminated rocks under biaxial and triaxial stress conditions, including failure stress, failure modes, and deformability.

3.2 Fabrication of SLR with different cohesive strengths of bedding plane

Laminated rocks comprise beddings/matrix and bedding planes. Observing the effect of C_p on the geomechanical behavior of laminated rocks requires constant bedding properties, which is impossible for actual laminated rock in the field. This research cast the SLR with a concrete mixture comprising Portland cement, sand, and hydrated lime; it reproduced the bedding plane by the construction lift between beddings. This research varied the C_p in the SLR using two methods, checking the applicability of these methods by conducting direct shear tests along the planes. One method was by varying the pouring time interval of the concrete beddings, and the other was to apply different normal stresses on the construction lift during the curing of the concrete mixture. This research found the second method to be more successful and therefore used it to cast SLR with various C_p. We then conducted Brazilian tests on SLR from different inclined angles and compared them with laminated shale specimens to verify the capacity of the SLR to replicate actual laminated rocks.

3.2.1 Experimental approach to vary cohesive strength of bedding plane

The SLR fabrication used a concrete mixture proportion of Portland cement: sand: hydrated lime: water=1.0:0.8:0.2:0.5. This approach used wooden molds for casting the concrete. The concrete blocks were cured for more than 28 days at a constant temperature of 72 ˚F as per ASTM standard (ASTM C192/C192M, 2016).

The first method to vary the C_p of the plane was by varying the pouring time interval between beddings. Previous studies found that the strength of the lift can decrease with the increase of the

time interval (Liu et al., 2018). The second method was to apply different normal stresses on the construction lift when curing the concrete mixture. This method applied the normal stress by putting dead weight on the top of the blocks during curing. For simplicity, this research first fabricated concrete blocks with only one plane for testing purposes. Note that the second method for the creation of a bedding plane had its time interval maintained at 3 hours. Fig. 3- 1a depicts the procedure to vary the C_p by varying the pouring time interval. In this method, the bottom matrix stood for t hours before pouring the top matrix and therefore fabricating a construction lift, i.e., a plane. Fig. 3- 1b shows the procedure to vary the plane strength by applying different normal stresses on the top of the concrete block during curing.

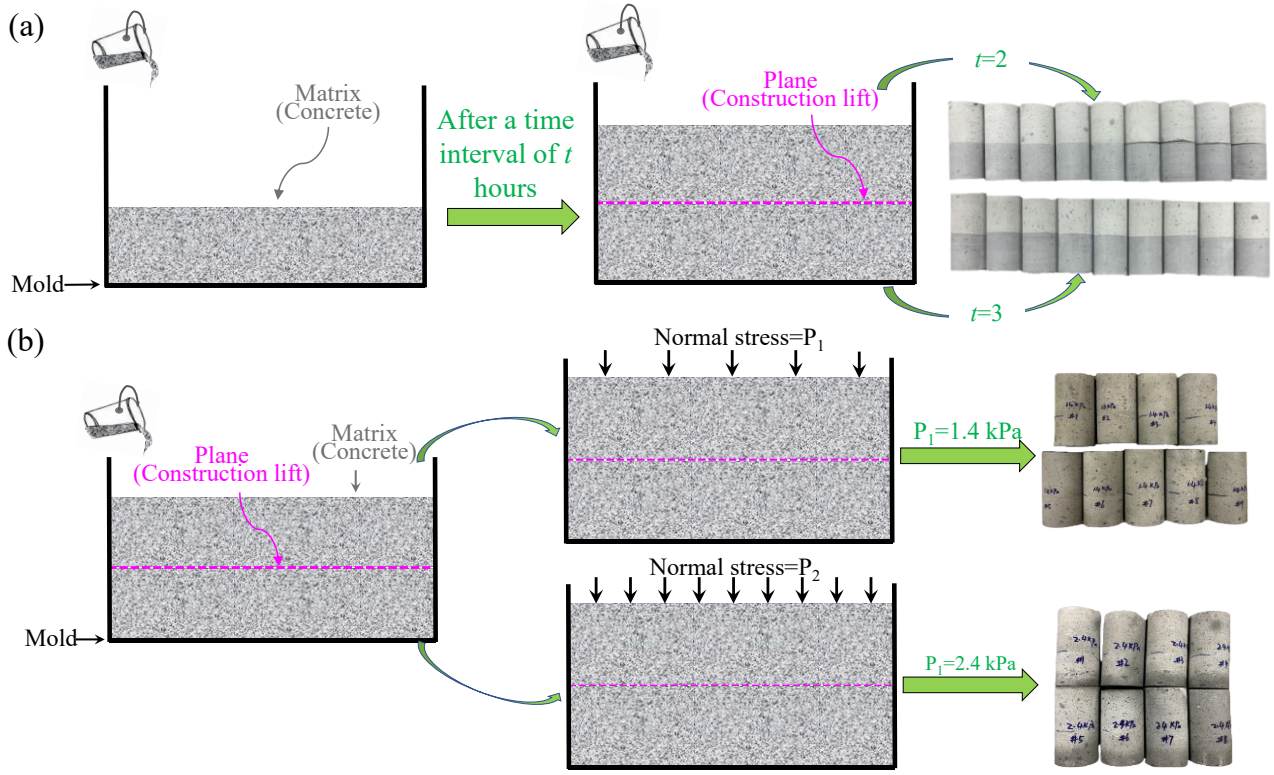

Fig. 3- 1 Depiction of fabricating planes with different C_p by (a) varying pouring time interval and (b) applying various normal stresses while curing (t represents time interval, in hours; normal stress realized by putting dead weight on top of blocks)

The first method fabricated concrete blocks containing planes with a time interval of t=2 hours and t=3 hours (named 2h-interval plane and 3h-interval plane, respectively). The second method cast concrete blocks containing planes made under normal stress of P_1=1.4 kPa and P_2=2.4 kPa (named 1.4 kPa plane and 2.4 kPa plane, respectively). After the concrete blocks cured, we cored concrete cylinders from each block using a 2.1"-diameter drill bit and prepared them as testing specimens as per ASTM standards, as shown in Fig. 3- 1. This process created four groups of specimens for

shear tests. Both methods included two groups of specimens. Fig. 3- 2 shows the direct shear testing system that conducted direct shear test along the planes. Each group of specimens underwent five sets of direct shear tests under normal stress ranging from 0.68 MPa to 6.21 MPa with an interval of 1.38 MPa.

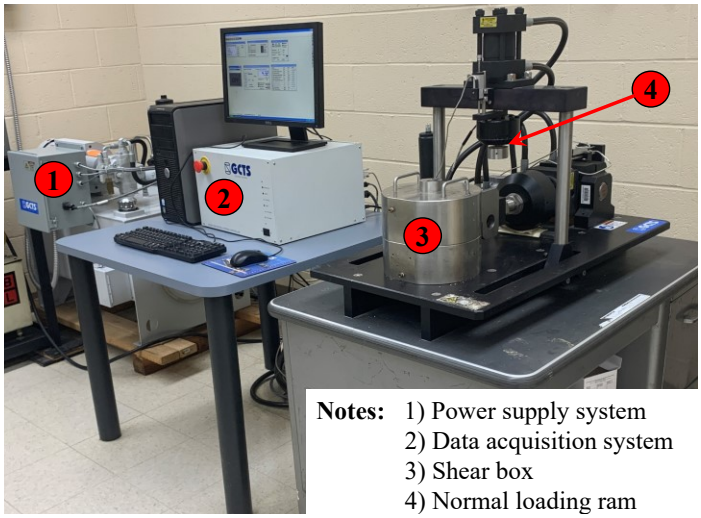

Notes: 1) Power supply system
2) Data acquisition system
3) Shear box
4) Normal loading ram

Fig. 3- 2 GCTS direct shear testing system for testing plane strength of samples

After direct shear tests, we plotted the shear strengths of the planes against the normal stress and obtained the C_p by fitting the data sets (Conshohocken, 1995). Fig. 3- 3 presents the results obtained through these two methods, where the y intercepts of the trendlines correspond to the C_p of the planes. Fig. 3- 3a shows that the C_p of the 2h-interval planes is 0.25 MPa while the C_p of the 3h-interval planes is 0.30 MPa. The C_p of the 3h-interval planes is even higher than the 2h-interval planes. This result did not meet the expectation that plane strength decreases with the increment of the pouring time interval. This showed that the first method cannot control the C_p. However, results presented in Fig. 3- 3b show that the second method was successful. The plane under normal stress of 1.4 kPa showed a strength of 3.08 MPa and the plane with normal stress of 2.4 kPa showed a strength of 3.87 MPa. In conclusion, the experimental practice confirmed that the second method successfully varied the plane cohesive strength C_p.

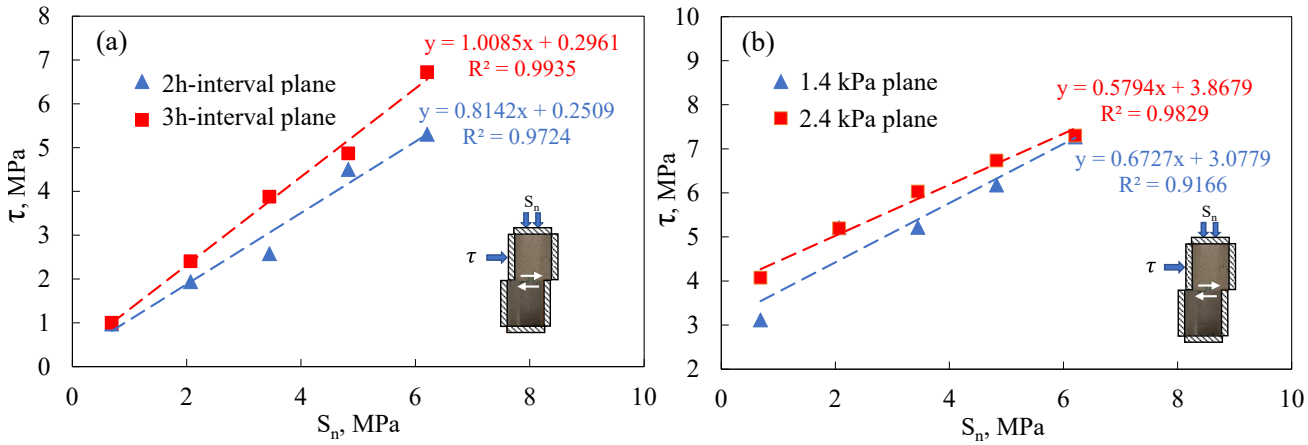

Fig. 3- 3 Direct shear results on planes made by (a) varying time interval and (b) varying applied normal stress during curing (dashed lines represent fitted results for each plane; y intercepts of fitting formula represent C_p; τ corresponds to shear strength; S_n corresponds to normal stress applied on shear plane)

3.2.2 Fabrication and verification of SLR

For observation of the effect of C_p on the mechanical behavior of laminated rock, this section includes the fabrication of SLR with different C_p. Multiple parallel construction lifts represent the bedding planes. The verified second method then varied the C_p. We cast three groups of SLR with various C_p and obtained the C_p values with direct shear tests. Afterward, we conducted Brazilian splitting tests on these three groups of SLR to verify their capacity of replicating actual laminated rocks.

3.2.2.1 Fabrication of SLR incorporating various C_p

This process used the same concrete mixture for casting SLR, with the plane spacing set constant as 1.0 cm. We fabricated bedding planes by applying normal stress of 0 kPa, 0.5 kPa, 1.0 kPa on the concrete blocks (named group A, group B and group C) respectively to obtain SLR with different C_p. After the blocks cured, Fig. 3- 4 shows the cored cylindrical specimens, wherein the grey and white colors represent different beddings which were differentiated by adding ink to the concrete mixture.

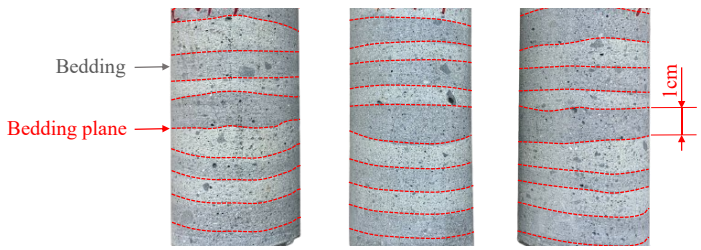

Fig. 3- 4 Depiction of cored synthetic laminated specimens (red dashed lines represent bedding planes)

To determine the exact C_p in SLR specimens of group A, group B, and group C, each group underwent five sets of direct shear test under normal stress, ranging from 0.68 MPa to 6.21 MPa with an interval of 1.38 MPa; this is the same as the tests in section 3.2.1. Fig. 3- 5 shows the variations of the shear strength with the normal stress. The C_p of group A, B, and C was read from fitting equations directly as 1.61, 2.37, and 4.16 MPa respectively.

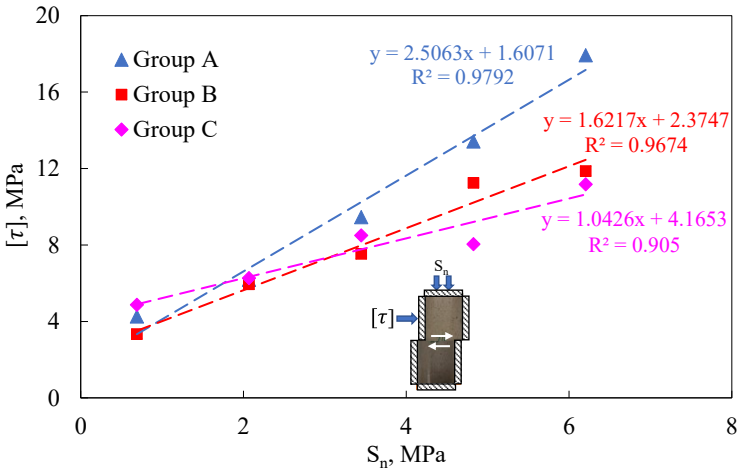

Fig. 3- 5 Direct shear results on planes of group A, group B, and group C

3.2.2.2 Verification of SLR using Brazilian tests

In the earlier section, we verified the methodology for the variation in plane strength. However, it is imperative to validate the replication of the actual behavior using the multi-parallel construction lift approach. For verification, these three groups of SLR underwent Brazilian splitting tests from different inclined angles (β), defined as the angle between the normal of the bedding plane and the loading axis. The present study selected inclined angles of 0˚, 30˚, 60˚, and 90˚ for verification. Each group underwent twenty sets of Brazilian tests, with five sets for each inclined angle. We then compared the failure behavior, including failure pattern and Brazilian tensile strength variation, to that of actual laminated rock.

Fig. 3- 6 shows the variation of averaged Brazilian tensile strengths of these three groups of SLR loaded from different inclined angles. Generally, the tensile strengths of each group decreased with the inclined angle. The results were in good agreement with reported research wherein Brazilian tensile strength of Mosel slate (Tan et al., 2015) and shale (He et al., 2018) decreases with the increment of the inclined angle. From this perspective, the test result verified the capacity of our SLR to replicate actual laminated rock. In addition, the Brazilian tensile strength at any inclined angle is ranked as group A < group B < group C. For example, at an inclined angle of 30˚, the

Brazilian tensile strength of group A is 2.03 MPa, while that of group B and group C are 2.08 and 2.23 MPa respectively. This result implies that a higher C_p brings higher tensile strength of the SLR.

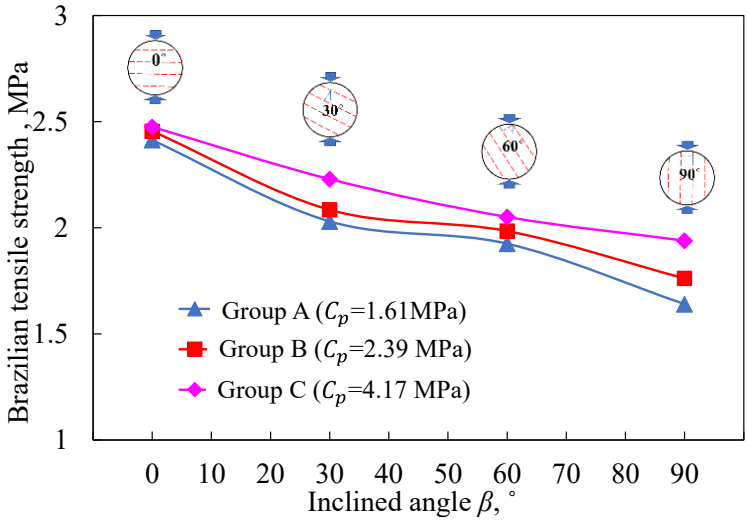

Fig. 3- 6 Variation of Brazilian tensile strength with different inclined angles

We also observed typical failure patterns of our SLR loaded from different inclined angles. Generally, there was no pronounced failure pattern difference between groups A, B, and C. Fig. 3- 7 depicts typical failure patterns under each inclined angle and compares them to that of actual shale (He et al., 2018). Fig. 3- 7 illustrates that more than one failure pattern was observed in specimens with each inclined angle β. For specimens with an inclination angle of β=0˚, 30˚, and 60˚, one failure is characterized with a vertical curved fracture that deviates from the load direction of the SLR discs. The other failure pattern is accompanied by fractures that propagate parallel with weak planes. These two patterns agree well with the tests on actual shale, as shown in the rows of β=0˚, 30˚, and 60˚ in Fig. 3- 7. In 90˚ specimens, most of the fractures propagate precisely along the bedding planes while accompanied by minor fractures parallel to the bedding planes, which is also in good consistency with test results on actual shale as shown in the row of β=90˚ in Fig. 3- 7.

In conclusion, both Brazilian tensile strength and failure pattern variation with inclined angles agreed well with published results on shale, verifying the capacity of the SLR to replicate the actual laminated rock.

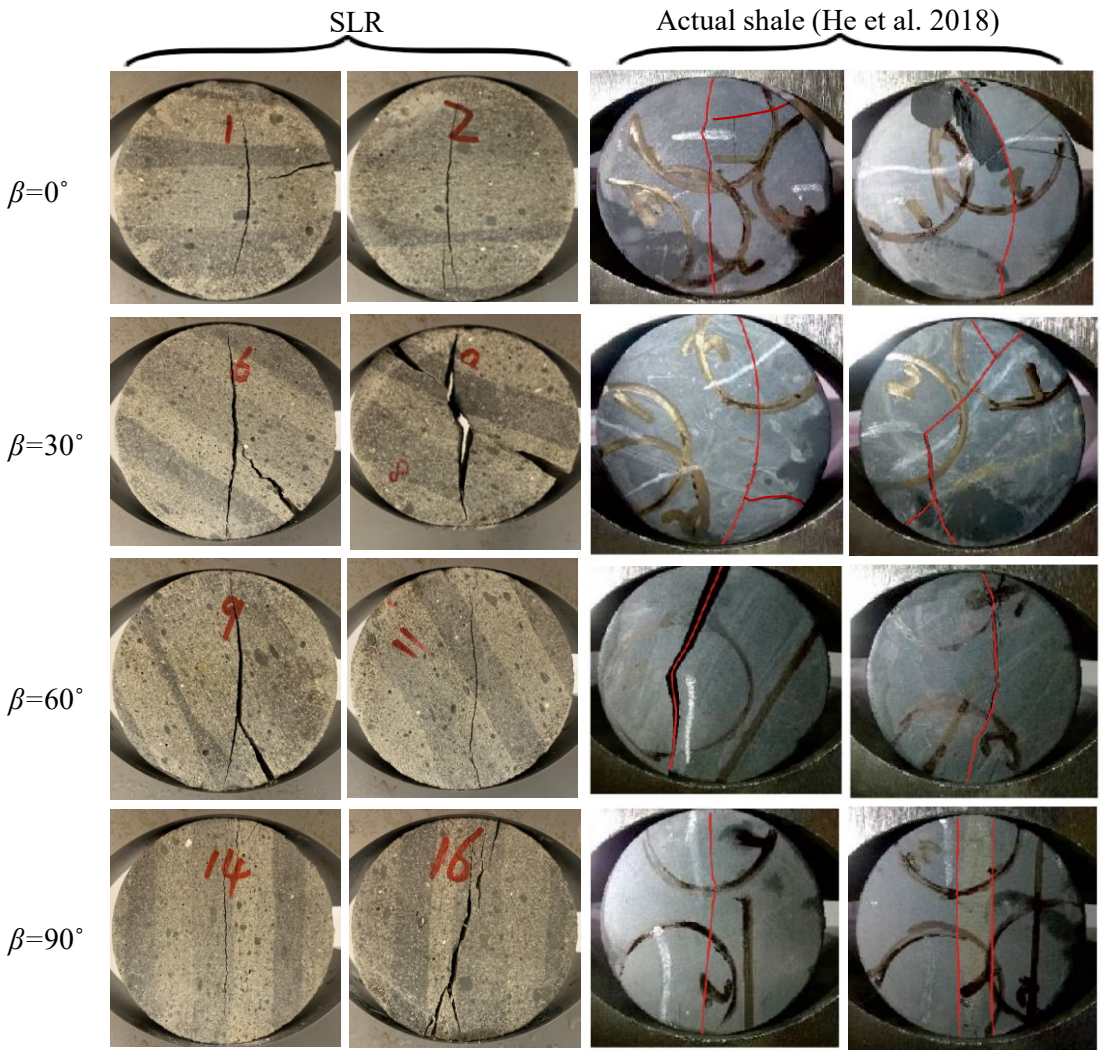

Fig. 3- 7 Comparison of typical failure patterns between SLR disc and actual shale discs under different inclined angles (red lines correspond to fractures of shale discs)

3.3 Biaxial and triaxial tests on SLR

This section used a specially developed platen set to apply biaxial and triaxial stresses on these three groups of SLR with different C_p fabricated above. This process was done to observe the mechanical behavior of the SLR, including strength, failure mode, and deformability, to analyze the effect of C_p.

3.3.1 Biaxial and triaxial loading apparatus

Entry roof in an underground coal mine is in a special stress condition wherein the horizontal stress σ_{h1}, σ_{h2} are normally far larger than the vertical stress σ_v which is usually less than a couple of MPa or even close to zero near the roof line, as shown in Fig. 3- 8. Kaiser et al. (2018) pointed out that in a low confinement condition, the rock mass can generate local tensile stresses that introduce

fractures parallel to the maximum compressive stress, which corresponds to the horizontal stress here. These fractures could propagate into typical spalling or delamination failure, which is a common roof failure problem in underground mines. Therefore, when studying the effect of C_p on the mechanical behavior of laminated rock, it is of vital importance to take this special in-situ stress condition into account.

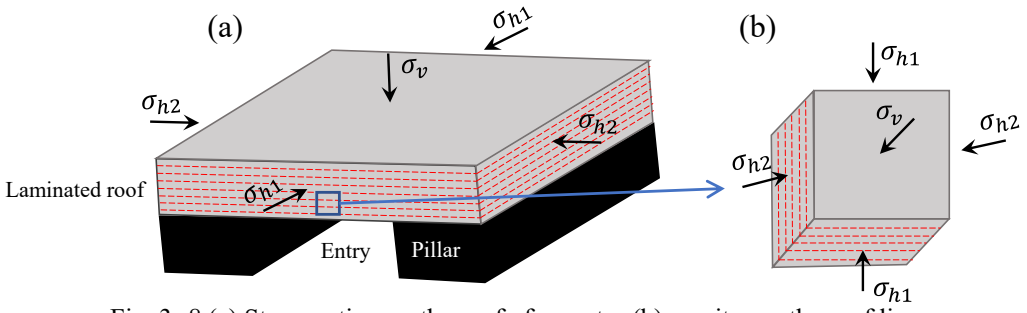

Fig. 3- 8 (a) Stress acting on the roof of an entry (b) a unit near the roof line

Researchers have recognized true triaxial test to be the most ideal method to reproduce this in-situ stress condition. However, such equipment is limited in availability and beyond the financial scope of the present research. Instead, this research used a frame made of hardened steel capable of applying biaxial stress, designed in Rock Mechanics Laboratory at West Virginia University (Shrey Arora and Mishra, 2015), to apply biaxial stress here. The frame consists of a top and lower platen with a pair of perpendicular surfaces that apply equal loads to a cubic specimen, as shown in Fig. 3- 10a. The loads are transited from MTS (MTS Systems Corporation) closed-loop electro-hydraulic testing system (Fig. 3- 9) to which the frame is attached, as shown in Fig. 3- 10b, wherein "*P*" is the load provided by the testing system and "*N*" is the split component loads acting normal to the specimen faces and parallel to the beddings. The biaxial compressive stress is calculated as $S_{bc} = N/A_{avg}$. A_{avg} is the approximate area of the face of the cubic specimen in contact with the biaxial platen, calculated as $A_{avg} = (A_1 + A_2)/2$, wherein A_1 and A_2 are specimen area in contact with adjacent arms of the biaxial platen. This method replicates a stress condition of σ_1=σ_2 =S_{bc}, $\sigma_3 = 0$.

Fig. 3- 9 MTS servo-controlled compression testing machine and its components
(1) Machine load, (2) Glass shield, (3) Hydraulic actuator, (4) Manual control system, (5) Strain Gauge control panel, (6) Computer, (7) MTS data acquisition system (Xue, 2019)

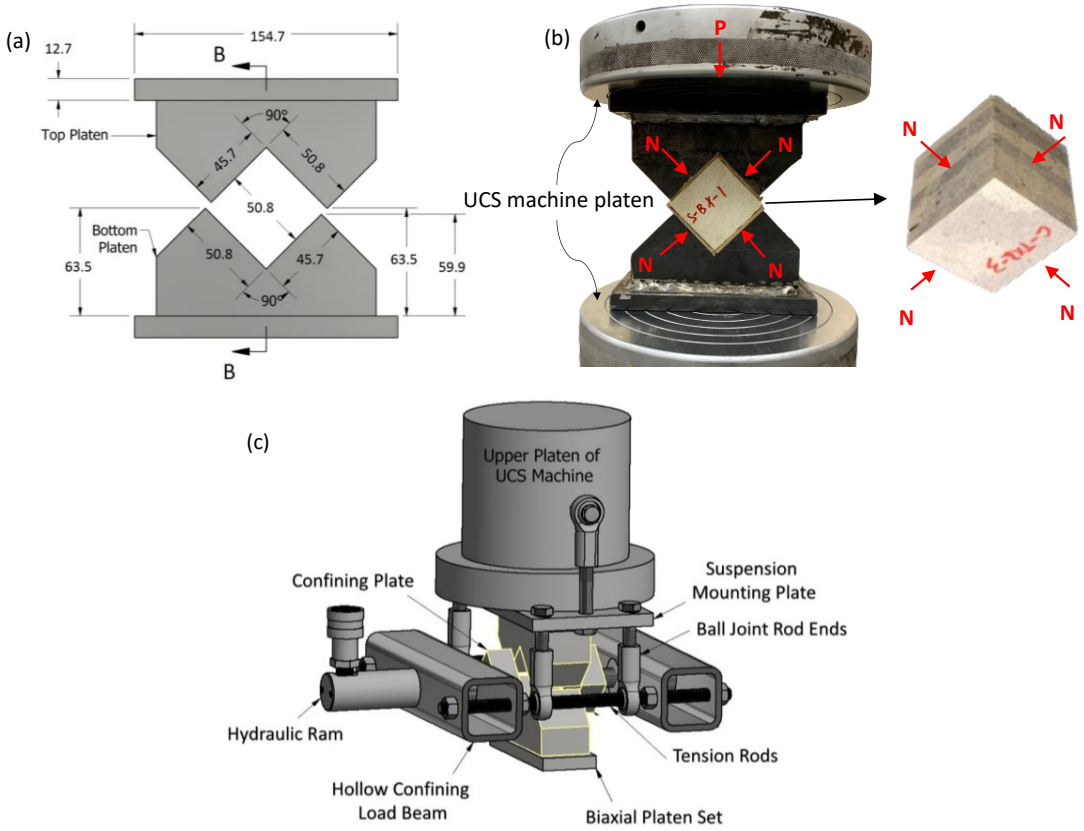

Fig. 3- 10 (a) Schematic view and (b) test setup of biaxial frame, (c) set-up of triaxial test with confining device

For a non-zero σ_v, this method modified the platen by adding a confining device to apply the σ_v as shown in Fig. 3- 10c. A pair of square confining plates (dimensions of 50.8×50.8×49.53mm) mounted the confining device to the platen of the loading frame. A hydraulic pump applies the confining stress. The device has a load capacity of 45 kN and it applies a maximum confining stress of 17.4 MPa for a cubic specimen of 50.8×50.8×50.8 mm. We used this device for the triaxial test on the SLR specimens.

3.3.2 Specimen Preparation

Preparation of these three groups of SLR with various C_p involved saw cutting and surface grinding them into 50.8×50.8×50.8 mm cubes. To replicate the stress condition depicted in Fig. 3-8, we cut the cubic faces along a direction where the bedding plane was parallel to the axial load. To minimize friction on the specimen faces, we inserted fiber cardboard shims (2 mm in thickness) between the platens and SLR specimens, and smeared Petroleum jelly between the shims and the platens as a lubricant. The lubricant was not directly used on the specimen face to prevent fluid penetration into the specimen.

This procedure placed the specimens on the platen with the bedding planes oriented parallel to the loads when testing. The triaxial tests applied the confining stress along the direction perpendicular to the bedding planes and maintained it as constant by a hydraulic pump with a regulator valve. The loading cell measured the load *P* directly, and the LVDT mounted in the test system measured the deformation of the specimen.

3.3.3 Testing Procedure

This procedure first conducted biaxial compressive tests ($\sigma_1 = \sigma_2$, σ_3 =0) and obtained the unconfined biaxial compressive strength (σ_{bc}). Next, the triaxial tests set the confining stress σ_3 at 2.5% of σ_{bc} and 5.0% of σ_{bc}. For instance, SLR specimens of group A had an average biaxial compressive strength of σ_{bc}=71.72 MPa. The confining stress σ_3 was then set at 1.79 MPa (2.5% of σ_{bc}) and 3.56 MPa (5.0% of σ_{bc}). Therefore, this procedure tested each group of SLR specimens under three different stress conditions. This included biaxial test, triaxial test with a confining stress of 2.5% of σ_{bc}, and triaxial test with a confining stress of 5.0% of σ_{bc} respectively. For each group under each stress condition, this research conducted five tests and tested a total of 45 SLR specimens in the overall test effort. These tests correspond to the axisymmetric extension tests

(σ_1=σ_2>σ_3) (Ma et al., 2017; Ma and Haimson, 2016). In each triaxial case, the test followed a loading path composed of two stages shown as Fig. 3- 11:

(1) Loaded the specimen monotonically in compression through the confining plates until it attained the preset σ_3 level.

(2) Maintained the σ_3 constant while $\sigma_1 = \sigma_2$ increased together monotonically with stain control mode (by controlling the platen displacement at a fixed strain rate) until failure of SLR.

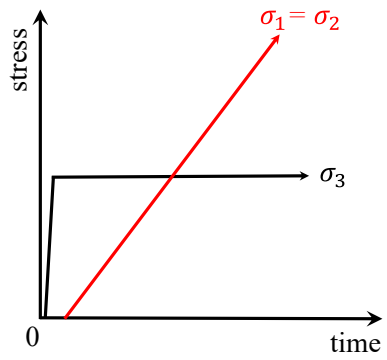

Fig. 3- 11 Loading path used in triaxial testing under strain control mode

During the test, we recorded the load-displacement relationship and, after failure, photographed and analyzed the post-test state of the specimen.

3.4 Results

3.4.1 Strength variation

Table 3- 1 presents the biaxial test results, which include the biaxial compressive strength σ_{bc} along with the C_p of each specimen. In addition, the table includes the calculated compressive modulus corresponding to the elastic linear part of the stress-strain curves. Section 3.4.5 includes the details to determine the linear part of the stress-strain curves.

Table 3- 1 Results of biaxial tests on laminated specimens with various C_p

	C_p, MPa	σ_{bc}, MPa	Averaged σ_{bc}, MPa	Biaxial compressive modulus, GPa	Averaged biaxial compressive modulus, GPa
Group A	1.61	70.35	71.72	2.85	3.54
	1.61	73.92		3.44	
	1.61	69.52		3.64	
	1.61	70.87		3.62	
	1.61	73.93		4.13	
Group B	2.37	79.06	77.29	3.45	4.02
	2.37	77.30		4.01	
	2.37	75.69		4.02	

	2.37	75.34		4.42	
	2.37	79.08		4.19	
Group C	4.16	87.12	80.36	4.38	4.23
	4.16	80.35		4.22	
	4.16	77.62		4.61	
	4.16	80.04		4.36	
	4.16	76.68		3.57	

Fig. 3- 12 shows the variation of the biaxial compressive strength and biaxial compressive modulus with the C_p of specimen among these three groups. The results show that both σ_{bc} and biaxial compressive modulus increase with an increase in C_p. Fig. 3- 12a shows that the σ_{bc} difference between group A and group B is 5.57 MPa, and the difference between group B and group C is 3.07 MPa. The increase rate of biaxial compressive strength with respect to the C_p was 7.33 MPa/MPa and 1.72 MPa/MPa, indicating that the increase rate of σ_{bc} gets smaller when C_p increases. The biaxial compressive modulus presents the same trend shown in Fig. 3- 12b. This leads to the conclusion that the strength and stiffness increased with the increase of C_p in the SLR, and this effect is more sensitive when the C_p is lower.

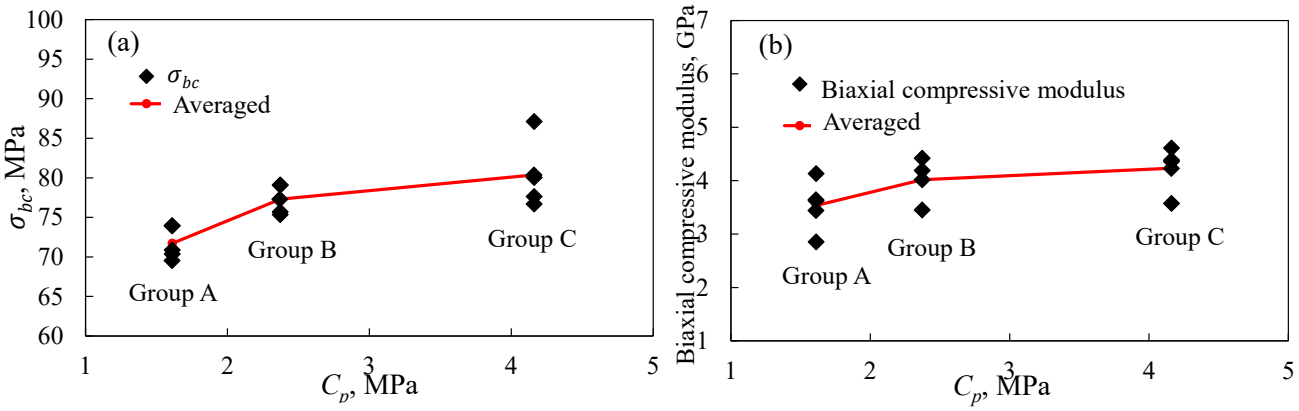

Fig. 3- 12 Variation of (a) biaxial compressive strength and (b) biaxial compressive modulus

Table 3- 2 lists triaxial tests results with confining stress of 2.5% of σ_{bc}, 5.0% of σ_{bc} in sequence, presenting the triaxial compressive strength, referred to as σ_{tc} here, and compression modulus of our SLR specimens.

Table 3- 2 Triaxial test results under confining stress of 2.5% of σ_{bc}

	C_p, MPa	Confining stress, MPa	σ_{tc}, MPa	Averaged σ_{tc}, MPa	Triaxial compressive modulus, GPa	Averaged triaxial compressive modulus, GPa
			Confining stress = 2.5% of σ_{bc}			
Group A	1.61	1.79	90.01	87.91	3.77	3.89
	1.61	1.79	87.71		4.01	
	1.61	1.79	90.01		3.70	
	1.61	1.79	84.41		3.33	

	1.61	1.79	89.32		4.63	
Group B	2.37	1.93	92.77	85.90	3.98	4.01
	2.37	1.93	78.83		3.87	
	2.37	1.93	85.29		4.02	
	2.37	1.93	84.56		4.02	
	2.37	1.93	84.61		4.14	
Group C	4.16	2.01	88.87	88.88	3.80	4.12
	4.16	2.01	96.90		4.53	
	4.16	2.01	89.75		4.19	
	4.16	2.01	85.43		4.30	
	4.16	2.01	83.45		3.79	
			Confining stress = 5.0% of σ_{bc}			
Group A	1.61	3.59	94.31	98.00	3.76	3.80
	1.61	3.59	98.07		3.9	
	1.61	3.59	97.69		3.72	
	1.61	3.59	100.06		3.71	
	1.61	3.59	99.89		3.92	
Group B	2.37	3.86	89.48	97.26	4.16	4.44
	2.37	3.86	88.74		4.01	
	2.37	3.86	107.97		5.05	
	2.37	3.86	102.86		4.58	
	2.37	3.86	108.58		4.38	
Group C	4.16	4.02	95.08	94.31	3.83	3.89
	4.16	4.02	94.23		3.85	
	4.16	4.02	93.49		4.15	
	4.16	4.02	94.22		3.67	
	4.16	4.02	94.52		3.99	

Fig. 3- 13 shows the variation of triaxial compressive strength σ_{tc} and modulus with respect to the C_p under confining stresses of 2.5% and 5.0% of their σ_{bc} respectively. The plot did not show any clear trend in the triaxial compressive strength with an increase in the C_p. Fig. 3- 13a shows that the average strength decreased from 87.91 MPa to 85.90 MPa when plane cohesive strength increased from 1.61 MPa to 2.37 MPa. However, the average strength increased back to 88.88 MPa when C_p increased to 4.16 MPa from 2.37 MPa. In the triaxial tests under a confining stress of 5% of σ_{bc}, the average strength decreased marginally when C_p increased, as shown in Fig. 3- 13c. The scatter points in Fig. 3- 13a and Fig. 3- 13c at each C_p value are extensive, and their values under different C_p stay close. The results showed that the confining stress reduced the effect of C_p on the SLR strength. In other words, when applying confining stress, the C_p showed less effect on the SLR strength.

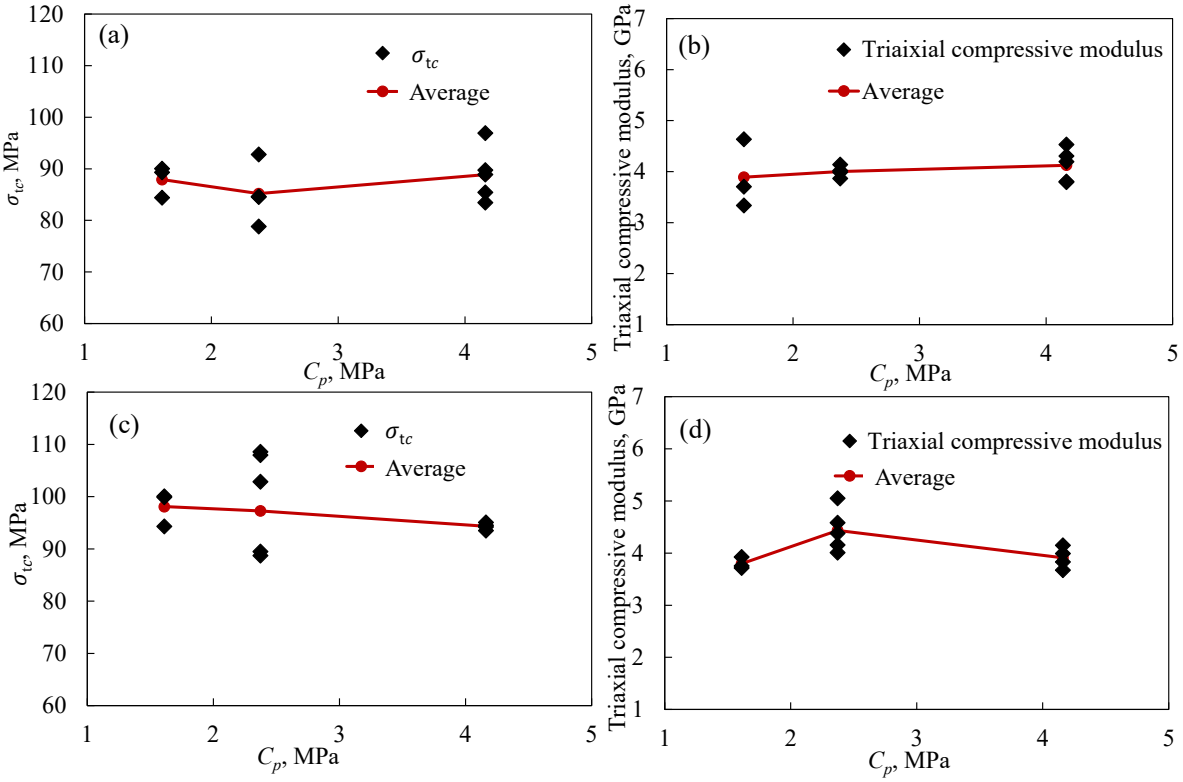

Fig. 3- 13 Variation of (a) triaxial compressive strength σ_{tc}, (b) triaxial compressive modulus under confining stress of 2.5% of σ_{bc}, and (c, d) those under confining stress of 5.0% of σ_{bc} with various C_p

3.4.2 C_p effect on failure modes under biaxial stress

This section investigates failure modes of SLR specimens with variable magnitude of C_p; it also analyzes the biaxial stress condition to investigate the effect of C_p on the mechanical behavior of SLR. This section describes the failure mode by failure type (i.e., shear, spalling or splitting), failure location, and failure plane angle θ in the specimens. The failure plane angle θ is defined as the angle between the normal to the plane and σ_3 direction, as shown in Fig. 3- 14. Fig. 3- 15 depicts the typical failure modes of the three groups of SLR specimens subjected to biaxial stress.

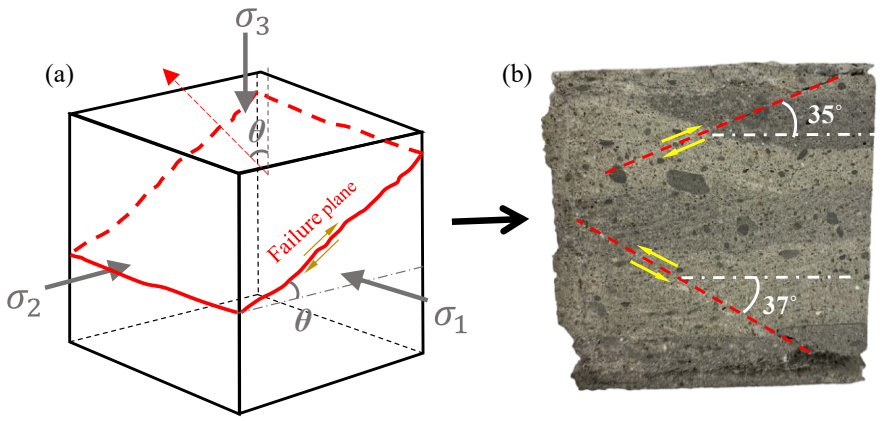

Fig. 3- 14 (a) Illustration of failure plane and measurement of failure plane angle θ, (b) Photographs of a faulted SLR specimen indicating unambiguous failure plane angles of 35° and 37°

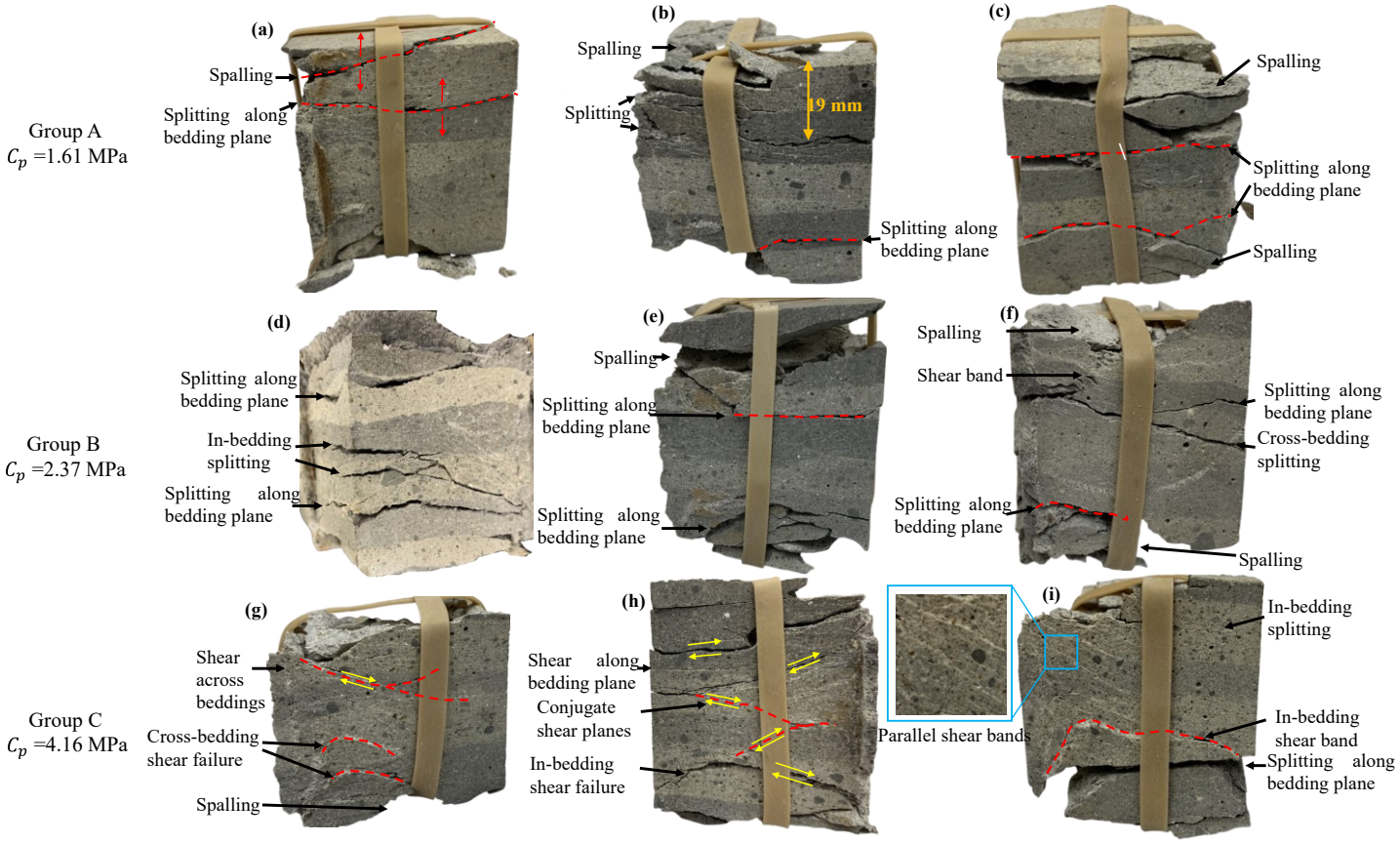

Fig. 3- 15 Failure mode of (a)-(c) group A, (d)-(f) group B, (g)-(i) group C subjected to biaxial stress

Fig. 3- 15a to c show typical failure modes of our SLR specimen group A (C_p =1.61 MPa) when subjected to biaxial stress conditions. Generally, group A is dominantly characterized by failure in spalling at the unconfined ends (top and bottom ends), followed by splitting along bedding planes. Intense spalling occurred at both unconfined ends in every specimen of group A. The central section of the SLR specimen either remained intact (Fig. 3- 15a, b) or split along the bedding

planes (Fig. 3- 15c). We observed the deepest failure location as 19 mm (37.5% of the specimen width) into the specimen as shown in Fig. 3- 15b, indicating that the failure rarely reaches the central portion of the SLR specimens when C_p=1.61 MPa. Both the spalling failure planes and splitting failure planes are nearly perpendicular to the σ_3 (θ=0).

Fig. 3- 15d to f show typical failure modes of the SLR specimen group B (C_p =2.37 MPa). Group B with a higher C_p shares similar modes with group A. For example, all specimens show the spalling at the unconfined ends and splitting along bedding planes near the unconfined ends as depicted through Fig. 3- 15d to f. However, we also observed some new characteristics. For instance, Fig. 3- 15d presents two in-bedding splitting fractures in the central portion, as opposed to group A where splitting only occurred near the unconfined ends and only happened along the bedding plane. We also observed cross-bedding splitting with a plane angle of approximately θ=15˚ in the central portion in Fig. 3- 15f. This splitting not along the bedding was due to the increase of C_p since the stronger bedding plane was less likely to fail. Moreover, shear band occurred in group B as shown in Fig. 3- 15d. This failure is similar to that of intact rocks under biaxial tests (Garg, 2018). Section 3.5 discusses this comparison. In fact, the in-bedding, cross-bedding split indicated that the increment of C_p caused the intact rock-like failure.

When the C_p increased to 4.16 MPa, the failure mode of the SLR specimens unambiguously evolved into intact rock-like modes, as depicted in Fig. 3- 15g to i. Fig. 3- 15g to i illustrate that the failure planes are dominantly shear planes, developed both near the unconfined ends and in the central portions. Only one splitting along the bedding plane occurred in the tests of group C, as shown in Fig. 3- 15i. A dominating shear band developed in the bottom bedding in Fig. 3- 15i. The dominating shear band is curved at its left end. The possible explanation for this is that the friction effect of the loading platen constraint interrupted the propagation of this shear failure. In addition to the shear that developed along the bedding plane in Fig. 3- 15h, all the shear planes are neither developed in one bedding or cross multiple beddings. We also observed multiple parallel shear bands and conjugate failure planes, as shown in Fig. 3- 15I, which both sheared across beddings. The shear bands demonstrate that the shear cracks are well-developed in these areas and the SLR specimens are heavily damaged. Therefore, we concluded that the increase in C_p of laminated rock in biaxial stress conditions caused the failure mode change from splitting along bedding planes at unconfined ends to in-bedding splitting or cross-bedding shear.

3.4.3 C_p effect on failure modes under triaxial stress

3.4.3.1 Failure mode under confining stress of 2.5% of σ_{bc}

Fig. 3- 16 presents the typical failure modes of three groups of SLR specimens subjected to confining stress of 2.5% of their σ_{bc}. Generally, all three groups present dominant shear failure regardless of the C_p. The splitting frequently observed in biaxial tests did not occur. Instead, Fig. 3- 16a to c and Fig. 3- 16g to f show shear failure occurring predominantly at the confining ends.

Group A presents multiple shear planes distributed through the whole specimen. This group had the ends near the confining platen sheared into thin slices. In the case of Fig. 3- 16a, parallel failure planes penetrated the specimen with a low plane angle. Fig. 3- 16a also presents a shear plane along the bedding plane. Fig. 3- 16b and c show intense parallel shear bands, demonstrating that shear failure heavily damaged the SLR specimens when C_p=1.61 MPa.

SLR specimens with higher C_p showed less damage compared to group A. Fig. 3- 16d to f show that group B with C_p=2.37 MPa failed in a few single dominant planes instead of intense parallel shear planes, as opposed to group A. We did not observe sheared slices at the confining ends in group A, indicating that the increase in C_p decreased the degree of shear failure. In addition, Fig. 3- 16e shows one shear plane along the bedding plane, demonstrating the effect of the bedding plane. When the C_p increased to 4.16 MPa as shown in Fig. 3- 16g to i, the SLR specimens failed in dominated conjugate shear planes, which are seldomly observed in group A and group B. This demonstrated that the increase in C_p caused laminated specimens to fail in modes similar to intact rocks (Garg, 2018).

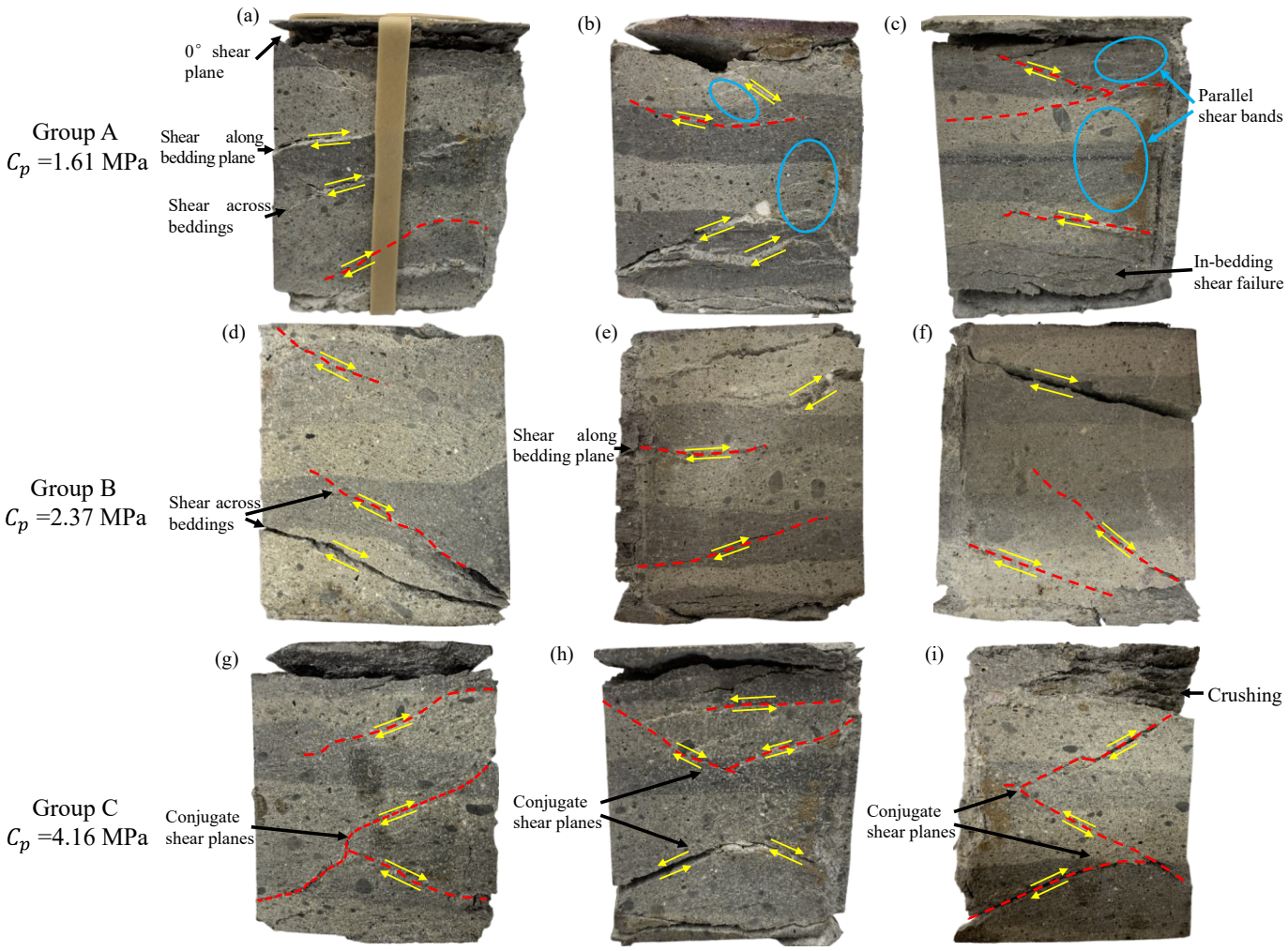

Fig. 3- 16 Failure mode of (a)-(c) group A, (d)-(f) group B, (g)-(i) group C under triaxial test with confining stress of 2.5% of σ_{bc}

3.4.3.2 Failure mode under confining stress of 5% of σ_{bc}

Fig. 3- 17 depicts typical failure modes of triaxial tests with a confining stress of 5% of their σ_{bc}. Generally, the failed specimens show the same characteristics observed from triaxial tests with a confining stress of 2.5% of σ_{bc}. For instance, group A had an extensive shear failure with low failure plane angles while having few shear planes along the bedding planes, as shown in Fig. 3- 17a and c. Groups B and C with higher C_p present conjugate shear planes with larger failure plane angles as shown in Fig. 3- 17d to f and g to I, respectively. However, the confining stress of 5% of σ_{bc} introduced an important phenomenon. Fig. 3- 17b and c show unambiguous compaction bands. The occurrence of compaction bands is consistent with the true triaxial results of Bentheim sandstone (Ma and Haimson, 2016). This phenomenon is indicative of grain crushing, signifying the specimens in the ductile region (Eichhubl et al., 2010). In addition, all the compaction bands

in Fig. 3- 17b develop along the bedding planes. The high confining stress crush grains are distributed along the bedding plane prior to the grains distributed in the beddings. On the other hand, Fig. 3- 17d to f and g to i do not present any compaction bands, indicating that higher C_p prevents the SLR from showing severe ductile behaviors.

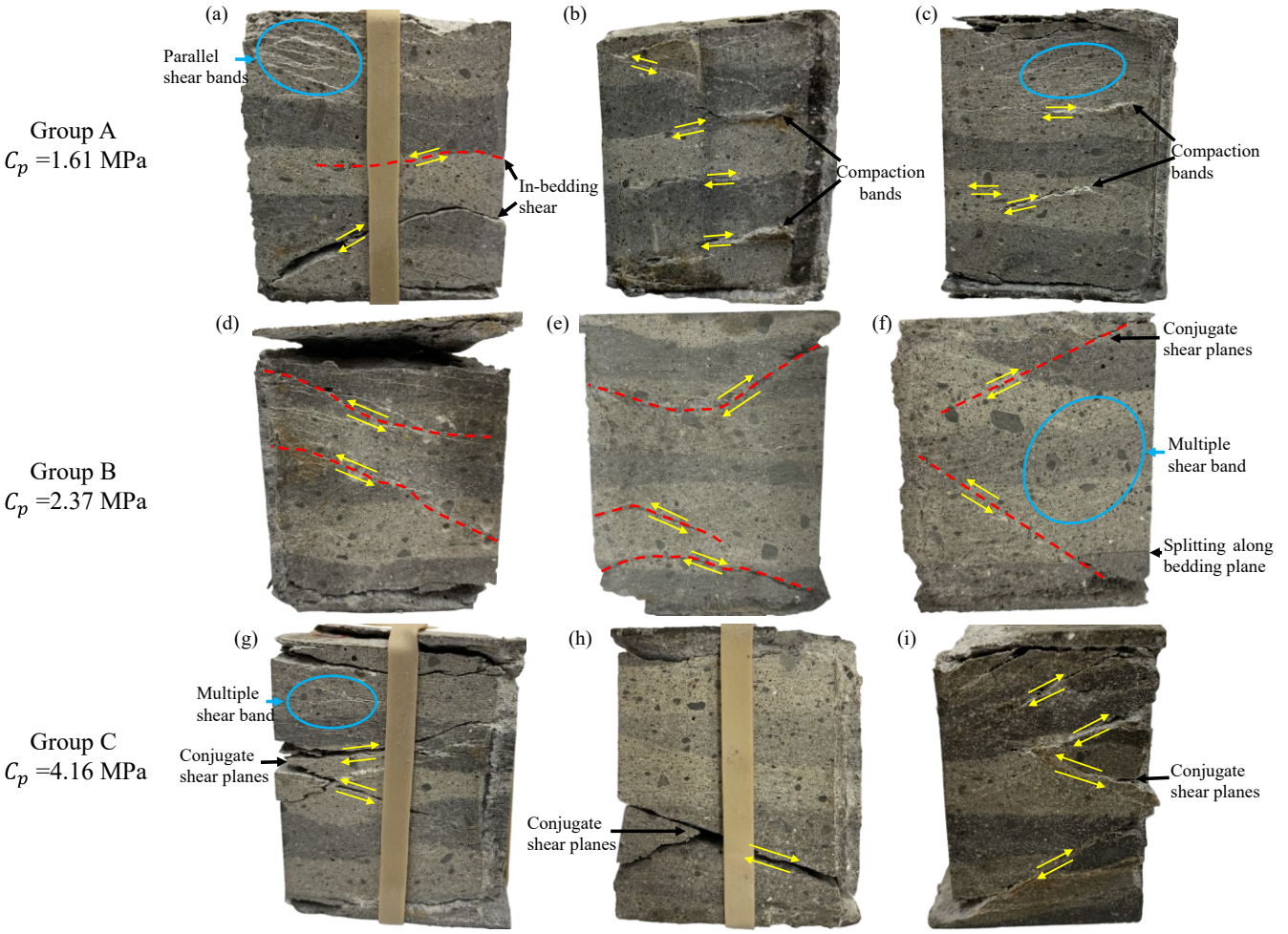

Fig. 3- 17 Failure mode of (a)-(c) group A, (d)-(f) group B, (g)-(i) group C under triaxial test with confining stress of 5% of σ_{bc}

3.4.4 Failure plane variation

The development of failure planes accompanies the failure process in the rock. Although the failure planes are locally irregular, their overall orientation is characterized by a failure plane angle θ. Table 3- 3 lists all the visible failure planes of these three groups of SLR specimens subjected to each stress condition and their measured failure plane angle. This does not include failure planes near the confining platen (within 5mm from the confining platen).

Table 3- 3 Failure plane types and angles of SLR specimens under various stress conditions

		Biaxial (σ_3=0)			$\sigma_3 = 0.025\sigma_{bc}$			$\sigma_3 = 0.05\sigma_{bc}$		
	C_p, MPa	Plane type	Plane angle, °	Average, °	Plane type	Plane angle, °	Average, °	Plane type	Plane angle, °	Average, °
Group A	1.61	Splitting	0	0.0	Shear	8	16.4	Shear	0	6.8
		Splitting	0		Shear	20		Shear	21	
		Splitting	0		Shear	29		Shear	0	
		Splitting	0		Shear	22		Shear	0	
		Splitting			Shear	34		Shear	15	
					Shear	0		Shear	0	
					Shear	10		Shear	0	
					Shear	10		Shear	18	
					Shear	11				
					Shear	20				
Group B	2.37	Splitting	0	7.1	Shear	27	22.0	Shear	25	23.5
		Splitting	0		Shear	35		Shear	24	
		Splitting	0		Shear	24		Shear	30	
		Splitting	12		Shear	21		Shear	16	
		Splitting	0		Shear	0		Shear	20	
		Splitting	0		Shear	20		Shear	15	
		Splitting	18		Shear	37		Shear	33	
		Shear	27		Shear	20		Shear	25	
					Shear	14				
Group C	4.16	Shear	15	23.6	Shear	24	24.2	Shear	18	24.0
		Shear	18		Shear	23		Shear	20	
		Shear	22		Shear	25		Shear	22	
		Shear	20		Shear	31		Shear	29	
		Shear	21		Shear	19		Shear	22	
		Shear	30		Shear	8		Shear	24	
		Shear	31		Shear	29		Shear	33	
		Shear	30		Shear	22				
		Shear	25		Shear	25				
					Shear	29				
					Shear	31				

Note: The wavy plane was estimated.

Multiple shear bands were not displayed, only planes/bands with width were counted.

Failure planes near the confining platen were not counted when measuring the failure plane angles to rule out the deviation caused by end constraint of the confining platen.

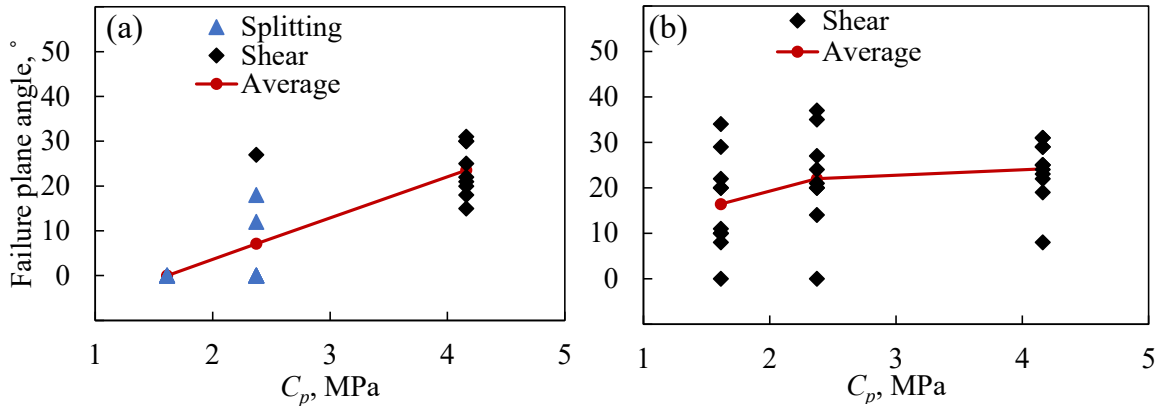

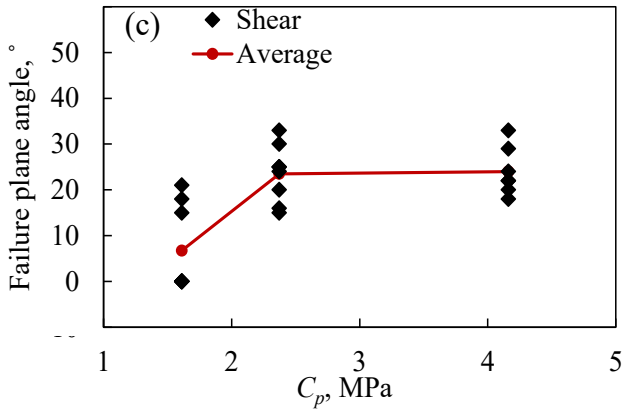

Fig. 3- 18 Variation of failure plane angles with C_p under (a) biaxial tests, (b) confining stress of 2.5% of σ_{bc}, (c) confining stress of 5% of σ_{bc}

Fig. 3- 18 plots variation of each failure plane angle against the SLR C_p, presenting that the average plane angle increases with the increase of C_p under each stress condition. For instance, Fig. 3- 18a shows that the average failure plane increased from 0° at C_p of 1.61 MPa to 23.6° at C_p of 4.16 MPa. In addition, with an increase in the C_p the shear plane increased significantly in the biaxial tests. For instance, when the C_p is 1.61 MPa, we observed no shear plane in the test. When the C_p is 2.37 MPa, we observed one shear plane out of eight planes. When the C_p increases to 4.16 MPa, failure planes/bands are all in shear.

However, the monotonously increasing trend is not as prominent when confining stress is applied, as shown in Fig. 3- 18b and c. Though the average plane angle increases slightly in the case of confining stress of 2.5% of σ_{bc} shown in Fig. 3- 18b, the extensively distributed data sets at different C_p are actually close in value. Fig. 3- 18c generally presents a similar scenario in the case of confining stress of 5% of σ_{bc}. This phenomenon indicates that under confining stress, the effect of C_p on the failure plane decreased.

3.4.5 Deformability

This research recorded the load-displacement data during each test and transformed it into stress-strain variation based on the geometric parameters provided in section 3.3 Fig. 3- 19 presents the typical stress-strain relationship of SLR specimens with various C_p under different stress conditions.

To characterize rock deformability, it is convenient to divide the curve into three distinct segments. “Segment I” (in blue) covers initial deformation and elastic response. “Segment II” (in red) begins

with a departure from linearity, exhibiting onset of failure, and ends when reaching peak stress. The post-failure response corresponds to "segment III" (in green). We observed a nonuniform region in segment I in each test, which lasted up to a strain of 0.04. This was due to the squeezing of the fiber cardboard. Segment II depicted the failure characteristics during the yielding process of specimens with various C_p.

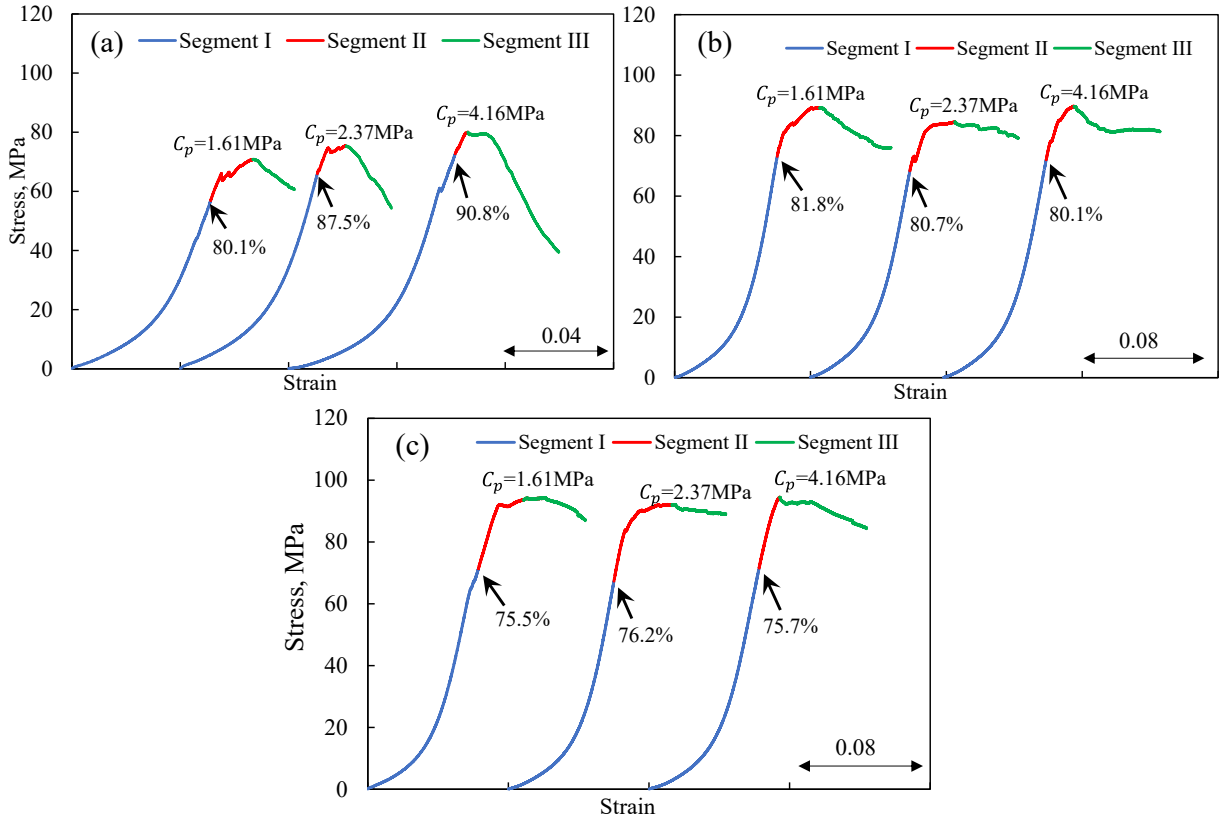

Fig. 3- 19 Stress-strain relationship of SLR with various C_p under (a) biaxial stress condition, (b) triaxial stress condition with confining stress of 2.5% of σ_{bc}, and (c) triaxial stress condition with confining stress of 5% of σ_{bc} (black arrows signify failure onset of each curve, in percentage of peak stress of this curve)

To discuss the effect of C_p on the failure onset of the SLR specimens, this research calculated the onset point of segment II during each test. The exact stress level at which the stress-strain curve departs from linearity is hard to examine visually since the curve gradually slopes. Therefore, it is necessary to calculate the derivative of stress with respect to strain and plot it against the strain. A change in the derivative represents the departure from the linear stress-strain relationship. The departure behavior is considered as the onset of inelastic deformation, leading to specimen failure.

After determining the onset of failure, this research then quantified the amount of inelastic strain. In biaxial tests shown in Fig. 3- 19a, these three curves have an inelastic strain of 0.016 (from

0.051 to 0.067), 0.011 (from 0.086 to 0.097), and 0.005 (from 0.062 to 0.067) respectively. Therefore, we concluded that the duration of the failure process before peak stress decreases with the increase of the C_p. The Fig. 3- 19b and c triaxial tests show this same trend. For example, the amount of inelastic strain of these three curves when confining stress of 5% of their σ_{bc} is applied are 0.037, 0.029, and 0.012 respectively, decreasing with the increase of C_p.

Moreover, the failure onset stress level differs with C_p. For instance, in the biaxial test shown in Fig. 3- 19a, the curve of C_p=1.61 MPa has an onset point of 80.1% of its peak stress, while curves of C_p=2.37 MPa and C_p=4.16 MPa have an onset point of 87.5% and 90.8% of their peak loads respectively. This signifies that the increase of C_p increases the threshold to initiate SLR failure. However, the confining stress alleviates this trend. For instance, the onset stress levels of these three groups are 81.8%, 80.7%, and 80.1% of their peak stress in the case when applying 2.5% of σ_{bc}, and 75.5%, 76.2%, and 75.7% respectively when applying 5% of σ_{bc}, as shown in Fig. 3- 19b and c. Both scenarios demonstrate the threshold to initiate SLR failure stays relatively stable between various C_p when applying confining stress instead of increasing with the increase of C_p as observed in biaxial tests.

In addition, we observed a change in the shape of segment II in these three curves. Fig. 3- 19a shows multiple noticeable peaks in segment II in the curve of C_p=1.61 MPa. This is indicative of splitting failure along the bedding planes depicted in Fig. 3- 15. However, with the increase of C_p, the multiple peaks become ambiguous. For instance, the curve of C_p=2.37 MPa has only one observable sub peak, and no subpeak occurs in the curve of C_p=4.16 MPa. Similarly, the shape change of segment II among these three curves is alleviated by applying confining stress of 2.5% of σ_{bc} and disappears entirely by applying 5.0% of σ_{bc}, as shown in Fig. 3- 19b and c respectively. This phenomenon confirmed the conclusion that the confining stress mentioned in the failure mode observation of section 3.4.3 constrained the splitting and spalling. In addition, it is noticeable that in segment III of Fig. 3- 19a, the stress decreases with the increase of strain, showing typical brittle behavior. However, in Fig. 3- 19b and c, segment III remains relatively flat after peak load, signifying that SLR specimens showed ductile behavior when under triaxial stress conditions.

3.5 Discussion

Using the synthetic laminated rocks (SLR) with various bedding plane cohesive strength (C_p), this section investigated the effect of C_p on the mechanical behavior of SLR, including the strength, failure modes, and deformability. It then compared results from the test with various published results to validate the accuracy of the results.

When observing the compressive strength under biaxial tests, the trend of biaxial compressive strength varying with C_p differs from Jaeger's Plane of Weakness model (Jaeger, 1960b) wherein the laminated rock strength does not vary with C_p, as shown by the solid lines in Fig. 3- 20a. This is because the ideal condition-based analytical solution does not consider the waviness of the bedding planes. Instead, it looks at the beddings and bedding planes as perfectly flat. However, the beddings casted in the present work were wavy (not perfectly flat), as seen in the failure mode figures in section 3.4.2. In fact, researchers have noticed this difference for years. For example, when validating the transversely isotropic model with analytical solution, Park et al. (2018) found that the bedding plane bumpiness in their model caused an increase in the uniaxial compressive strength of the transversely isotropic model, as shown by the scatters at β=90˚ in Fig. 3- 20a. Fig. 3- 20b plots the strength against C_p, showing that at an inclination angle of 90˚ the strength of the model increases with the plane cohesive strength, which is agreement with SLR test results in Fig. 3- 12.

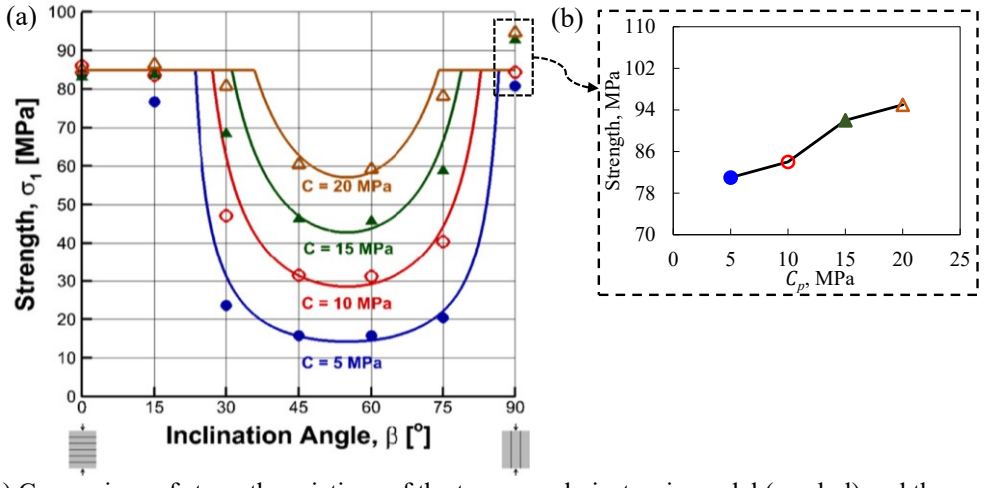

Fig. 3- 20 (a) Comparison of strength variations of the transversely isotropic model (symbol) and those of analytical solution (line) with respect to various inclination angles under different plane cohesive strength (Park et al., 2018), and (b) variation of strength with respect to plane cohesive strength under inclination angle of 90˚

Additionally, the observed trend of biaxial compressive modulus, increasing with C_p, is different from the analytical solution of the elastic modulus with an inclination angle of β, which is calculated as shown in Eq. 3-1 (Amadei, 1982):

$$\frac{1}{E_\beta} = \frac{1}{E_r} + cos^2\beta \left(\frac{cos^2\beta}{k_n\delta} + \frac{sin^2\beta}{k_n\delta}\right) \quad \text{(Eq. 3-1)}$$

where E_r is the elastic modulus of the beddings, δ is the spacing of the bedding planes, and k_n and k_s are the normal and shear stiffness of the bedding planes, respectively. When β=90˚, this analytical solution presents $\frac{1}{E_{90}} = \frac{1}{E_r}$, demonstrating the macro modulus of the laminated model does not change with the bedding plane properties. We can also attribute this to the waviness of the bedding planes in our SLR specimens. This difference was also present in the bonded-particle discrete element modeling of transversely isotropic rock (Park et al., 2018) wherein researchers noted that the measured elastic modulus of their transversely isotropic model with the 90° inclination angle increased in accordance with the increasing C_p. They attributed this difference to the bumpiness of the bedding plane in their model. In conclusion, we argue that the scenario observed in our SLR specimen could be more realistic than the results of the analytical solution.

Triaxial tests demonstrated that confining stress reduced the effect of C_p on the SLR strength when comparing strength variations under biaxial tests. In addition, the scatter points values under different C_p are close, as illustrated in Fig. 3- 13b and d in section 3.4.1. This indicates that the monotonically increasing trend of the SLR stiffness with respect to the C_p observed in biaxial tests was no longer present after applying confining stress. These results validate the function of the support system from the experimental perspective. It can be extended that when the support system applied support stress to the exposed laminated roof in underground entries, the roof strength and stiffness reduction caused by bedding planes can be relieved.

C_p has a significant impact on the failure modes of our SLR specimens. The failure modes in group A to group C showed a transition from laminated rock-like failure to intact rock-like failure. When the bedding plane strength increased, the laminated rock failed like an intact rock. The transition includes failure location, failure type, and failure plane angle. Especially in a biaxial stress state ($\sigma_3 = 0$), the SLR specimens are typically characterized by failing in intense spalling and splitting near the unconfined ends. The multiple peaks in their stress-strain curves presented in section 3.4.5

confirmed this phenomenon. This is in qualitative agreement with actual shale failure under biaxial tests performed by Arora and Mishra (2015). Moreover, increasing the C_p caused shear failure cutting across beddings. This transition agrees well with field observations. Mark and Molinda (2007) made a statement based on numerous empirical observations: "if most of the failure surfaces cut across bedding, then the strength of the bedding is most likely equal to or greater than that of the intact rock", which empirically validated the SLR specimens. From the perspective of failure location, increasing the C_p caused the occurrence of failure in the central portion of the specimens, which was not observed in group A specimens with lower C_p. This characteristic corresponds to that observed from biaxial tests on intact rocks of Berea sandstone, conducted by Garg (2018) wherein the intact rocks also fail in shear at their central portion. Section 4.2.3 quantitively discussed the failure angle. The failure planes generally deviate from parallel to bedding planes when the C_p increases. In triaxial cases, although the C_p brings a similar impact on the SLR specimens as that in biaxial tests, the confining stress alleviates the damage in comparison to biaxial tests. It is interesting to note that a confining stress of 5% of σ_{bc} introduced crushing of the grains along the bedding plane. The grain crushing signifies that the specimens entered an early ductile regime, which the strain-stress curves in section 3.4.5 confirmed. This may result in strength reduction of the bedding planes, causing worse engineering problems in the field. From this point of view, confining stress may cause problems if the magnitude is inappropriately high.

Deformability observation shows that SLR specimens with higher C_p fail with less deformation under the biaxial stress state. The possible explanation is that higher C_p brings higher stiffness of the laminated specimen and decreased deformability. Stress-strain curve shape changes with C_p. Considering the failure mode observed in section 3.4, the possible explanation is that the bedding plane splitting occurred in a domino sequence when C_p is low, while specimens with high C_p failed in dominating shear. In fact, Arora and Mishra's biaxial test (2015) on the shale from the Illinois no. 6 seam found the shale split in a domino effect with the unconfined zones failing first. This is in qualitative agreement with the results presented here.

3.6 Conclusions

This chapter explored the effect of bedding plane strength on the mechanical behavior of synthetic laminated rocks (SLR) subjected to various stress conditions, including biaxial stress conditions ($\sigma_3 = 0$) and triaxial stress conditions with different confining stresses. This chapter paid

particular attention to the influence of bedding plane cohesive strength (C_p) on the strength, failure modes, and deformability of the SLR specimens. The following paragraphs are summaries of this chapter's main conclusions.

Comparison of different methods to vary C_p demonstrates that one can vary the C_p of the bedding plane in SLR by applying different normal stresses when curing the concrete mixture. Brazilian splitting tests on SLR with different orientations of bedding planes show good consistency in failure strength and failure modes with actual shale specimens, which validates the capacity of the SLR to replicate the actual laminated rock.

C_p poses an effect on SLR strength, modulus, and failure modes in biaxial stress conditions. The biaxial compressive strength and modulus of SLR increases with the increment of C_p. Increasing the C_p introduces the transition of the failure model from typical laminated rock-like characteristics to intact rock-like characteristics. First, the SLR specimens with low C_p fail in splitting and spalling failure, while shear failure dominates in SLR specimens with higher C_p. Second, failure happens mainly near the unconfined ends of SLR specimens, but increasing C_p causes failure at the central portion of the SLR specimens. Finally, the failure plane deviates from the direction of parallel to bedding planes when the C_p increases.

A similar trend occurs in triaxial stress conditions, except that application of confining stress relieves the damage of SLR specimens and constrains the effect of C_p on SLR strength and modulus. On the other hand, inappropriately high confining stress may cause bedding plane strength reduction, since grain crushing along the bedding planes occurred under confining stress of 5% of σ_{bc}.

The duration of the failure process before reaching σ_{bc} decreases with the increase of the C_p according to deformability analysis of the SLR subjected to biaxial stress. However, the threshold stress level to initiate SLR failure increases with C_p. One can further validate the function of confining stress by relieving both trends observed here.

Our results describe the detailed effect of C_p on the mechanical behavior of laminated rocks and provide a better understanding of the influence of C_p when considering laminated roof support in underground coal mines.

CHAPTER 4 DEM ANALYSIS OF THE EFFECT OF LAMINATION PROPERTIES ON THE STABILITY OF AN UNDERGROUND COAL MINE ENTRY WITH LAMINATED SHALE ROOF

4.1 Introduction

Shale roof in underground coal mines presents various lamination properties. Laboratory tests on synthetic laminated rock showed that bedding plane strength posed a significant effect on the geomechanical behavior of laminated rock. Therefore, research should investigate bedding plane strength and other lamination properties in laminated shale to provide support for understanding their effect on shale roof failure. Although researchers have studied influential factors such as horizontal stress and mine entry orientation on roof stability for decades (Becker, 2013; Gao and Stead, 2013; Garg, 2018; P. Zhang et al., 2018), research on the detailed effect of these lamination properties, including bedding plane spacing and bedding plane strength, on a field-scale entry is not yet present.

This chapter extends the investigation of the effect of lamination properties on laminated rock to the stability of the shale roof. It establishes an underground entry model with a laminated roof using DEM and investigates the effects of lamination properties of shale on the stability of the modeled entry. The microparameters of the entry model were calibrated with laboratory data. Next, a parametric analysis investigated the effect and sensitivity of the bedding plane spacing, bedding plane strength, and supporting pressure on the roof stability and stress distribution inside the laminated roof.

4.2 Calibration of numerical laminated shale

PFC can develop jointed rock mass using three methods (Chiu et al., 2016): (1) bond-eliminated model, (2) band-eliminated model, and (3) smooth-joint model. Smooth-joint model is characterized by eliminating the roughness resulting from the particle arrangement. The bond-eliminated model involves applying a plane through the specimen and eliminating the bonds through the plane to separate the whole model into blocks. This method is easy to use; however, the joint face may have inestimable roughness because of the interlock between particles on the

joint face. Instead of inserting a plane without thickness, the band-eliminated model eliminates the bond within a broad band through the specimens that reduce the particle-interlocking problem. However, there is considerable difficulty in controlling the normal displacement on the joint face. In the smooth-joint model, a smooth joint intersects the particle pair to overlap and pass through each other instead of moving around one another (Itasca Consulting Group, 2019; Potyondy and Cundall, 2004). As such, this model improves the influence of these two techniques and eliminates the roughness resulting from the particle arrangement.

This chapter simulated the laminated shale roof with an assembly of 2D rigid particles bonded together. The laminated shale roof consists of laminas and distributed bedding planes. This study modeled the laminas with a linear parallel bonded model and modeled the bedding planes with a smooth-joint model (Itasca Consulting Group, 2019) provided in PFC.

This process used the Brazilian splitting test of the shale from the literature survey (He et al., 2018) for calibrating the model microparameters. The present study used the test results with inclined angles of 0°, 30°, 60°, and 90°, as shown in Table 4- 1.

Table 4- 1 Brazilian tensile strength (BTS) of the shale samples (He et al., 2018)

	Brazilian tensile strength, MPa			
θ	0˚	30˚	60˚	90˚
1	8.129	4.229	4.718	2.789
2	6.264	7.098	3.243	3.505
3	5.567	6.583	3.623	3.566
4	7.936	5.265	3.025	2.944
5	7.458	4.986	2.857	2.654
Mean	7.071	5.632	0.664	3.091

There is no efficient way to calibrate the assembly comprising both the linear parallel bond model and the smooth-joint model. Researchers must adjust the microparameters through trial and error based on observation of the failure mode and failure strength. In addition, they must scale the laboratory test results when applying them to large-scale rock mass during the calibration. The present research uses the strength reduction factor of 0.58 (Gadde et al., 2007) for the BPM with bedding planes. After multiple times of trial and error, Fig. 4- 1 presents both numerical and scaled experimental Brazilian tensile strength results of the laminated specimens at different inclined angles. Generally, the numerical model results match well with the experimental results.

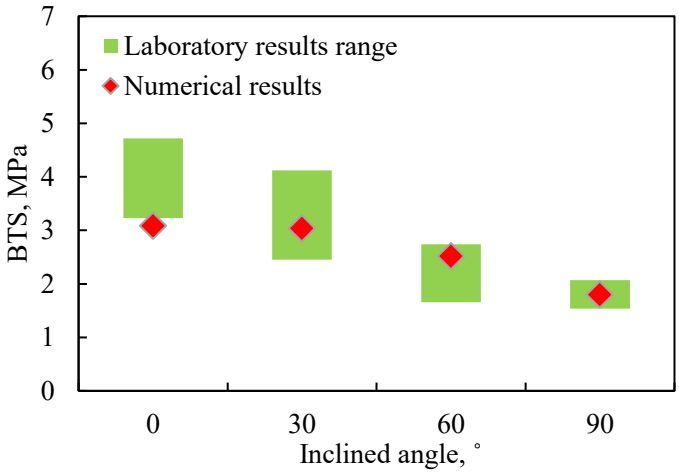

Fig. 4- 1 Comparison between numerical and experimental results of laminated specimen under Brazilian test

Fig. 4- 2 shows the typical fracture patterns for different inclined angles of the shale specimens (He et al., 2018), with the conclusion that the fracture patterns vary with the inclined angle. Central-linear/curved fracture mainly propagated along the loading axis when the orientation was 0° and 90°. In the specimens with the inclined angle of 30° and 60°, the fractures mainly developed along the bedding direction or with some orthogonal fractures. However, the failure tends to occur near the loading point in a 30° inclined specimen. Fig. 4- 3 gives the calibrated fracture patterns, where the blue lines represent the tensile cracks and the red lines represent the shear cracks. Compared with Fig. 4- 2, the fracture patterns in the numerical model match well with laboratory results. This further validated the reliability of our calibrated microparameters. The numerical models utilizing these microparameters can capture the fracturing behavior of the laminated shale.

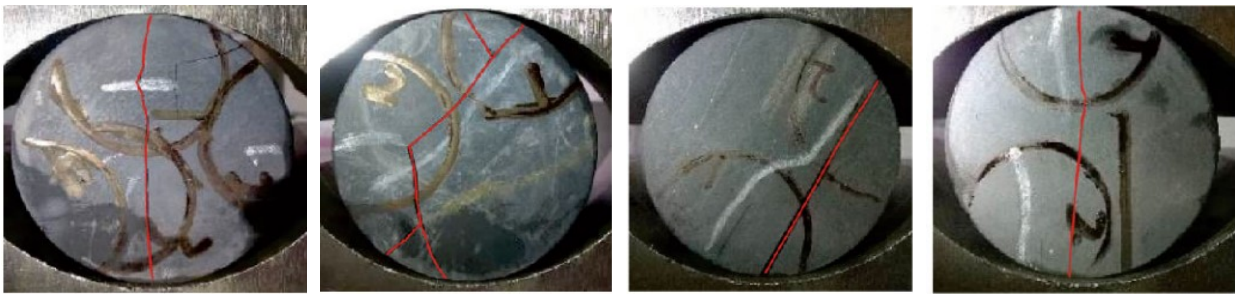

Fig. 4- 2 Fracture patterns of slate specimens with different inclined angles (He et al., 2018)

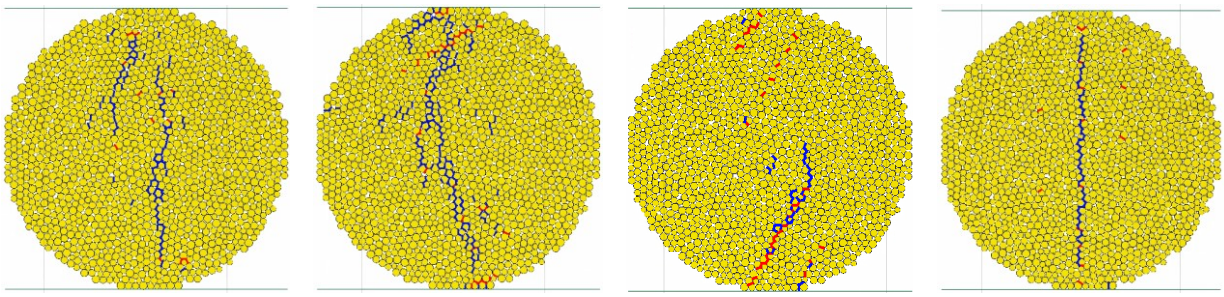

Fig. 4- 3 Fracture patterns of calibrated models

4.3 Configuration and empirical verification of the entry models

This study built its entry model in PFC which included laminated shale roof, coal seam, and floor. The model simulated the excavation of entry by deleting the particles within the entry domain. This study then investigated the roof failure modes of the intact roof and the laminated roof in comparison with filed evidence.

4.3.1 Configuration of the entry model incorporating shale roof

The objective of the present section is to investigate the effect of lamination properties on roof failure. In PFC, a slight increase in the model size significantly increases the run-time. Therefore, one must carefully consider the dimension of the model. The present study selects the dimensions of the entry model as 18 by 13.5 m. The model consists of a 3-m-thick laminated roof followed by a competent roof that has no bedding planes. Fig. 4- 4 shows the schematic diagram of the entry model. The laminated roof incorporates laminas simulated with the linear parallel bonded model and bedding planes simulated with the smooth joint model. Table 4- 2 and Table 4- 3 list the microparameters of laminas and bedding planes calibrated in section 4.2 to replicate scaled experimental results. Considering the objective of this model, the competent roof, coal body, and floor are hypothetically set as the same as the bedding parameters listed in Table 4- 2 corresponding to a linear parallel bonded model.

This set-up fixed the bottom of the model while applying vertical and horizontal stresses to the top and both sides of the model respectively, as shown in Fig. 4- 4. The model simulated the typical stress conditions that one might expect at a depth of 390 m, which typically represents a vertical stress σ_v of 10.0 MPa. For finding the minimum horizontal stress to cause roof failure, this study increased the magnitude in a step sequence. This value was defined as the critical failure stress of the model in the present study. As an example, we conducted an initial model run with horizontal

stress of 10 MPa. If roof failure did not occur, we increased horizontal stress incrementally until we observed a roof failure. In this case, the value σ_x is called critical failure stress for this model. The servo-mechanism provided in the PFC applied preset stresses to the boundaries (Itasca Consulting Group, 2019). Measurement spheres with a diameter of 0.2 m, shown as blue dots and placed above the roofline, monitored stress distributions after excavation. We also applied damping boundary conditions to remove any dynamic effects during static model runs.

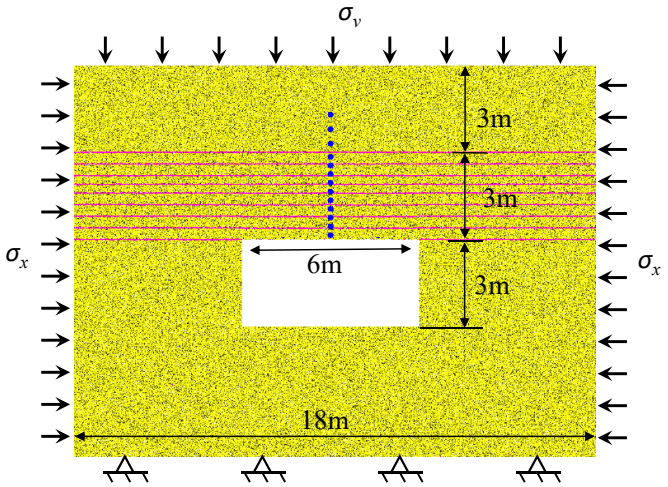

Fig. 4- 4 Schematic diagram and boundary conditions of entry model (σ_x corresponds to horizontal stress while σ_v corresponds to vertical stress; blue dots represent measure stations set in model roof)

Table 4- 2 Microparameters of laminas used in the PFC2D model

Micro-parameter	Value
Particle density, kg/m^3	2,610
Particle size, mm	10 to 15
Damping ratio	0.5
Bond gap, m	5×10^{-4}
Young's modulus of the particle, GPa	10
Young's modulus of the parallel bond, GPa	10
Ratio of normal to shear stiffness of the particle	1.0
Ratio of normal to shear stiffness of the parallel bond	1.0
Particle friction coefficient	0.7
Parallel bond tensile strength, MPa	11
Parallel bond cohesion, MPa	60
Friction angle, degree	31

Note: Microparameters listed in this table are for linear parallel bonded model
Microparameters listed in this table achieved a match with scaled laboratory results.

Table 4- 3 Microparameters of bedding planes used in the PFC2D model

Microparameter	Value
Bedding plane spacing, cm	10
Normal stiffness of smooth joint, GPa/m	100
Shear stiffness of smooth joint, GPa/m	2,000

Tensile strength of smooth joint, MPa	2
Shear strength of smooth joint, MPa	15
Friction coefficient	0.6
Contact gap, m	5×10^{-4}

Note: Microparameters listed in this table are for smooth joint model
Microparameters listed in this table achieved a match with scaled laboratory results.

4.3.2 Comparison of the laminated and nonlaminated models

This study conducted a parametric model run to compare laminated roof and models with only competent roof, and then to a model without lamination. The vertical stress remained constant at 10.0MPa. Fig. 4- 5 shows the model results with varying horizontal stresses on the immediate roof with no lamination. The colored particles represent the fragments in the specimen, and the same color indicates a piece of fragment that comprised a clump of bonded particles. Different colors of fragments indicate that the fragments separated due to the development of fractures. The model shows critical failure stress under which the model roof can stay stable with only minor spalling, as shown in Fig. 4- 5a and b. When reaching critical failure stress, however, the roof failure will continue to develop upward as shown in Fig. 4- 5c. The same phenomenon occurs for the laminated model, as shown in Fig. 4- 6c. Due to such failures, the models did not converge. However, the run did accurately obtain the critical failure stress magnitude. The two models differ significantly in failure mode. The roof failure develops into a dome shape shown in Fig. 4- 5c, while the cavity formed in the laminated model has near-vertical sides as shown in Fig. 4- 6c. The model results were similar to the failure observed in the field (Esterhuizen and Bajpayee, 2012).

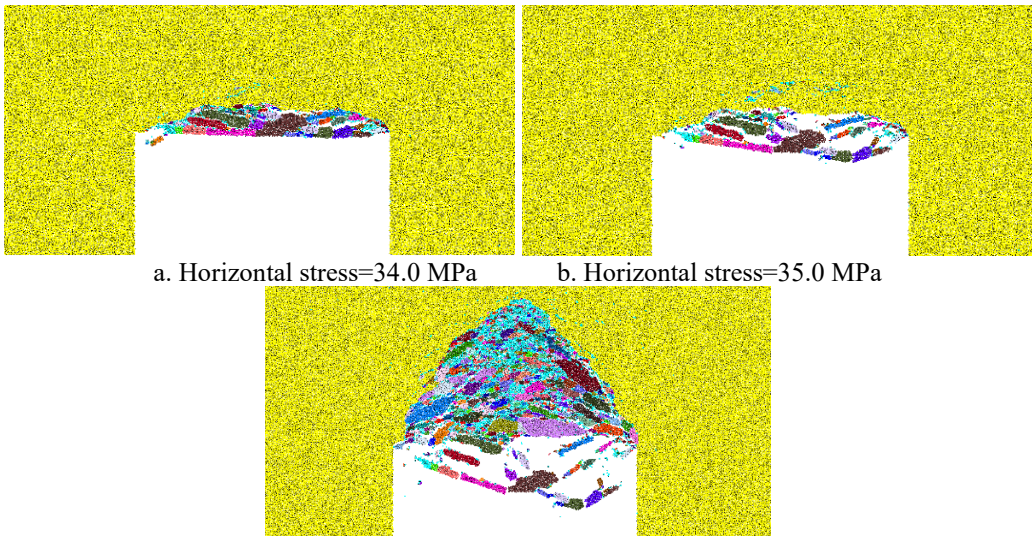

a. Horizontal stress=34.0 MPa b. Horizontal stress=35.0 MPa

c. Horizontal stress=36.0 MPa

Fig. 4- 5 Failure mode of a nonlaminated model with critical failure stress of 36.0 MPa (falling fragments kept here for illustration)

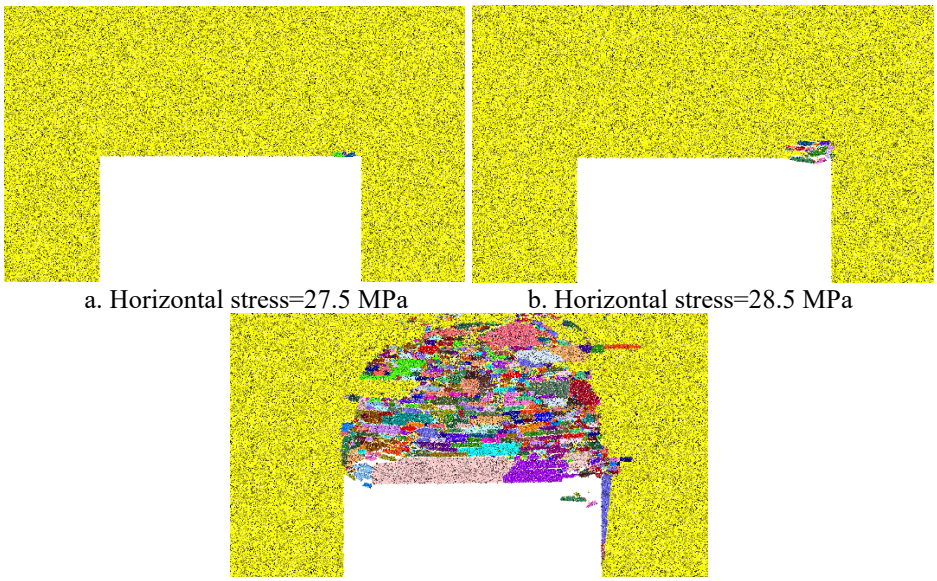

a. Horizontal stress=27.5 MPa b. Horizontal stress=28.5 MPa

c. Horizontal stress=29.0 MPa

Fig. 4- 6 Failure mode of a laminated model with critical failure stress of 29.0MPa (bedding plane spacing=10cm; falling fragments kept here for illustration)

4.4 Sensitivity analysis for geomechanical behavior of shale roof

4.4.1 Effect of bedding plane spacing

The thickness of the laminas in a laminated roof varies from tens of centimeters to less than 1 cm (Esterhuizen and Bajpayee, 2012). This thickness has a significant impact on the strength and failure development within the roof. This section studied the effect of bedding plane spacing on the failure behavior of laminated roof, conducting nine numerical simulations by changing bedding plane spacing. This process sets bedding plane spacing as 10 cm, 15 cm, 20 cm, 25 cm, 30 cm, 35 cm, 40 cm, 45 cm, and 50 cm.

Fig. 4- 7 shows the variance of critical failure stress with bedding plane spacing. This figure displays that the bedding plane spacing has a significant impact on the critical failure stress of laminated roof. Under constant vertical stress, the critical failure stress increases monotonously with an increase in the bedding plane spacing. Their variations are relatively steep before the bedding plane spacing approaches a considerable value. For example, when the bedding plane spacing is less than 25 cm, the critical failure stress gradient is around 0.32 MPa/cm. When the bedding plane spacing ranged between 25 cm and 40 cm, the gradient decreases to 0.12 MPa/cm. Furthermore, when the bedding plane spacing is larger than 40 cm, the curve becomes relatively flat. This indicates that the critical failure stress of a laminated roof is highly sensitive to the

bedding plane spacing where the bedding plane spacing is small, and the sensitivity decreases when the thickness increases to a higher magnitude.

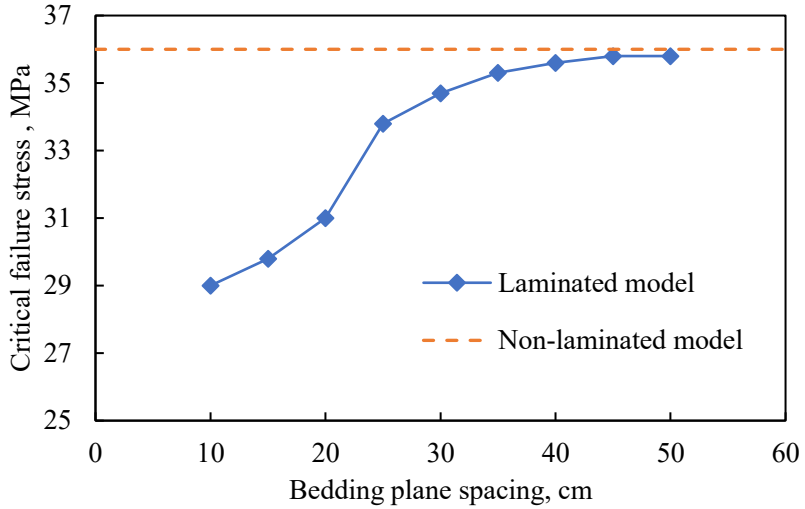

Fig. 4- 7 Effect of bedding plane spacing on critical failure stress (the red dashed line corresponds to the critical failure stress of nonlaminated model)

As a comparison, Fig. 4- 7 shows the critical failure stress of the non-laminated model, 36.0 MPa, as a red dash line. As shown in the figure, the critical failure stress of the non-laminated model becomes the upper limit of the critical failure stress of the laminated model. As shown in Fig. 4- 7, the curve keeps approaching 36.0 MPa with an increase of bedding plane spacing, and it never exceeds the limit. This demonstrates that the rock matrix that forms the laminas for given bedding planes determines the strength of the laminated roof.

In addition, this research observed stress distribution along the vertical axis in the entry roof in models with different bedding plane spacings. This research maintained vertical and horizontal stress applied to the model at 10 and 20 MPa, respectively, to observe the influence of bedding plane spacing on stress distribution in the entry roof. We selected a horizontal stress of 20 MPa because none of the models would fail under such a magnitude. We then extracted horizontal stress using the measure spheres along the entry's vertical axis in Fig. 4- 4. Fig. 4- 8 shows the horizontal stress at various depths from the roofline under bedding plane spacings of 10 cm, 20 cm, 30 cm, and nonlaminated model as a comparison. This investigation concluded that bedding plane spacing has a great impact on the stress magnitude in the laminated roof. However, the shapes of the distribution curve are similar, i.e., each curve is generally increasing within the depth of 1.65 from the roofline, then becomes relatively flat with increasing depth.

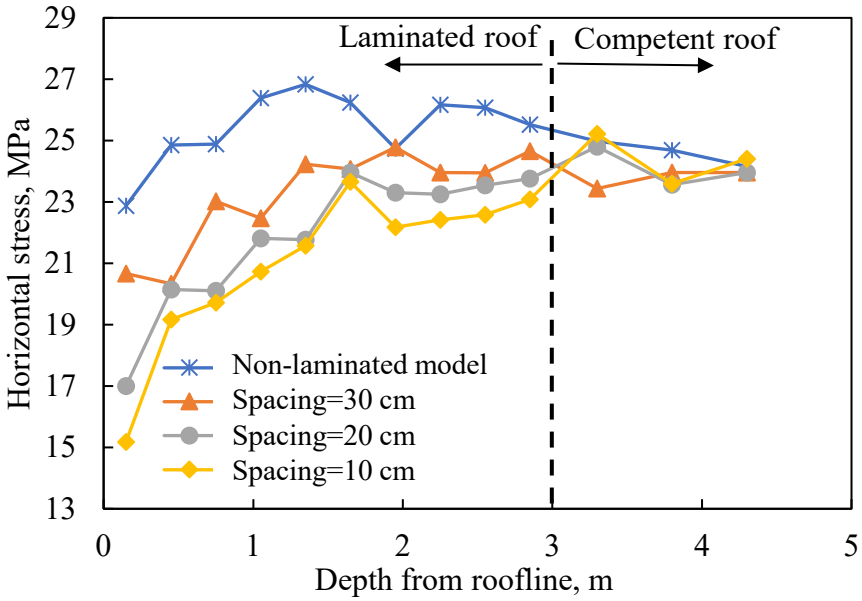

Fig. 4- 8 Effect of bedding plane spacing on stress distribution in laminated roof (black dashed line corresponds to dividing line of laminated roof and competent roof)

One can observe a significant difference among the curves under different bedding plane spacings. As shown in Fig. 4- 8, horizontal stress in a fixed depth increases with the bedding plane spacing. For example, at a depth of 1.05 m, the horizontal stress in different models has a ranking of 10 cm lamina<20 cm lamina<30 cm lamina< nonlaminated model. The same trend occurs at other depths. However, when the depth is more than 3 m, all the curves converge and show a similar flat trend. At the depth of 3.0 m, there is a clear separation between the laminated roof and competent intact roof as shown by the black dashed line in Fig. 4- 8. In addition, the impact of excavation weakens in the deeper surrounding rock. The above results indicated that bedding plane spacing has a significant effect on roof strength and stress distribution.

4.4.2 Effect of bedding plane strength

The bedding planes in the laminations produce large deformation and low strength of the laminated roof of underground entries. This section investigates the effect of bedding plane strength on the fracturing behavior of laminated roof. This section conducts fifteen numerical simulations by simultaneously changing the tensile and shear strength of the smooth-joint model (Dou et al., 2019a). The smooth joint strength in Table 4- 3 was set as a base, and the strength ratio to the base was taken as 1.5, 1.25, 1.0, 0.75, and 0.5, respectively, as shown in Table 4- 4. The remaining parameters in the numerical model was designated as constant.

Table 4- 4 Critical failure stress of the models with different plane strength

Smooth joint strength (Strength ratio)	Bedding plane spacing, cm	Critical failure stress, MPa
Tensile strength=3.0 MPa Shear strength=22.5 MPa (1.5:1)	10	30.7
	20	33.0
	30	38.5
Tensile strength=2.5 MPa Shear strength=18.75 MPa (1.25:1)	10	27.5
	20	32.0
	30	37.5
Tensile strength=2.0 MPa Shear strength=15 MPa (Set as a base)	10	29.0
	20	31.0
	30	34.7
Tensile strength=1.5 MPa Shear strength=11.25 MPa (0.75:1)	10	22.5
	20	27.8
	30	32.0
Tensile strength=1.0 MPa Shear strength=7.5 MPa (0.5:1)	10	19.1
	20	25.4
	30	27.5

The influence of smooth joint strength on the critical failure stress of the model was shown in Table 4- 4. The critical failure stress against the strength ratio with varying bedding plane spacing is shown in Fig. 4- 9. This figure shows that bedding plane strength has a significant impact on critical failure stress. Under a constant bedding plane spacing, the critical failure stress increased monotonously when the bedding plane strength ratio increased, as shown in Fig. 4- 9. A similar trend occurred in the models of 20 and 30cm-thick laminas. Some non-linear trends occurred at strength ratio=1.25 for the 10cm-thick model.

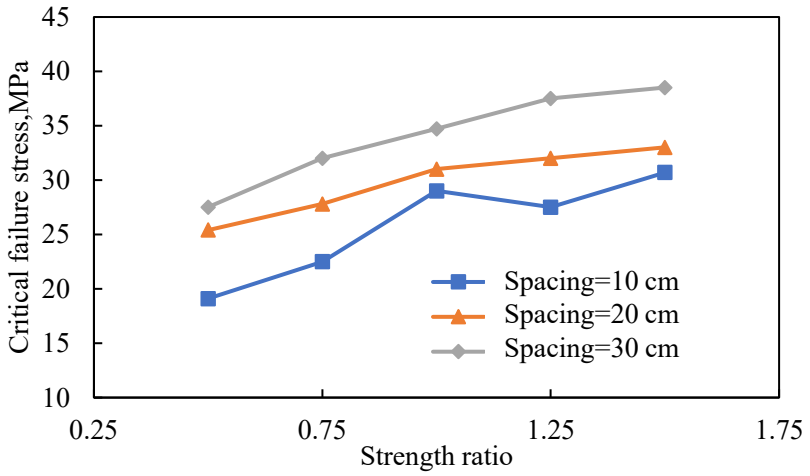

Fig. 4- 9 Effect of plane strength on critical failure strength of the models

In addition, we observed a significant gap among the curves under different bedding plane spacings. For example, when the strength ratio is equal to 0.5, the critical failure stress of the model has a ranking of 30 cm model > 20 cm model > 10 cm model. This indicated that the effect of plane strength on critical failure stress is sensitive to the bedding plane spacing of the roof. The results discussed in earlier sections showed that the bedding plane strength significantly affects the stability of the laminated roof of an underground entry. In general, the weaker bedding plane strength reduces the stability of the laminated roof.

In addition, this section investigated the effect of the strength of the bedding plane on the stress distribution in the roof using numerical simulation. This investigation conducted simulations under different bedding plane spacings of 10 cm. All numerical models had vertical and horizontal stress maintained at 10 and 20 MPa. Fig. 4- 10 shows the variations of horizontal stress with plane strength ratio under different bedding plane spacings. This analysis does not include simulation of the stress distribution of strength ratio of 0.5, as the 20 MPa horizontal stress exceeded the critical failure stress. A failed model would not reveal the stress condition induced by a laminated roof since the failure disturbed the stress distribution.

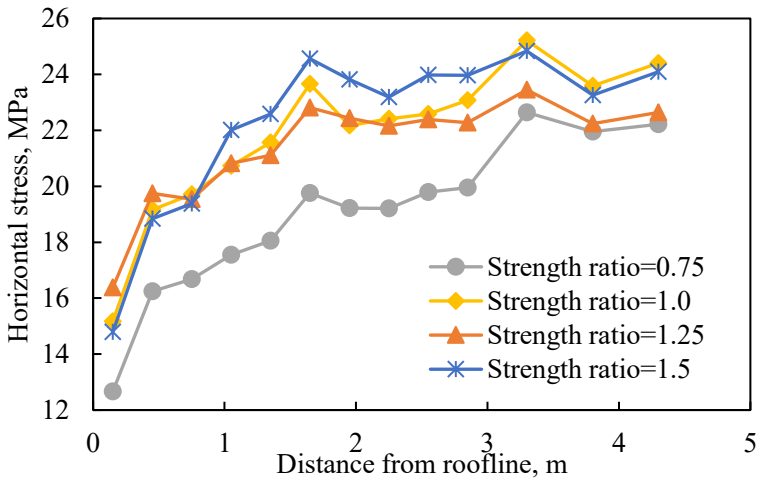

Fig. 4- 10 Effect of bedding plane strength ratio on stress distribution

Fig. 4- 10 presents the stress distribution along the axis of the cross section of the entry under different bedding plane strengths. The results support the conclusion that the stress concentration increased with an increment in bedding plane strength, as the curve with a higher strength ratio is generally above the one with a lower strength ratio. For example, for a fixed depth of 1.35 m, the horizontal stress can be ranked as strength ratio of 0.75 < strength ratio of 1.0≈strength ratio of 1.25 < strength ratio of 1.5.

4.4.3 Effect of roof support on the laminated roof

This section investigates the influence of support systems on the controlling development of the laminated roof failure. It uses the critical failure stress to evaluate the effect of a roof support system to control laminated roof failure. The investigation compares entry models with a 3.0 m-thick shale roof containing 10-cm, 20-cm and 30-cm laminations, based on their critical failure stress under different support pressures. The pre-mining vertical stress was set at 10 MPa and the horizontal stress increased monotonically until the critical failure stress.

This research adopted a pressure-application algorithm to simulate the support system in entries. Potyondy (2017) initially developed this algorithm to apply water pressure in a drill hole. It is activated in two steps. In the first step, the algorithm identified the particles within a certain gap on the free surface of the entry and connected them as a chain. In the second step, the algorithm applied a specific force on the chained particles from outside, which represents supporting pressure on the entry, as depicted in Fig. 4- 11. In Fig. 4- 11, the orange lines are the identified chain. The red arrows are the force applied perpendicular to the chain. Afterwards, this research calculated the complete model under a stepwise increase in the horizontal stress up to the critical failure stress.

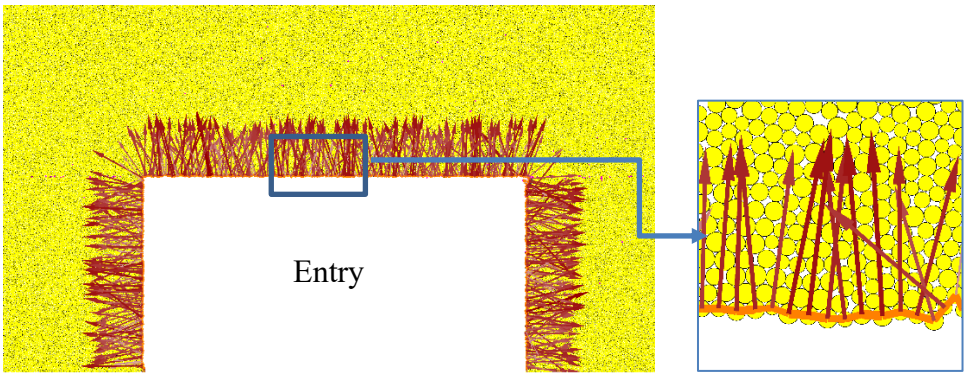

Fig. 4- 11 Algorithm for applying supporting pressure

This study analyzed five different assumed supporting pressures, 0 to 2 MPa with an interval of 0.5 MPa, in the numerical models. Typically, a support design in a 0.7×0.7 m pattern with a pre-tension load of 100 kN achieved a supporting pressure of 0.2 MPa. Therefore, the assumed supporting pressure series was only for parametric study in this section, since a confining stress of 2 MPa is impractically high in the field.

Fig. 4- 12 shows the variations of critical failure stress of the models with supporting pressure under different bedding plane spacings. The critical failure stress increased monotonously with the

increase in the support pressure. For a fixed support pressure, as bedding plane spacing increases from 10 to 30 cm, the critical failure stress of the models increased significantly. This indicated the effect of the supporting pressure to be sensitive to the bedding plane spacing. In addition, the gap between the curves of different bedding plane spacings decreased slightly when the support pressure is large in magnitude. For example, when the supporting pressure is 0.5 MPa, the gap between the 10 and the 30 cm curve is 5.0 MPa. When the support pressure increases to 2.0 MPa, the gap drops to 1.8 MPa. This indicates that bedding plane spacing has a smaller effect on roof stability for larger supporting stresses.

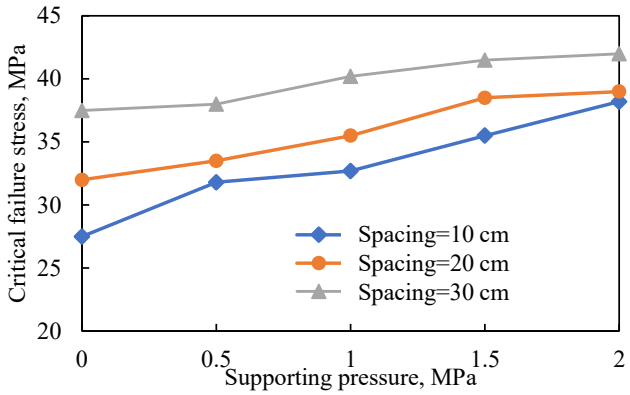

Fig. 4- 12 Effect of supporting pressure on critical failure stress

4.5 Discussion

When comparing the failure modes of the entry models with and without laminations, this research found a typical difference. The laminated roof tended to fail along a nearly vertical line at both top corners of the entry, while the intact roof failed in a dome shape, which shows good consistency with empirical and previous numerical observations. Empirically, Esterhuizen and Bajpayee (2012) stated that the laminated roof fall-caused cavities can have near-vertical sides, as opposed to dome-like failure cavities formed in rocks that are not bedded, which is exactly the scenario observed in our entry models. Numerically, our model results with the intact roof were consistent with that obtained with Trigon bonded block models (BBM) (Gao et al., 2014) shown in Fig. 4- 13a, verifying the capacity of our inputs of block material. Moreover, the laminated roof failure observed by Voronoi BBM (Coggan et al., 2012) presented similar failure modes observed in our models shown in Fig. 4- 6c, verifying the combination of block material and parameters of bedding planes.

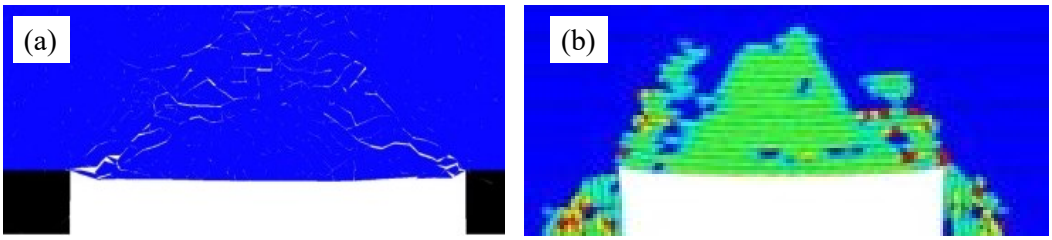

Fig. 4- 13 Roof failure model results using (a) intact roof simulated with Trigon BBM (Gao et al., 2014), and (b) laminated roof simulated with Voronoi BBM (Coggan et al., 2012)

Since the supporting conditions in our models were different from the actual entry, a direct comparison between empirical and numerical results is not possible. However, with some appropriate assumptions discussed in section 4.3.3, this research obtained ARBS values CMRR values of our models and used them for verification. In fact, Abousleiman (2020) made similar assumptions in their DEM models incorporating laminated roof. Their models categorized cutter caving and delamination of the laminated roof as unstable and obtained good agreement with the empirically- derived ARBS discriminant. Here, we defined critical failure stress for stability evaluation, and the results were also consistent with the same empirical observations. Our models were thus verified to have a capacity for replicating actual laminated roof.

Research has found roof stability to be sensitive to the bedding plane spacing. When the bedding plane spacing is less than 25 cm, the increasing rate of the critical failure stress of the laminated roof continued to increase (Fig. 4- 7), which is similar to the quadratic relationship between the strength of a beam and beam thickness illustrated by Euler buckling equations (Esterhuizen and Bajpayee, 2012):

$$\sigma = \frac{\pi^2 E t^2}{3L^2} \qquad \text{(Eq. 4.5)}$$

where E is the elastic modulus, and t and L represent the beam thickness and beam length respectively. This consistency signified a buckling failure mechanism of the laminated roof when the laminas are thin. However, when the bedding plane spacing gets larger, the increasing rate of critical stress decreased until it reached 0 (Fig. 4- 7). The possible explanation is that the laminated roof fails in compression when bedding plane spacing increases. This scenario is quite similar to the compression curve shown in Fig. 4- 14 (Esterhuizen and Bajpayee, 2012). Generally, both the failure patterns and sensitivity analysis results were comparable to previous research.

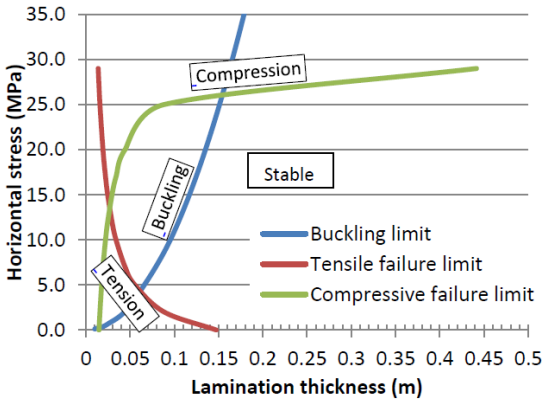

Fig. 4- 14 Potential failure modes of an elastic beam subject to external horizontal stress based on classic beam analysis (Esterhuizen and Bajpayee, 2012)

4.6 Conclusions

This section created entry models with laminated roof based on the data from laboratory tests. Based on the models, this research compared failure patterns between the laminated roof and the nonlaminated roof. Results showed that the laminated roof failed in a dome shape, while the nonlaminated roof failed with nearly vertical sides, validating the model.

This research investigated the effect of bedding plane spacing on roof stability by evaluating the critical failure stress of models. Results showed that bedding plane spacing significantly affects roof stability. The effect is sensitive to the bedding plane spacing. In addition, the laminated roof stability increases with the bedding plane strength, and the matrix that comprised the laminas determines the maximum possible strength of the laminated roof. The stress distribution of the laminated roof showed that the horizontal stress magnitude at a fixed depth increases with the bedding plane spacing.

This section investigated the effect of bedding plane strength on roof stability by changing smooth joint shear strength and tensile strength simultaneously. The roof strength increased with the increment of bedding plane strength. Bedding plane strength also affects the stress distribution in the roof. A high bedding plane strength can bring higher stress at a fixed depth. This section also investigated the effect of support pressure on the failure behavior of the shale roof using a pressure algorithm. This algorithm applied various supporting pressures to models with different bedding plane spacings. Results show that the supporting pressure increased the stability of the laminated shale model. The increase in the supporting pressure increases the strength of the laminated roof. The effect is also sensitive to bedding plane spacing.

CHAPTER 5 DISCRETE ELEMENT MODELING OF DELAMINATION IN LABORATORY-SCALE LAMINATED ROCK

5.1 Introduction

Field observations show loss of cohesion between the laminated and stack layers, which Chapter 3 concluded would result in strength reduction and failure mode change. Observations from previous research have shown cutter roof failure is usually accompanied by delamination (Hill, 1986). The current understanding of the delamination failure in these rock types is poor. Therefore, a detailed research effort to understand the delamination process of laminated rocks is necessary. In the current chapter, numerical models incorporating weak bedding planes targeted this research problem.

The parameters of a joint or weak plane model, such as shear and normal stiffness cohesion, significantly affect the behavior of the rock. Researchers have performed significant work on simulating rock with joints or weak plane, providing various insights on how to assign parameters to the model (Chiu et al., 2013; Lambert and Coll, 2014; Oh et al., 2017; Wai Loong et al., 2013; Yang et al., 1998). The research approach mentioned in the literature review used non-persistent joints to simulate bedding planes that are different from actual laminated shale (Swift and Reddish, 2005). The joint models have predefined stiffness that restricts delamination and therefore cannot explain the intrinsic process of delamination of a laminated rock under various stress conditions.

When comparing the modeling methods and the joint models, PFC is uniquely able to simulate the crack development with its smooth jointed model, as demonstrated in Chapter 4. The inherent constitutive models in PFC are capable of modeling both the frictional and cohesive planes. The present chapter particularly focused on the frictional planes. The calibrated models investigated the delamination process under different boundary conditions at a laboratory scale. This study will provide further understanding of the process of delamination.

5.2 Methodology

This research used the parallel bond model to model the laminas and the smooth-joint model to represent the plane of weakness. This research calibrated its microparameters based on the laboratory testing data from Yang's experiments (Yang et al., 1998). Yang fabricated brittle rock

with a mixture of plaster, sand, and water in the proportions of 1:0.25:0.92. This study also created a synthetic frictional weak plane using a controllable double-blade guillotine with 60°-wedge blades. Direct shear test performed on this synthetic weak plane provided mechanical parameters for the plane.

This research obtained the parameters of bedding by calibrating the parallel bond model with the laboratory data for intact rock. To obtain the parameters of the weak plane, this research calibrated the smooth-joint model with the laboratory data from direct shear tests by simulating a direct shear model in the PFC. Then, the bedding and weak plane parameters are combined together to create the laminated rock mass model. Simulated triaxial compression tests investigated the effect of joint angle on the mechanical behavior of a jointed rock. This research validated the results by comparison with the rock mass magnitude. The following flow chart shows procedure to simulate the laminated rock model.

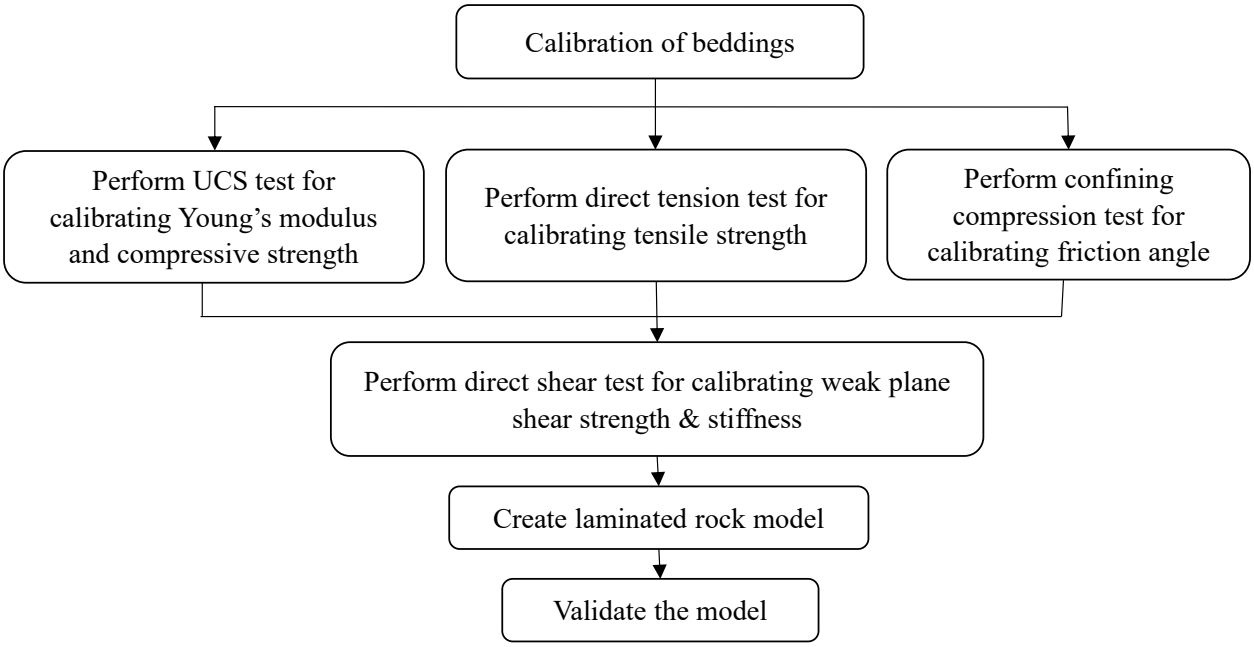

Fig. 5- 1 Procedure to simulate laminated rock

5.3 Calibration

5.3.1 Calibration of laminas

Based on the laboratory tests, the uniaxial compressive strength is 7.63 MPa, the direct tensile strength of the rock is 1.05 MPa, the Young's modulus is 4.55 GPa, and the internal friction angle is tested as 31°.

Following the calibrating procedures recommended by Itasca (Potyondy and Cundall, 2004), the microparameters of matrix, including Young's modulus, direct tensile strength, and uniaxial compressive strength, are calibrated as shown in Fig. 5- 2 and Fig. 5- 3.

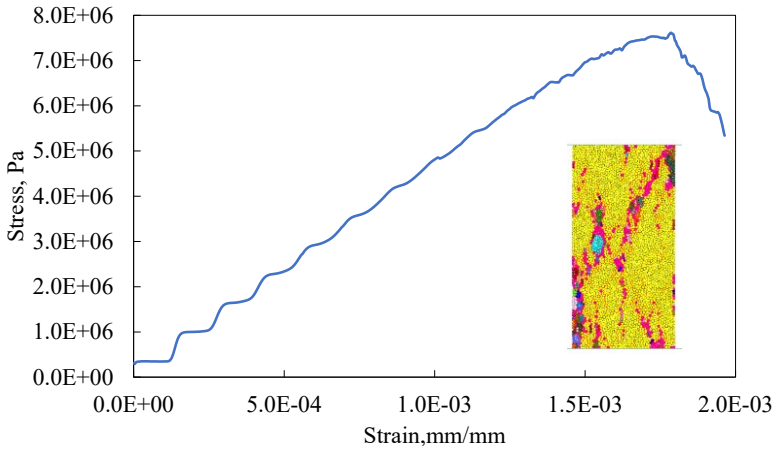

Fig. 5- 2 Calibration of Young's modulus and uniaxial compressive strength

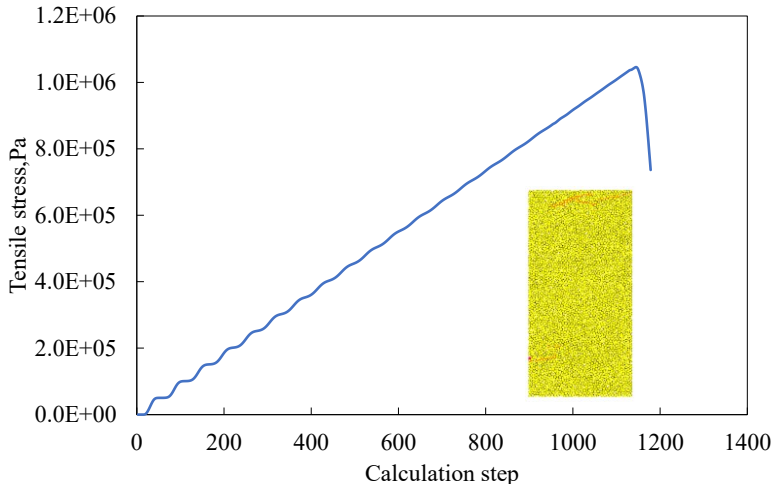

Fig. 5- 3 Calibration of direct tensile strength

Finally, we simulated the confined compression strength tests with a servo-control mechanism using confining pressures of 2.5, 5.0, and 7.5MPa. Table 5- 1 shows the test results of both the direct tensile and unconfined compressive tests. Fig. 5- 4 shows the Mohr envelope of the specimen matrix.

Table 5- 1 Compressive test results under different confining stress

Direct tensile strength, MPa		Unconfined stress		Confining stress=2.5MPa		Confining stress=5.0MPa		Confining stress=5.0MPa	
σ_3	σ_1	σ_3	σ_1	σ_3	σ_1	σ_3	σ_1	σ_3	σ_1
-1.05	0	0	7.6	2.5	17.5	5.0	25.1	7.5	33.5

Note: σ_3-the applied minimum principal stress σ_1-the applied maximum principal stress

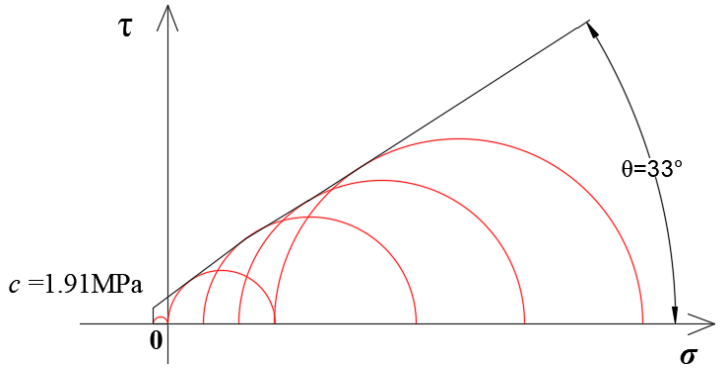

Fig. 5- 4 The Mohr envelope of the parallel bonded model

Table 5- 2 shows all the calibrated results as compared to laboratory results. The macro parameters of the bonded particle model are in good agreement with the tested specimens in the laboratory. Table 5- 3 lists all calibrated micro parameters.

Table 5- 2 Comparison with the numerical and laboratory results

	Unconfined compressive strength, MPa	Direct tensile strength, MPa	Young's modulus, GPa	Angle of friction, degrees
Laboratory results	7.63	1.05	4.55	31
Numerical results	7.62	1.05	4.50	33

Table 5- 3 Micro parameters utilized for the parallel bond particle model

Parameters	Values
Particle radius, mm	0.5- 0.75
Material density, kg/m^3	2,500
Bond gap	0.5e-4
emod, GPa	2.219
kratio	1.0
pb_ten, MPa	1.538
pb_coh, MPa	4.5
pb_fa, degrees	31
Ball-ball friction	0.4

Note: emod- parallel bond effective modulus; kratio- parallel bond normal-to-shear stiffness ratio;
pb_ten- parallel bond tensile strength; pb_coh- parallel bond cohesion;
pb_fa- parallel bond friction angle

5.3.2 Calibration of the weak planes

As mentioned in earlier sections, mechanical parameters play a dominant role in determining the behavior of the entire specimen. It is therefore imperative to calibrate the weak planes in the numerical model. The present research used a direct shear test to obtain the mechanical parameters and calibrate the weak planes in the models. The data from the direct shear test was used on a

frictional weak plane with zero cohesion value of the weak plane. Fig. 5- 5 shows the direct shear conducted under normal stress of 0.63 MPa in the lab (Yang et al., 1998). The shear stiffness of the weak plane is 0.48GPa, and the shear strength is 0.96 MPa.

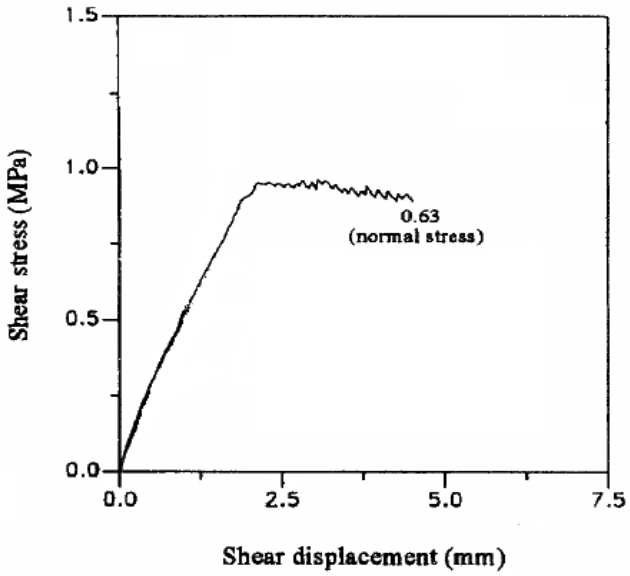

Fig. 5- 5 Direct shear test in lab (Yang et al., 1998)

We developed a direct shear model composed of the parallel bond particle as matrix and smooth joint fracture as a frictional weak plane in PFC2D, as shown in Fig. 5- 6a. The red line represents the location of the smooth joint plane. The servo-control mechanism applied normal stress to the top of the specimen. The model simulated the shear process by moving the upper platen horizontally over a fixed lower platen.

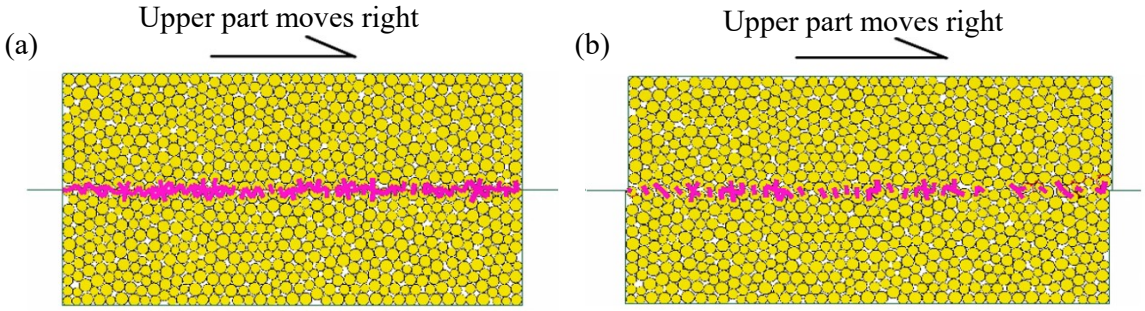

Fig. 5- 6 Illustration of the (a) original and (b) sheared direct shear model

The numerical model monitored the upper platen displacement and the shear stress along the weak plane. The model calibrated shear stiffness and shear strength through a trial and error approach. The calibrated results with a shear stiffness of 0.45 MPa and shear strength of 0.98MPa show a good correlation with the laboratory data as observed in Fig. 5- 7. This showed that the simulated

weak plane matched the actual behavior of the weak plane in an intact rock. Table 5- 4 lists the parameters used for the smooth-joint model.

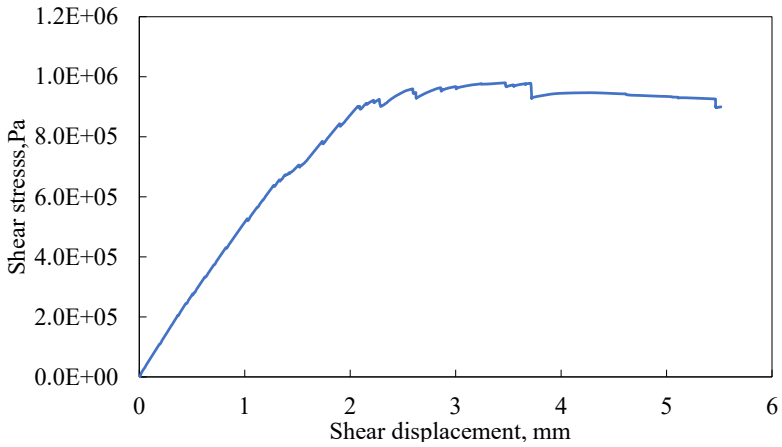

Fig. 5- 7 Simulated direct shear test

Table 5- 4 The calibrated micro parameters for smooth-joint model

Parameters	sj_kn, GPa	sj_ks, GPa	sj_fric	sj_coh	sj_ten	sj_large
Values	200	9.9	2.3	0	0	1

Note: sj_kn-smooth-joint normal stiffness; sj_ks- smooth-joint shear stiffness;
sj_fric- smooth-joint friction coefficient; sj_coh- smooth-joint cohesion;
sj_ten- smooth-joint tensile strength; sj_large- smooth-joint bond type

5.3.3 Validation of combined micro parameters

We conducted a series of confined compressive tests on an inclined single joint specimen to validate the combination of parallel-bond model and smooth-joint model as shown in Fig. 5- 8. The confining stress was set at 1.0 MPa, and we compared the results to theoretical conclusions (Swift and Reddish, 2005).

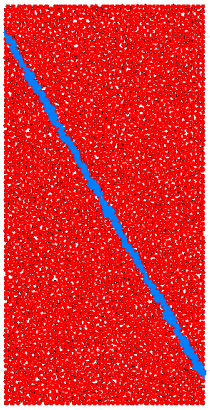
Fig. 5- 8 Rock specimen with a 60° oriented joint

Fig. 5- 9 plots the compressive strength of the specimens with different orientations. The curve is in good agreement with theoretical results, validating the feasibility of the combination of

parameters for the parallel bond model and smooth-joint model (Jaeger, 1959). Fig. 5- 10 shows the stress-strain curves for these specimens. This figure shows that the specimens with 30-70° orientations have low overall Young's modulus and low strength. This is due to the sliding along the plane of weakness.

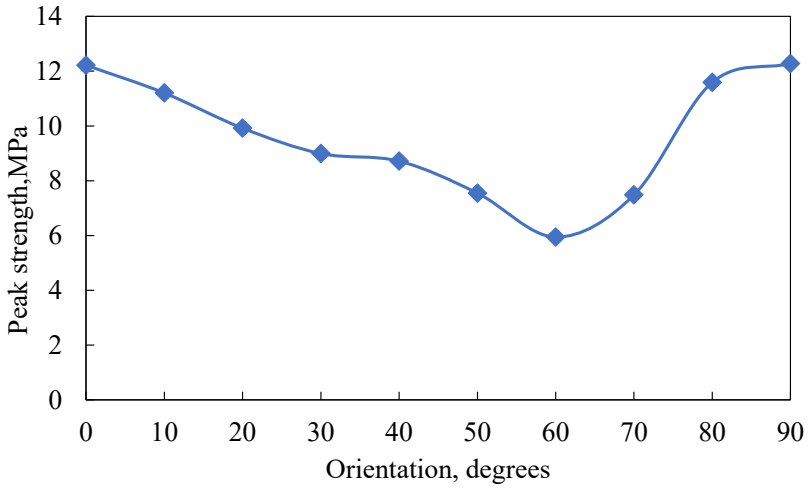

Fig. 5- 9 Compressive strength with various inclined weak planes

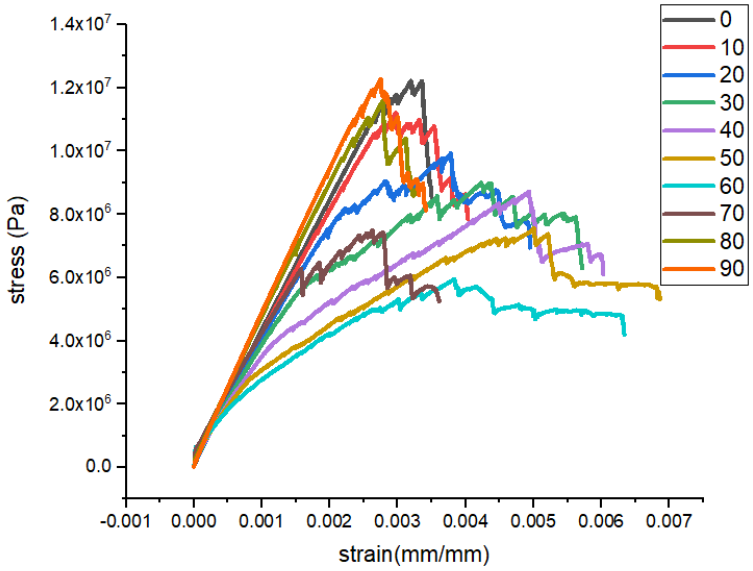

Fig. 5- 10 Stress-strain curves for specimens with orientation of bedding planes

5.4 Delamination simulation

With the validated micro parameters obtained in earlier sections for both the bedding and the weak plane, this research built laboratory-scale laminated rock specimens in PFC2D with dimensions of 150mm in length and 80mm in height. The program simulated specimens with uniaxial, triaxial boundary conditions. This was then followed by a simulation of an unsupported roof under compression test to observe the failure process of the laminated specimen under different stress

conditions. Fig. 5- 11 shows the schematic diagrams of these models. Focusing on the development of delamination, the following sections discuss the tests on these models in detail.

The simulation consists of the following different conditions to which the model is tested:

(1) Uniaxial compressive test subjected to incremental horizontal stress.

(2) Uniaxial compressive test subjected to various constant horizontal stress.

(3) Confined compressive test subjected to incremental horizontal stress.

(4) Compressive test on unsupported roof model subjected to incremental horizontal stress.

Conditions (1) to (3) focused on the unconfined and confined effect of the delamination under various horizontal stresses. Condition (4) simulated the stress state, which is commonly observed in underground-unsupported entries. Condition (1) also investigated the effect of bedding plane spacing on delamination.

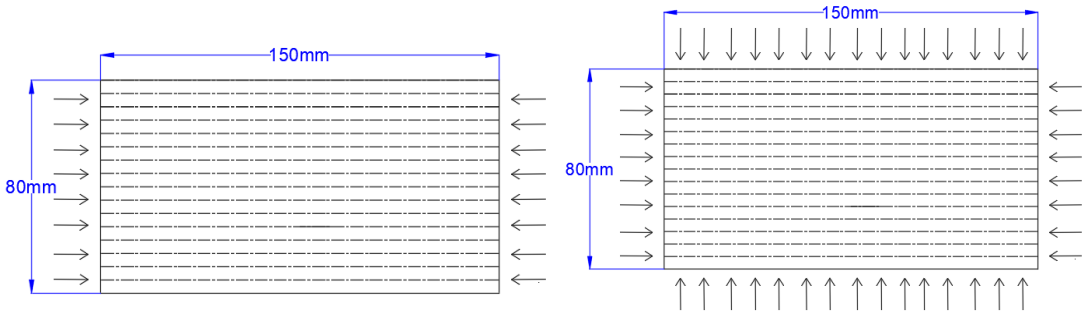

(a) Uniaxial compressive test model (b) Confined compressive test model

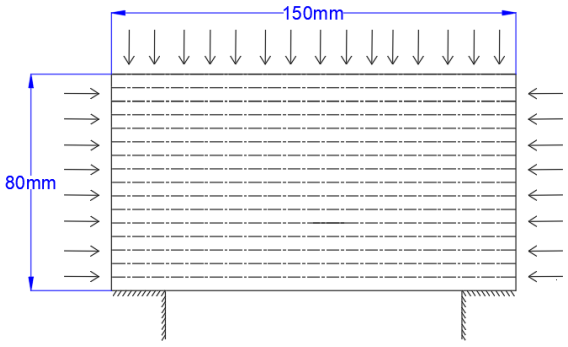

(c) Unsupported roof test model

Fig. 5- 11 Simulation sequence

5.4.1 Uniaxial compressive test subjected to incremental horizontal stress

Fig. 5- 12 shows the smooth jointed laminated model. The red lines represent the parallel joints and the yellow particles represent the laminas. The uniaxial stress in the model represents the

horizontal stress. The model applied this stress by moving boundaries at a constant velocity, which can cause incremental horizontal stress. The moving velocity of the platens was 0.01m/s. This study recorded observations of the model behavior throughout the test. Fig. 5- 13 shows the strain-stress curves for all the models, including the intact rock and laminated specimens with various bedding plane spacings.

This study then conducted an analysis on laminated rock specimens with a bedding plane spacing of 4, 5, 6, 7, and 8mm.

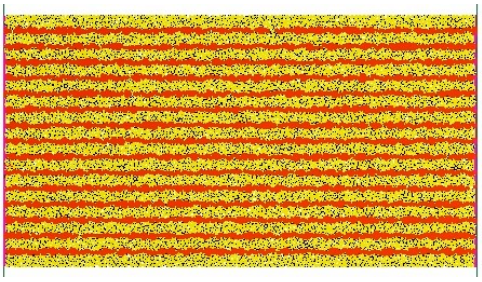

Fig. 5- 12 Laminated rock model

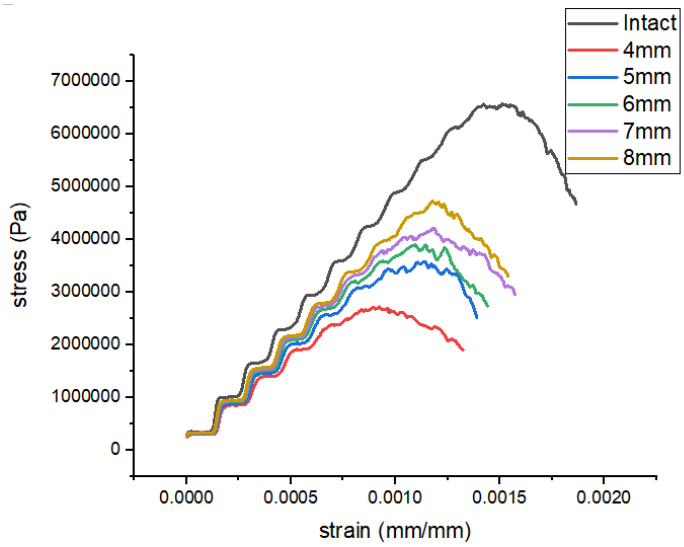

Fig. 5- 13 Stress-strain curves for specimens with different bedding plane spacings

Fig. 5- 13 shows that the laminated rock strength increased with the bedding plane spacing. Therefore, thick lamination will sustain high horizontal stress. Similarly, the stiffness of the specimen will also increase with an increase in the bedding plane spacing. In addition, the peak stress occurs at different strain magnitudes for these curves, as shown in Fig. 5- 13. For example, the 8mm-bedding specimen reaches its peak stress when the strain is 0.0011, while the 4mm-bedding specimen reaches its peak at the strain of 0.0008, indicating that the thinner bedding will bring about a smaller strain value when reaching peak strength. From the model results, one can

conclude that the thickness of the bedding in laminated rock significantly affects the macro behavior, e.g. along- bedding stiffness, along- bedding strength, and the maximum strain it can sustain before failure.

Fig. 5- 14 shows the sequence of the delamination process captured from the numerical simulation. As shown by the legend, the black lines represent the compressive force chain in the specimen, while the red lines represent the tensile force chain, which is not noticeable during the test. The boldness of these lines represents the relative magnitude of the force. The red cracks represent the fractures, which indicate unbonded particles. The colored particles represent the fragments in the specimen, and the same color indicates a piece of the fragments that consist of a clump of bonded particles. Different colors of fragments indicate that the fragments are separate due to the development of fractures. The colored arrows represent the particle moving velocity under the horizontal stress, and the size of the arrows represents the magnitude of the velocity.

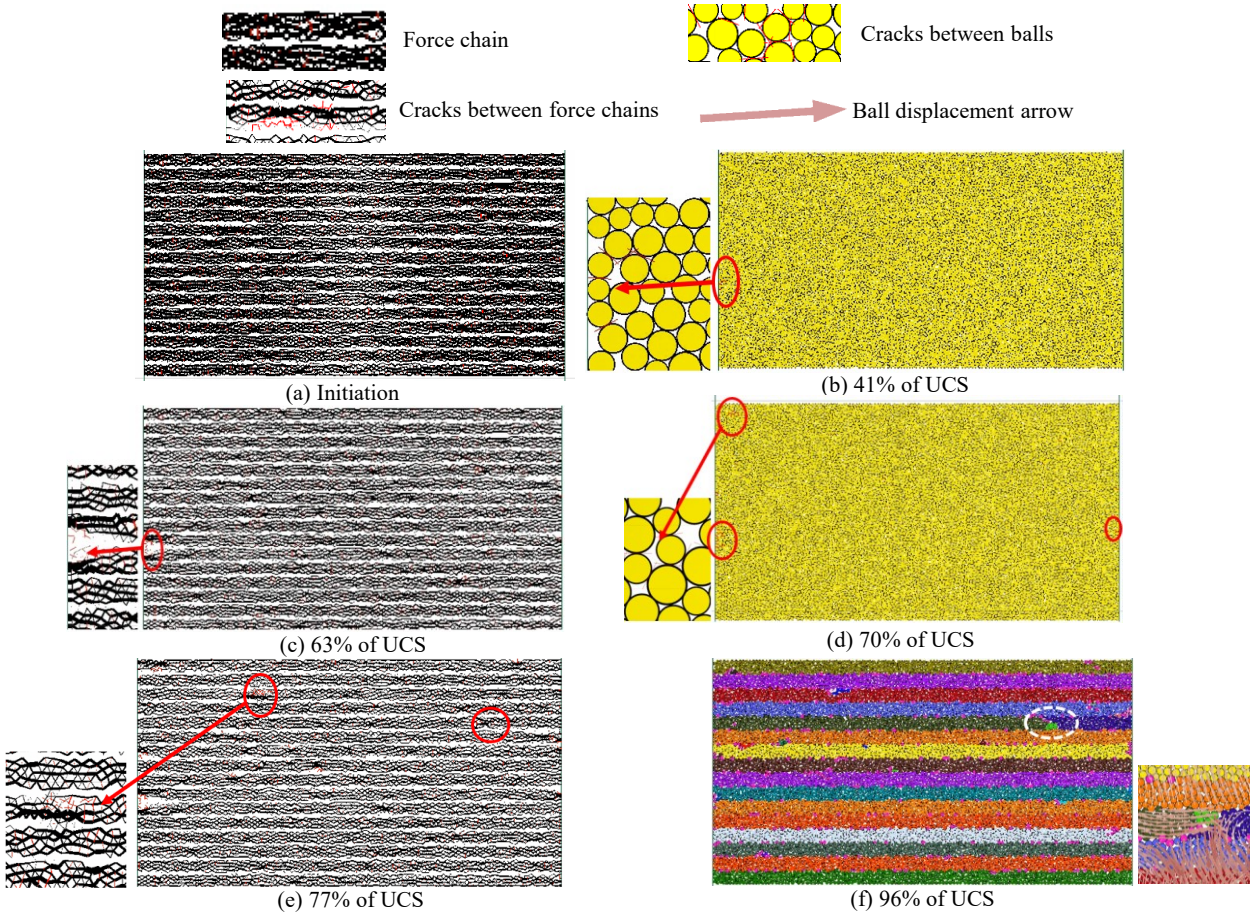

Fig. 5- 14 Development of delamination (continued on next page)

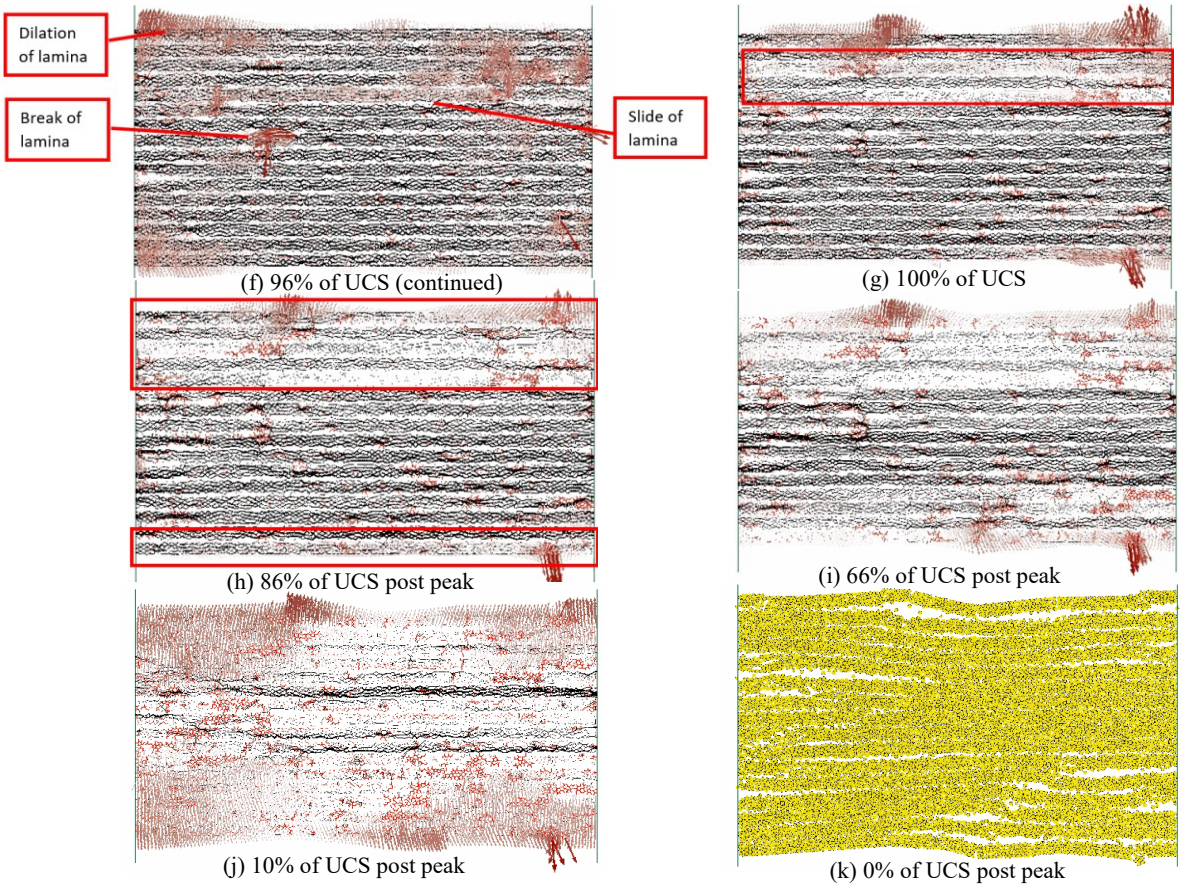

Fig. 5- 14 Development of the delamination

In Fig. 5- 14a, at the initiation of the test, the force chain inside the specimen includes various separate force chains that exist inside the laminas. This is because the laminas are mechanically disconnected from each other, as there is no cohesion between the laminas. The force chains do not connect at all, indicating that there is no vertical force between the laminas. As such, one can conclude that the laminas are acting independently under horizontal stress in an unconfined condition.

At 41% of its uniaxial compressive strength, the specimen develops fractures at its left end. In addition, the initiation location is inside the specimen instead of on the edge of the specimen. Fig. 5- 14c shows the localization of fractures at the initiation point and the progressive change in the force chain shape with every increment in the compressive stress, indicating the transfer of force. Subsequently, cracks occur at different places on the edge of the specimen (Fig. 5- 14d and Fig. 5- 14e).

The delamination does not occur until the compressive stress exceeds 96% of its compressive strength (Fig. 5- 14f). In Fig. 5- 14f, failure occurs in the fifth bedding from the top. This bedding is represented by three colors: the left section in grey, the middle section in green, and the right section in blue, demonstrating bedding failure. The particle velocity further validates the failure of this bedding. As seen in the velocity distribution picture in Fig. 5- 14f, the left grey section moves towards the right, while the right blue section moved to the lower left. In addition, the upper bedding moved upward vertically and the lower bedding moved downward vertically. This showed that the laminas moved apart, indicating the occurrence of delamination. At the same time, the fifth bedding slid relative to its upper and lower laminas, which is another indicator of the delamination. In Fig. 5- 14f, the entire left section of the fifth bedding moved to a new position. In addition, particles also moved in opposite directions in various localized sections, indicating the breakage of the bedding. Surprisingly, specimen failure did not occur when the laminas moved in the outward direction.

When the compressive stress reaches exactly the compressive strength of the specimen, force chain boldness of the third and fifth bedding from the top decreased to zero, which indicated a loss in strength, as shown in Fig. 5- 14g. However, at the same time, the bedding between them (third bedding from the top) still maintained the stress shown by the boldness of the force chain. This indicated that the failure of the bedding is not continuous, and therefore the failed bedding and non-failed bedding may occur alternatively at a specific point in time.

After the compressive strength test, the laminated specimen did not completely disintegrate due to the residual strength. When it reached 86% of the compressive strength in the post-peak stage, the upper five laminas faded, indicating a loss in strength as shown in Fig. 5- 14h. Similarly, this behavior occurs in the bottom outer bedding. Since the applied stress continues to work, more laminas adjacent to failed ones lose their strength, which results in expanding delamination scope and seriousness. Finally, the specimen dilates even after the complete disintegration of the specimen, as shown in Fig. 5- 14i, j, and k.

5.4.2 Uniaxial compressive test subjected to various constant horizontal stress

In underground roadways, the horizontal stress usually remains relatively constant after excavation of the roadways. Therefore, it is important to investigate the process of delamination of the

laminated specimen under constant horizontal stress. This section investigates this phenomenon by applying varying constant horizontal stress to the 5mm-bedding specimens.

When the horizontal stress is at 41% of the compressive strength, the contact force chains maintain their original shape and magnitude. Only limited fractures occur within the specimen, as shown in Fig. 5- 15. This indicates that the delamination will not occur under this magnitude of compressive stress.

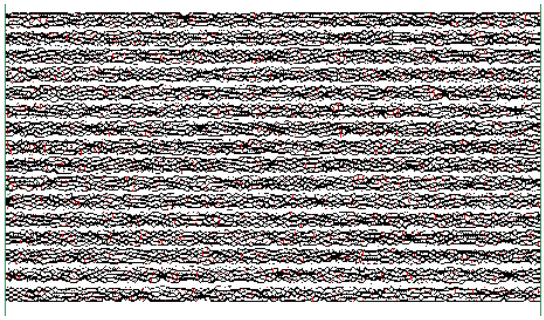

Fig. 5- 15 Horizontal stress at 41% of compressive strength

However, when the horizontal stress increased to 42% of the compressive strength, delamination occurred in the specimen after 30,000 time steps as the adjacent laminas inside moved in the opposite directions, as shown in Fig. 5- 16a. Therefore, the complete specimen delaminated with its upper half moving upward and the lower half moving downward. With every increment in the calculation step, the delamination becomes more pronounced. As shown in Fig. 5- 16b, one bedding separated completely from both its upper and lower halves with a reduction in the strength, partially due to the opposite moving directions of these two parts. However, in comparison with Fig. 5- 14f, the delamination only initiated from one bedding, while this occurred at multiple places in Fig. 5- 14f. With the calculation step at 1,600,000, the whole specimen loses its strength. This is similar to roof fall that occurs in mines due to loss of strength.

In conclusion, delamination may occur under constant horizontal stress, which is much lower than its compressive strength. In addition, the laminated specimen may completely lose its strength under constant stress.

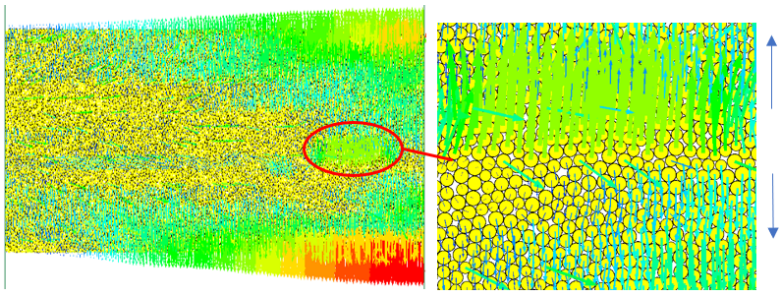

(a) Step 30,000

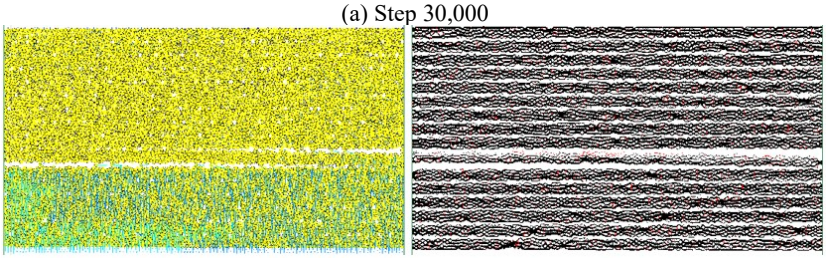

(b) Step 300,000

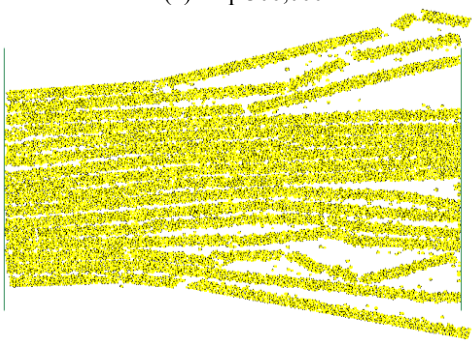

(c) Step 1,600,000

Fig. 5- 16 Horizontal stress=42% of compressive strength

5.4.3 Confined compressive test subjected to incremental horizontal stress

The roof is reinforced with a support system, such as roof bolts, that provides confining pressure to the laminated roof. The present section observed both the failure process and mode under a confined compressive state. This section of research sets the confined stress at 1.0 MPa through the servo-control mechanism in PFC2D. In order to make a comparison with the tests under uniaxial compressive state in section 5.4.1, all geometrical and mechanical parameters, including dimension, bedding plane spacing, bedding and weak plane micro parameters, are set to be the same as the model in section 5.4.1. Fig. 5- 17 shows the full stress-strain curve of this test in which the confined compressive strength is 7.9 MPa. This figure shows that the monotonic portion of the stress-strain curve is nearly a straight line, which is similar to a uniaxial compression test. Instead of a sharp drop in stress after failure, one can observe residual strength under the confining stress.

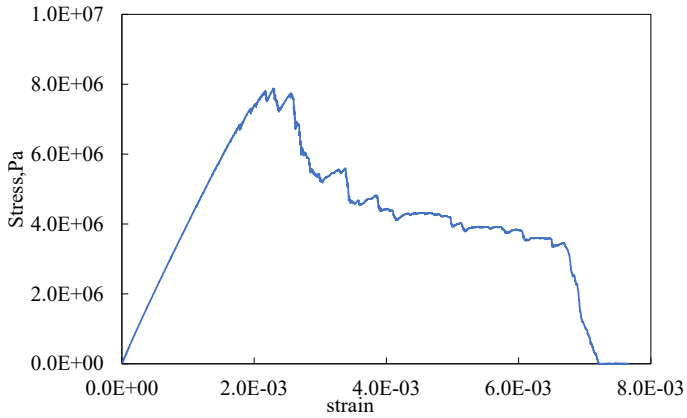

Fig. 5- 17 Full stress-strain curve of confined compressive test

Fig. 5- 18 depicts the force chain, particle moving velocity, bedding fragment, and fracture developing process. The signs and their physical meanings are the same as described in earlier sections. The figure showed that the force chains connect to each other, in comparison with those from the uniaxial test in Fig. 5- 14a. This showed that the laminas mechanically connect with each other due to the confining pressure. Therefore, the laminated specimen acts as if complete instead of carrying the load independently as in the uniaxial test.

The fractures initiate at the edge of the specimen when the stress reached 46% of the strength, as shown in Fig. 5- 18b, which is marginally higher than the uniaxial test at 41%. As the horizontal stress continued to increase, these fractures continued to develop and progressively change the shape of the force chain at the left end of the specimen in Fig. 5- 18c, indicating the change in the force distribution.

When the horizontal strength reached 78% of the confined compressive strength, the bedding fractured inside the specimen. As shown in Fig. 5- 18d, the particles in the same bedding moved towards the opposite directions and interacted with the fragments. The same case occurred in several more laminas in the specimen when the compressive stress reached 96% of the confined compressive strength, as shown in red circles in Fig. 5- 18e. Some small sections also separated from these laminas, as highlighted by red circles, that caused the shape change of their force chains. However, these laminas still did not completely fail, as their force chains are still capable of carrying load. The bedding disintegrated into small sections after exceeding the peak value (Fig. 5- 18f). The test proceeded into post-peak stage in which the laminas continued to fail and disintegrate into small pieces until the specimen completely disintegrated (Fig. 5- 18g).

The delamination failure mode that occurred in the uniaxial compressive test does not occur during any stage of the confined compressive test. Therefore, this study concluded that by applying supporting systems to the laminated roof, it is possible to restrain delamination, e.g. roof bolting or secondary support can apply confining stress to the free face of the roof.

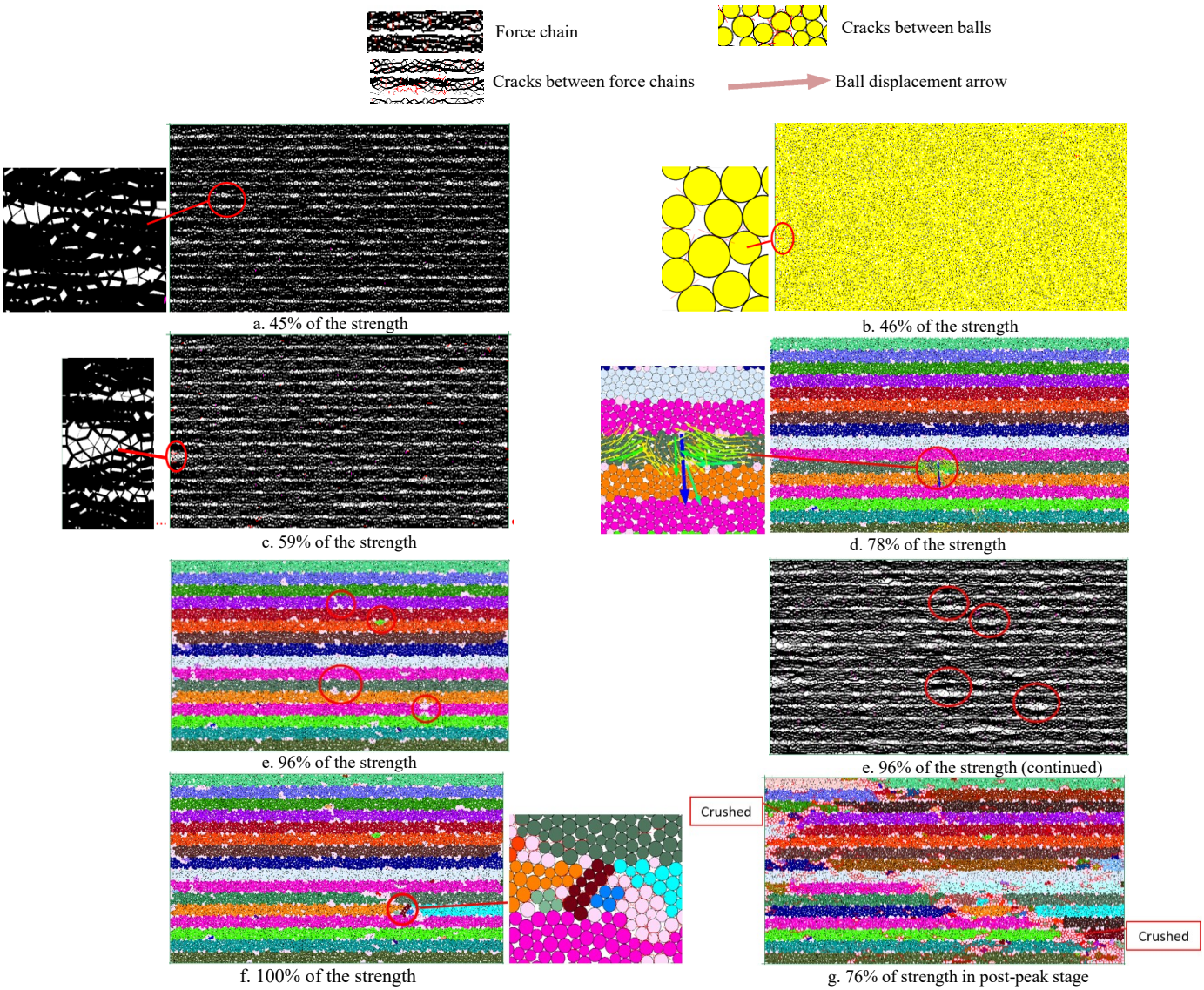

Fig. 5- 18 Failure propagation in the confined compressive stress test

5.4.4 Compressive test on unsupported roof model subjected to incremental horizontal stress

This section simulated an unsupported roof model at a laboratory scale. Fig. 5- 11c shows the schematic diagram of the model. The rigid boundaries in the lower corners are the supporters provided by ribs of the roadway. Fig. 5- 19 shows the unsupported roof model established in PFC2D in order to investigate the failure propagation in such a stress state. All the micro-

parameters and geometric dimensions are the same as the models in earlier sections, except for the boundary conditions. The model initiated with a hydrostatic stress state set at 1.0 MPa. The test applied horizontal stress until a complete loss in the strength of the roof occurred.

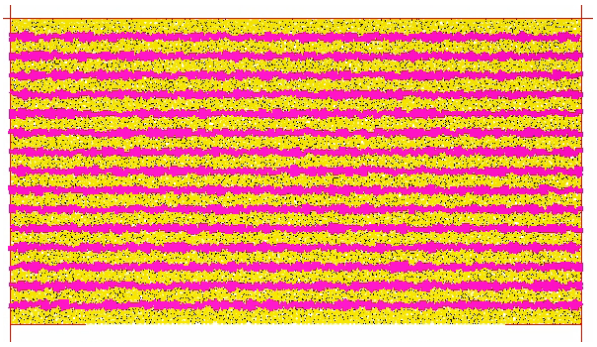

Fig. 5- 19 Unsupported roof model

Fig. 5- 20 shows the stress-strain curve obtained after the test completed. The strength of the unsupported roof is 3.5MPa, which matches the uniaxial compressive strength in Fig. 5- 13 and is much lower than the confined compressive strength in Fig. 5- 17.

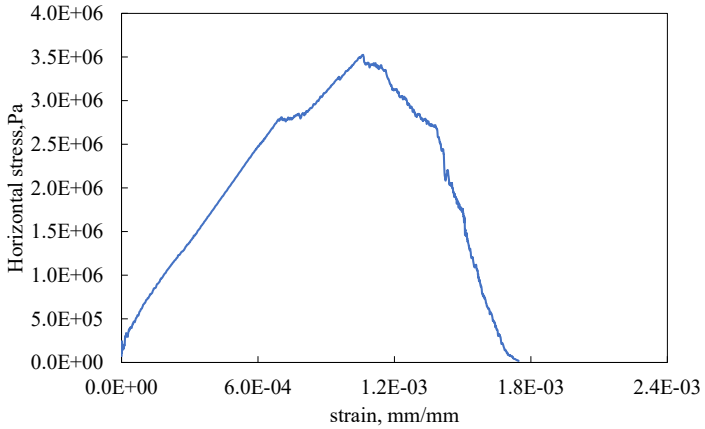

Fig. 5- 20 Full stress-strain curve of unsupported roof model

Fig. 5- 21 depicts the force chain, particle moving velocity, bedding fragment, and fracture developing process. The signs and their physical meanings are the same as in earlier sections.

The cracks initiate from the two bottom corners of the specimen, which represent the intersection of the roof and ribs as shown in Fig. 5- 21. With the increase in the horizontal stress, the bottom bedding moves downward to its left side adjacent to the intersection. This causes delamination at this location as shown in Fig. 5- 21b, which is in good agreement with field observations of cutter roof failure. Next, the right side of this bottom bedding starts to delaminate as well. Fig. 5- 21c

shows that the delamination of this bedding gradually caused its failure, as demonstrated by the faded force chain of the bottom bedding.

The next failed bedding is not the one adjacent to the bottom bedding. Instead, the inner bedding showed delamination. As shown in Fig. 5- 21d, the particles moved in opposite directions in the fifth bedding from the bottom of the specimen when the horizontal stress reached 80% of its strength, indicating the initiation of bedding failure. Fig. 5- 21d further verified this failure by showing its faded force chain. Immediately after the fifth bedding failed, the sixth bedding failure occurred, shown by the faded force chain in Fig. 5- 21e. This created two separate failed zones in this specimen, i.e. the outer failed zone and inner failed zone. These zones are separated by several intact laminas between them.

The second bedding from the bottom does not fail until the horizontal stress reaches its peak value, i.e. the strength of this specimen, as shown in Fig. 5- 21f. The particles of this bedding moved horizontally at a relatively high velocity. This causes the bedding force chain to weaken, as shown in the force chain map in Fig. 5- 21f. Afterward, the test moved into the post-peak stage where the intact laminas lose their strength one by one until the separate failed zones connect with each other, as shown in Fig. 5- 21g. Next, the failed zones develop upward until the whole specimen loses its strength, as shown in Fig. 5- 21h and i. The failed roof mass continued to fail and formed an opening as observed in the field.

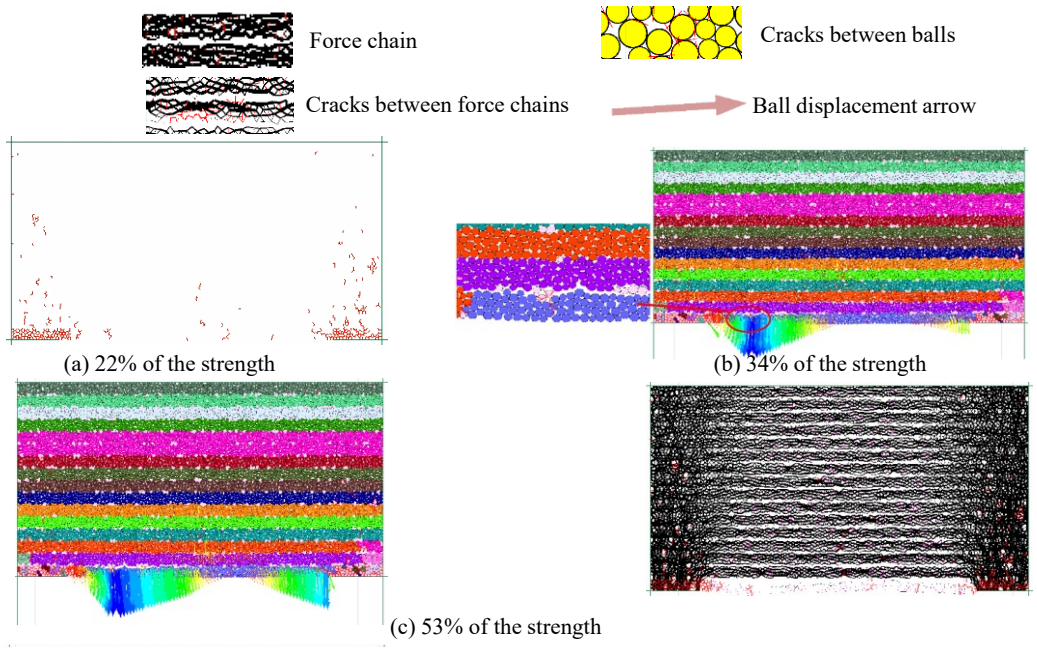

Fig. 5- 21 Cutter roof failure propagation of unsupported roof model (to be continued)

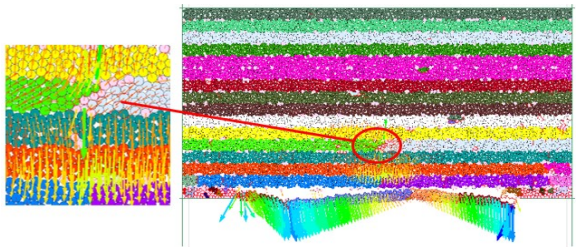

(d) 80% of the strength

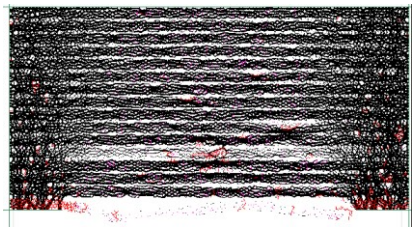

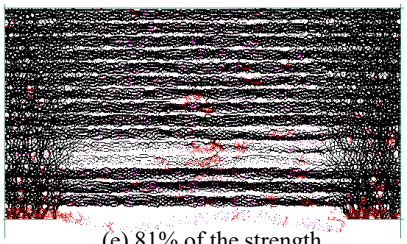

(e) 81% of the strength

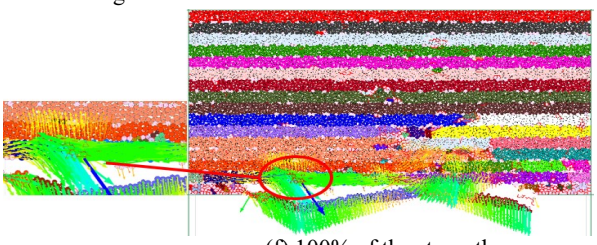

(f) 100% of the strength

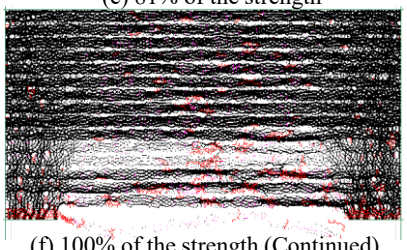

(f) 100% of the strength (Continued)

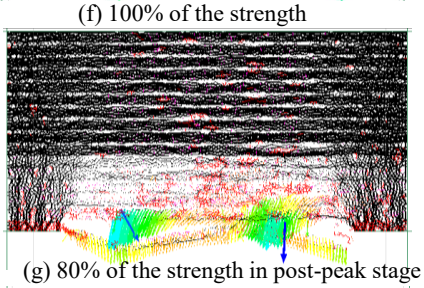

(g) 80% of the strength in post-peak stage

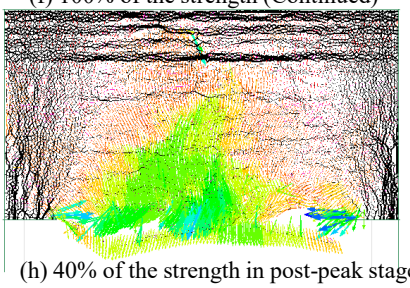

(h) 40% of the strength in post-peak stage

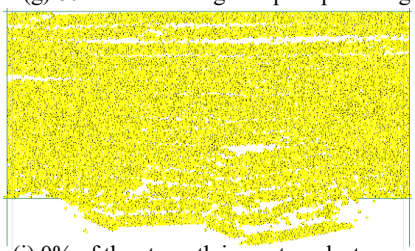

(i) 0% of the strength in post-peak stage

Fig. 5- 21 Cutter roof failure propagation of unsupported roof model (continued)

5.5 Conclusions

This chapter presented a numerical investigation of the delamination process of a laboratory-scale laminated specimen with frictional bedding planes. This study created laminated rock with a parallel bond model and smooth-joint model in PFC2D and validated the calibrated models with the confined compressive tests on specimens with varying plane orientations. The validated laminated model implemented the compressive tests under various stress conditions and investigated the crack development and delamination propagation during these tests.

Uniaxial compressive tests with various bedding plane spacings showed that the thickness of the bedding significantly affects the macro parameter of the laminated specimen, including along-

bedding stiffness, along-bedding strength, and the maximum strain it can sustain before failure. Increased thickness of the bedding caused an increase in the macro parameters.

The delamination propagation analysis of uniaxial compressive tests showed that the delamination of an unconfined specimen begins on the inside laminas instead of the outer ones. Delamination does not occur until the compressive stress matched the UCS when applying incremental stress to the specimen. However, delamination occurred under constant horizontal stress, which was much lower than its compressive strength. The modeling results confirmed that applying confining stress prevented delamination. The compressive test on an unsupported roof model showed that cutter roof propagation and delamination initiated at the intersections of the roof and ribs. Before roof fall, separate failed zones formed in this specimen, i.e. outer failed zone and inner failed zone. These zones are separated by several intact laminas between them. The separate failed zones connect with each other as the intact laminas weaken and finally create a massive failure. This research showed the mechanism involved in roof delamination. The effect of interface parameters such as strength and stiffness of the weak planes will require further investigation.

CHAPTER 6 INVESTIGATION OF LAMINATED ROOF FAILURE COUPLING DEM AND FDM

6.1 Introduction

As discussed in Chapter 3, the effect of bedding plane strength is sensitive to stress conditions. One can, therefore, expect that the stress condition variation around a longwall panel would influence the effect of lamination properties on the roof stability.

Normally an entry in a longwall coal mine serves two panels. Therefore, the surrounding rock of an entry experiences three stages through its life span: development, one-panel extraction, and two-panel extraction. The development stage corresponds to the stress concentration caused by the excavation of the entry. The one-panel extraction stage corresponds to the first longwall panel extraction that causes side abutment pressure acting on the entry's surrounding rock. The extraction of the panel on the other side of the entry brings new side abutment pressure that typically causes higher stress concentration. Researchers have identified that the entry roof shows a different ground response to these stages according to field observation (Wang and Peng, 1996). Particularly, studies have not investigated how these stress conditions change the effect of laminated properties on the laminated roof, according to the previous literature review. Investigating the sensitivity of the effect of lamination properties to stress conditions is impossible in the field since it is impossible to observe lamination properties in the field in the first place. This is also the reason why we fabricated SLR in Chapter 3. On the other hand, replicating the three stages of stress conditions in the laboratory is out of the financial scope of this work.

This chapter adopts numerical simulation to approach this topic. Compared to the finite difference method (FDM), research has recognized the discrete element method (DEM) for its excellent performance in simulating large strain problems and fracturing processes in rock mass. However, the discrete element method has its limitations. Simulating a large-scale problem requires a large number of particles, which consumes significant computational resources. Coupling DEM/FDM can significantly reduce the required computational resources without sacrificing the robust performance of DEM in capturing the cracking process (Breugnot et al., 2016; Indraratna et al., 2015), making it possible to study an entry-scale model or even a panel-scale model.

This chapter first validated the coupling method by coupling a uniaxial compressive test. Then, it creates a 3D numerical model coupled with the FDM and DEM to simulate the laminated roof failure in an eastern coal mine in the US. The FDM-DEM coupled model represents the laminated roof of the entry by an assembly of bonded particles using PFC3D. The model simulates the laminated roof by adding parallel bedding planes incorporating a certain stiffness and strength in the model. Continuum zones represent the ribs, floor, and far-field surrounding rock using FLAC3D. After verifying the coupled model with filed measurement results, this study implemented parametric studies of bedding plane strength. This process varied the strength of the bedding planes and cohesion-to-tensile ratio of the bedding planes to observe their effect on laminated roof response subjected to panel extraction-induced loadings.

6.2 Coupling methods

Historically, there were two coupling strategies to take advantage of both discrete element and continuum methods: the edge-edge method and bridging domain method, which is called wall-zone logic and ball-zone logic in PFC/FLAC coupling respectively. In the edge-to-edge method, the FDM and DEM interact through an interface slaved to the FDM zones, while the bridging-domain method realizes the data exchange by an overlapping area.

The edge-edge method coupling method ensures accuracy by the interaction that occurs in the interface between DEM particles in PFC3D and FDM zones in FLAC3D (Breugnot et al., 2016), as shown in Fig. 6- 1a. The interface serves as a boundary condition for both the DEM domain and the FDM domain. The DEM particle acts as a stress/force boundary of the FDM zones. Both contact forces and moments between DEM particles are transferred to the FDM elements through the contact points within the interface. Meanwhile, the method calculates the FDM grid point velocities within the interface every time step and transfers them to the DEM particles. Itasca software realizes this vital data exchange process by using wall-zone logic. The critical time step needs to be identical in both the DEM domain and FDM domain to ensure data exchange.

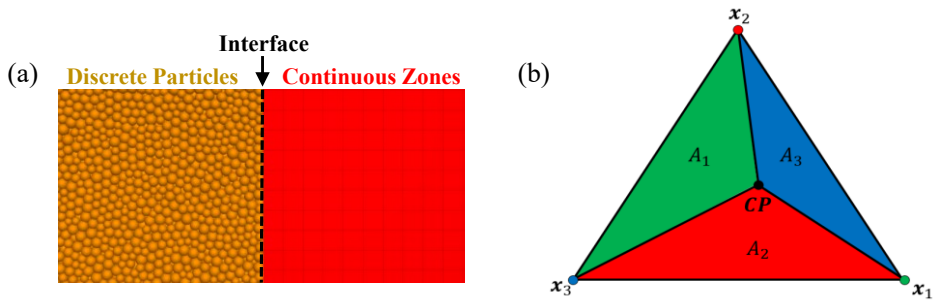

Fig. 6- 1 Depiction of coupling approach (a) and interpolation scheme (Itasca Consulting Group, 2019) (b) of wall-zone logic in PFC/FLAC

Wall-zone logic captures the grid point coordinates and transfers them into DEM, wherein it creates wall facets to wrap these FDM zones. The wall facets are responsible for interacting with particle force/moments and grid point velocities. Every time step, the grid point coordinates renew; the wall facets renew accordingly, hence they can update the velocity boundary applied to the discrete particles. Vice versa, the process updates the discrete force and moments passed to the grid points by the wall facets simultaneously. This scheme breaks the quadrilateral zone faces into two triangles (Itasca Consulting Group, 2019) and calculates forces for the three gridpoints corresponding with the wall facet. When a particle is in contact with a triangular wall facet created to wrap a zone face, we denote the position of the closest point on the wall facet to the contact point as a vector $\overrightarrow{\boldsymbol{CP}}$, as shown in Fig. 6- 1b. The wall-zone logic adopts a barycentric interpolation/extrapolation to extrapolating values of this point (forces and moments) to the vertices of the triangle, which coincides with the zone grid points. $\overrightarrow{\boldsymbol{X_i}}$, $\boldsymbol{i}$=1,2,3, representing the locations of the three triangular vertexes. Hence, one can determine weighting factors for each vertex by taking the triangle area opposite a vertex divided by the total area of the triangle, i.e. $w_i=A_i/A$. Thus, each value of the $\overrightarrow{\boldsymbol{CP}}$ can transfer to the vertex by the derived weighting factors.

This process realized the bridging domain method in the PFC/FLAC coupling scheme by a ball-zone logic wherein a certain width of overlapped area composing discrete particles and continuous zones interact with each other, as shown in Fig. 6- 2a.

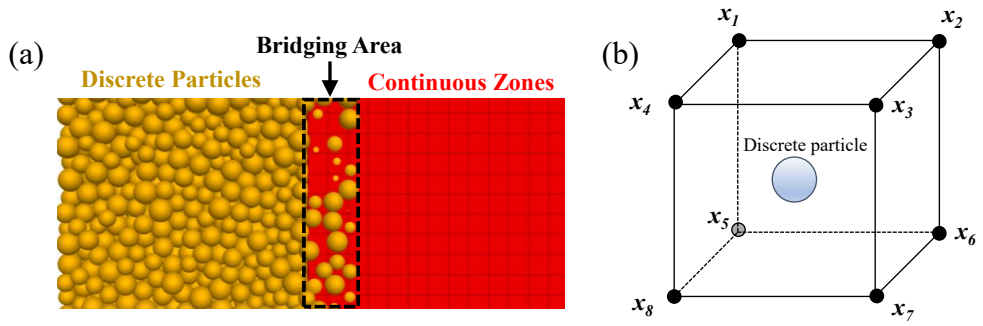

Fig. 6- 2 Depiction of coupling approach (a) and interpolation scheme (b) of ball-zone logic in PFC/FLAC

The ball-zone coupling scheme determines the displacement $\overrightarrow{d_J}$ of the discrete particles by the interpolation function x_{mi} based on the displacements $\overrightarrow{u_x}$, of the eight grid points x_i, i=1,2, ··,8, of the continuous zone that surrounds the discrete (Breugnot et al., 2016; Xiao and Belytschko, 2004) as shown in Fig. 6- 2b. The displacement is described as:

$$\overrightarrow{d_J} = \sum_x^8 x_{mi}\, u_k \qquad \text{(Eq. 6-1)}$$

This scheme achieves the coupling principle by minimizing the total kinematic energy of the bridging area while satisfying Eq. 6-1 at the same time.

6.3 Coupling strategy

To validate the coupling model development and determine the best coupling strategy for investigating the sensitivity of laminated roof response to bedding plane parameters under the impact of longwall panels, we first conducted a preliminary coupling test. We generated a cuboid subjected to the uniaxial compressive stress to evaluate the coupling methods in comparison. The numerical analysis focuses on the strain-stress response of the BPM and continuum material, i.e. strain, Young's modulus, and strength of the numerical rock mass.

The cuboid uniaxial compressive specimens had a dimension of 50×50×100 mm. The boundary conditions between the BPM and the FDM zones were sited in the middle of the numerical sample. Fig. 6- 3 shows the cross-section of the uniaxial compressive specimen using ball-zone coupling and wall-zone coupling.

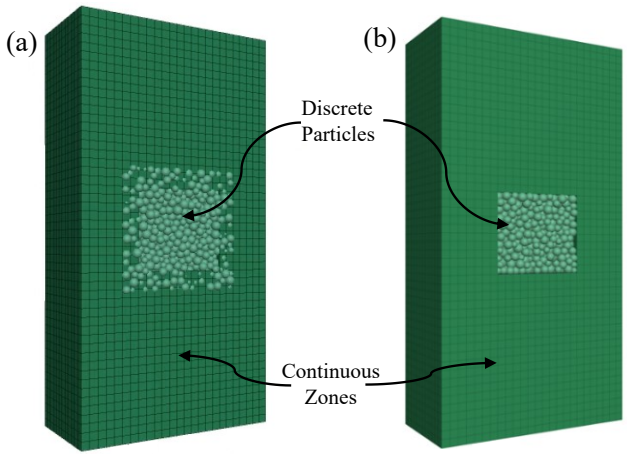

Fig. 6- 3 Depiction of uniaxial compressive specimens generated with (a) ball-zone coupling method and (b) wall-zone coupling method.

The calibration of FDM and BPM are pre-procedure for setting up the coupled model. This procedure used laboratory test data of Berea sandstones for calibrating the coupling model. The uniaxial compressive strength and Young's modulus served as the major index for the calibration. This procedure calibrated the BPM and continuum material separately before coupling them together. This strategy simplifies the parameter selection for the coupled model. This study then conducted numerical uniaxial compressive tests with the BPM and continuum separately until it reached the similar Young's modulus and uniaxial compressive strength with the laboratory results listed in Table 6- 1. It is important to note that during the numerical test, this model fixed the lateral deformation at the top and bottom surface to take the end effect into account (Xu and Cai, 2017).

Table 6- 1 Laboratory uniaxial compressive tests of Berea sandstone

	Specimen #1	Specimen #2	Specimen #3	Average
Young's modulus, GPa	11.25	9.95	10.16	10.45
UCS, MPa	63.69	65.74	58.10	62.51

The coupled model used the Mohr-Coulomb model for continuum and the parallel bonded model (Itasca, 2018) for the BPM. Fig. 6- 4 shows calibrated results of the final failure pattern and the stress-strain curve during the numerical test from which the UCS of the continuum material was 62.0 MPa and Young's modulus was 9.51 GPa. The UCS of the BPM was 61.0 MPa and Young's modulus of the BPM was 10.34 GPa. In general, the continuum and BPM both showed good agreement with the laboratory test results.

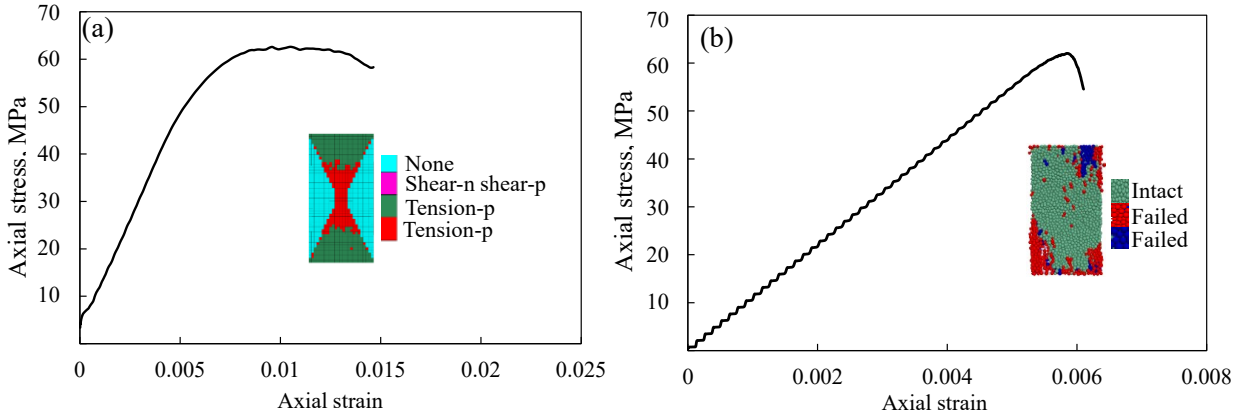

Fig. 6- 4 The stress-strain curves of (a) the continuum (b) BPM under uniaxial compressive load

We then applied the calibrated parameters for both the continuum and BPM to coupling models obtained through the wall-zone coupling method and ball-zone coupling method respectively, which is shown in Fig. 6- 5 and Fig. 6- 6. Fig. 6- 5a shows that the curve of both the continuum and BPM are parallel in their linear portion, indicating a similar Young's modulus in the coupled model. The peak load of BPM in the coupled model was 68.78 MPa and that of the continuum was 65.49 MPa. It seems that the BPM has a higher strength than the continuum. The possible explanation is that the continuum surrounds the BPM, applying confining stress to the BPM. The yielding and post-peak portions of these two curves vary in shape because of the different failure criteria they are following. Fig. 6- 5b depicts the displacement distribution in the wall-zone coupling model. We observed that the BPM and continuum are continuous in displacement, meaning that these two materials are coupling well. Generally, Fig. 6- 6 showed the same consistency with that observed in Fig. 6- 5, indicating that the ball-zone coupling method also worked to couple the two distinct materials.

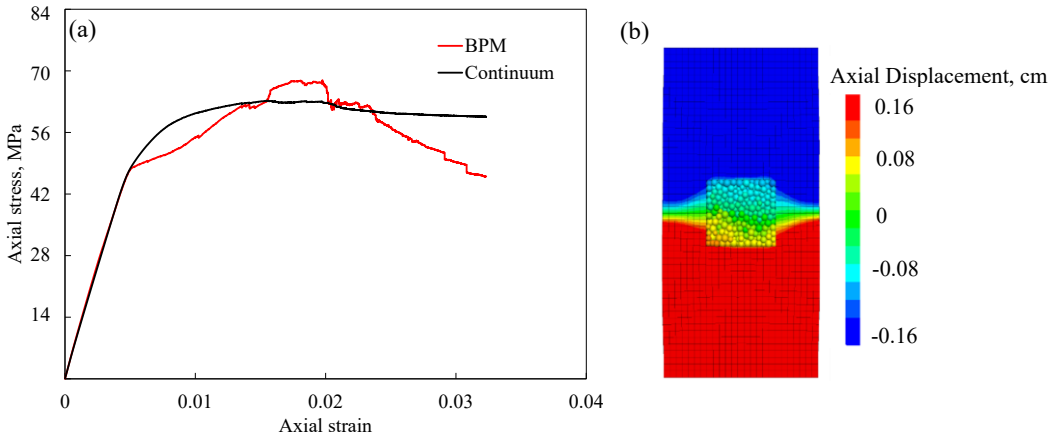

Fig. 6- 5 Stress-strain curves (a) and displacement distribution (b) of the calibrated wall-zone coupling model

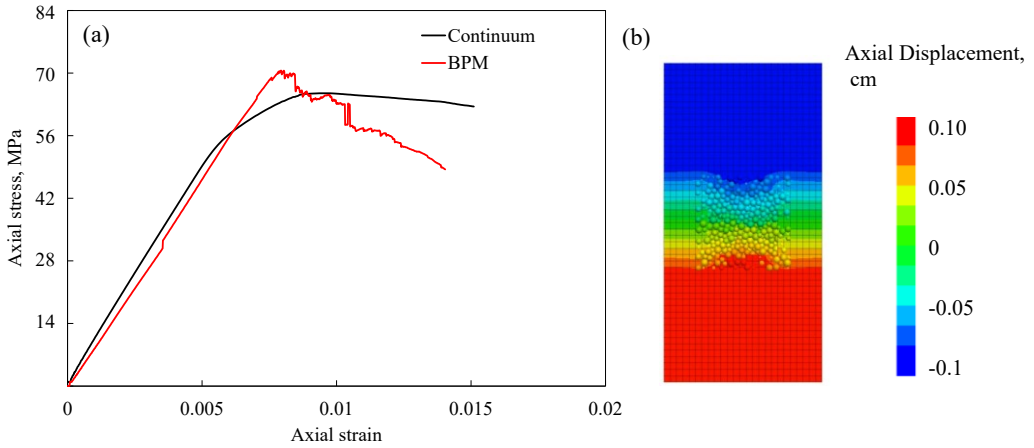

Fig. 6- 6 Stress-strain curves (a) and displacement distribution (b) of the calibrated ball-zone coupling model

In conclusion, both the ball-zone coupling method and wall-zone coupling method achieved good stress-stain consistency between the continuum and BPM. In fact, these methods achieved stress consistency by ensuring the strain/displacement consistency, which is illustrated in Fig. 6- 5b and Fig. 6- 6b, and identical stiffness between the two distinct materials. Here the separately calibrated BPM and the continuum based on the same laboratory data ensure the identical stiffness, and therefore their stress-strain behaviors match well.

6.4 Panel scale modeling with coupling method

In this section, we created a coupled panel scale model with the wall-zone coupling method. The geological conditions were as per a longwall coal mine (Esterhuizen et al., 2019) in the US. In the coupled model, we shortened the length along the panel strike to only 0.3 m as a plane strain model. The purpose of this model is to observe the laminated roof response under the effect of lamination properties when subjected to entry excavation and longwall panel extraction. Therefore, this model created the area of interest, the laminated roof of the entries, by laminated BPM with PFC3D as shown in Fig. 6- 7. We calibrated the laminated BPM based on the laboratory tests of the roof. The ribs, floor, and far-field surrounding rock were created with a continuum with FLAC3D.

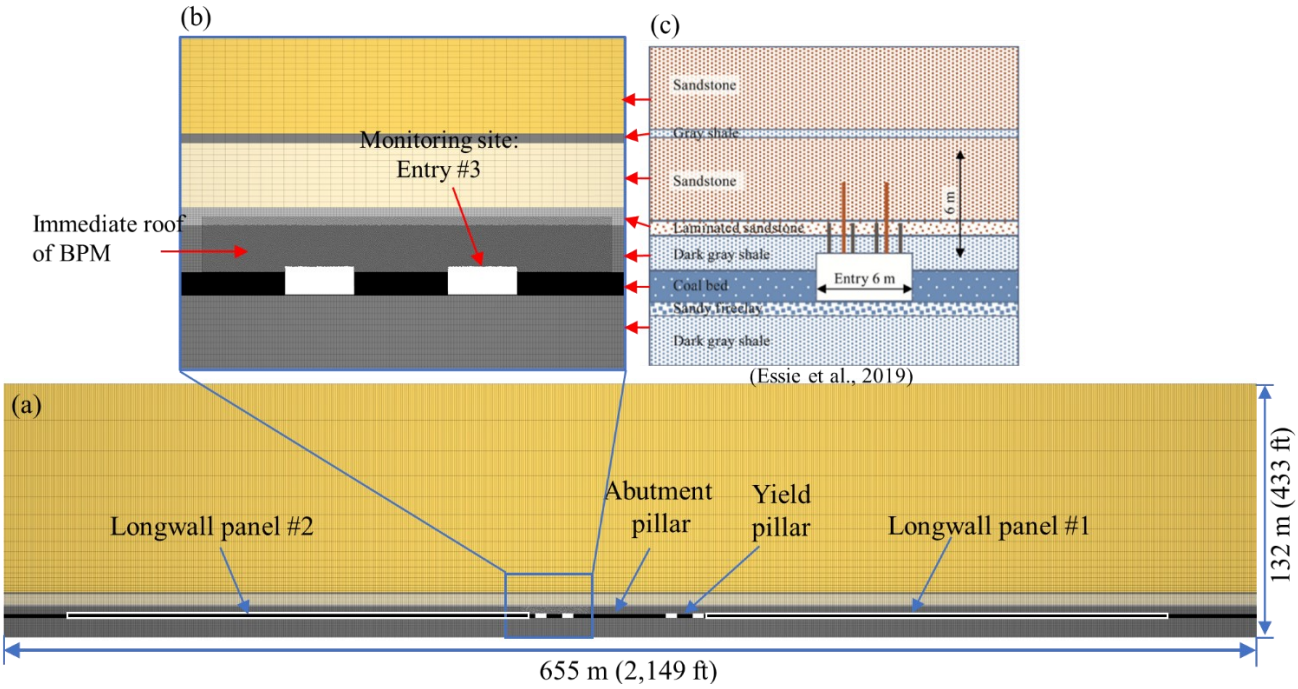

Fig. 6- 7 Illustration of (a) set up of longwall panel, (b) geological setting of the model, and (c) geological condition of the actual mine site

The coupled numerical models generated laminated BPM with the parallel bonded model and smooth joint model. The parallel bonded model can reproduce the bedding, while the smooth joint model can replicate the bedding planes. The modeling procedures consisted of four steps. The first step involved calibrating the laminated BPM based on the actual test data on shale. The second step involved calibrating the continuum material with the same data. The third step involved installing the laminated BPM into the continuum domain with the wall-zone coupling method verified before. Last but not least, the coupling model simulated entry and panel extraction and compared the ground response with the field observations for verifying this coupling model.

6.4.1 Calibration of the laminated BPM representing shale roof

The laminated BPM is a transversely isotropic (TI) material with different stiffness parallel and perpendicular to the bedding planes. In the coupling method, stiffness plays a key role in achieving stress consistency. Therefore, the horizontal stiffness and perpendicular stiffness of the laminated BPM should be consistent with the adjacent continuum material. The calibration procedures used in Chapter 3 and Chapter 4 are therefore not applicable for calibrating the coupling models. Therefore, this study summarized the reported calibration strategies and proposed a practical method for calibrating a TI model with DEM. This section calibrated the laminated BPM based on

the actual test data of shale in this section. The present research calibrated the laminated BPM with the shale cored from the underground mines (Esterhuizen et al., 2019; Jin et al., 2018).

In a DEM, the model consists of two different models, one representing bedding and one representing the weak planes. According to the mechanism of the PFC, there are at least ten micro parameters that contribute to the macro behavior of the TI model. Therefore, calibration is not only the beginning step of the TI rock numerical research but also the most difficult and time-consuming procedure in numerical research. The complexity and uncertainty of the TI model bring an obstacle to the application of this method and somewhat limit this valuable method to academic researchers. Though the studies mentioned above posted good results of the calibrated model, most obtain the combination of these parameters through a trial-and-error approach, which makes their results not replicable if the research objective changes. For example, most researchers focused on laboratory scale modeling wherein the particles are relatively finer than that in a large-scale model. Unlike the continuum-based numerical method, the particle size in a BPM does not only impact the model resolution but also the mechanical characteristics. Therefore, recalibration would be necessary when applying the BPM to a field-scale problem.

Considering the inconvenience caused by this scenario, Potyondy (2004) suggests a bonded particle model calibration, which makes the utilization of BPM easier and more popular. However, the suggested procedure is only applicable to BPM composed of a single contact model, i.e. parallel bonded model or flat joint model. As for the TI model incorporating two contact models, there is no systematic summary for efficient calibration.

To calibrate a three-dimensional TI model replicating the coal mine shale roof, this section details a large number of attempts made and techniques proposed to quickly calibrate the TI model.

6.4.1.1 Calibration procedure

Table 6- 2 shows a list of micro parameters that need to be calibrated in the TI model. Considering that the shale beddings are horizontal in the case study mine, this study calibrated the TI model from two directions wherein the inclination angles of the bedding planes are set as 0° and 90° respectively. The following steps summarize the proposed calibration procedures.

Step 1: Generation of intact rock with a specific modulus

This step covers the calibration of the modulus of the matrix, generated with a parallel bonded model, for the installation of the smooth joint in the following step. Potyondy (2019) describes the recommended procedure for calibrating a parallel bonded model in detail. The calibrated modulus of the matrix should be slightly higher than both the modulus parallel to the bedding planes (E_0) and the modulus perpendicular to the bedding planes (E_{90}) of the targeted actual rock. The current step does not consider the strength UCS.

Step 2: E_0 and E_{90} calibration by varying the normal and shear stiffness ($k_{n,sj}$ and $k_{s,sj}$) of the smooth-joint contact model

After installing the smooth joints into the matrix whose modulus was calibrated as above, this step considers the E_0 and E_{90} of the TI model. We initiated the cohesion (C_{sj}), tension ($\sigma_{t,\,sj}$), and friction angle (μ_{sj}) of the smooth joint at their approximate laboratory values and kept them constant at this step. This step does not consider the uniaxial compressive strength parallel and perpendicular to the bedding plane (UCS_0 and UCS_{90}).

We adjusted the E_0 by iteratively varying the normal stiffness of the bedding plane ($k_{n,sj}$) and increased the E_{90} by increasing the shear stiffness of the bedding plane ($k_{s,sj}$). This is because the smooth joint interacts with the matrix when subjected to loads. In PFC, one can envision the smooth joint contact as a series of springs distributed along the plane with shear and normal stiffness at the same time, as shown in Fig. 6- 8. Therefore, when the TI model deforms under a load perpendicular to the plane, the smooth joint contact deforms due to the existence of the normal stiffness of the bedding plane ($k_{n,sj}$), introducing a relationship between the macro modulus of the TI model with the modulus of the smooth joint contact. Likewise, when the TI model deforms under a load parallel to the plane, the smooth joint deforms accordingly due to the existence of shear stiffness ($k_{s,sj}$).

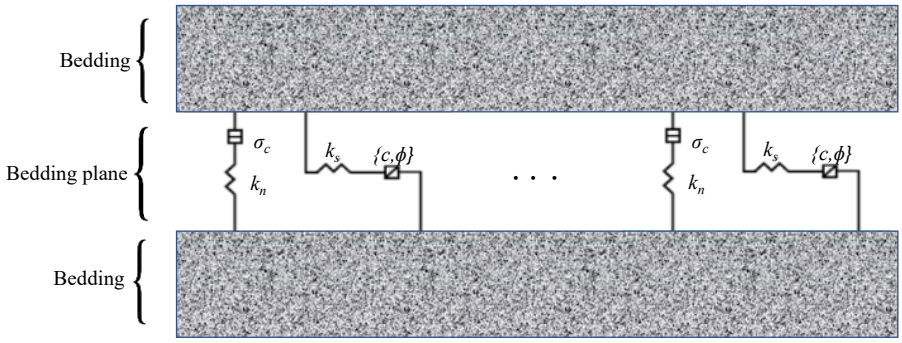

Fig. 6- 8 Smooth joint contacts with normal and shear stiffness uniformly distributed on plane

This increasing trend of E_0 with $k_{n,sj}$ is also comparable to the analytical solution of the elastic modulus with an inclination angle of β, which is calculated as shown in Eq. 6-2 (Amadei, 1982):

$$\frac{1}{E_\beta} = \frac{1}{E_r} + cos^2\beta \left(\frac{cos^2\beta}{k_n\delta} + \frac{sin^2\beta}{k_n\delta}\right) \quad \text{Eq. 6-2}$$

where E_r is the elastic modulus of the beddings, δ is the spacing of the beddings, and k_n and k_s are the normal and shear stiffness of the weak planes, respectively. When $\beta = 0^\circ$, $\frac{1}{E_0} = \frac{1}{E_r} + \frac{1}{k_n\delta}$, demonstrating that the E_0 increases with the increment of $k_{n,sj}$. However, when $\beta = 90^\circ$, $\frac{1}{E_{90}} = \frac{1}{E_r}$, demonstrating the macro modulus of the TI model does not change with the bedding plane stiffness, which is somehow different from the trend we observed in our numerical TI model. In our TI model, E_0 increases with $k_{s,sj}$. This is because the ideal condition-based analytical solution does not consider the bumpiness of the weak cohesive planes. Due to the bumpiness, the actual weak plane is not straight and has a certain thickness that is not imposed by the analytical solution. Fig. 6- 9 show contact bonds in the TI model wherein the smooth joint bonds are shown with a certain bumpiness and thickness. We argue that the scenario observed in the TI model could be more realistic than the results of the analytical solution and this argument is supported by reported research (Park et al., 2018) and also our laboratory discussions in Section 3.5.

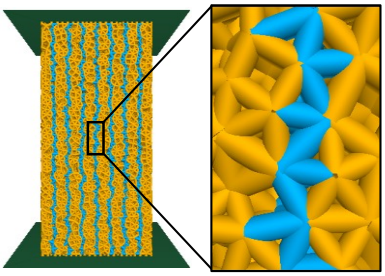

Fig. 6- 9 Contact bonds in a TI model embedding a set of vertical weak planes, which has a rough surface with a thickness

Step 3: UCS_0 and UCS_{90} calibration by adjusting $\sigma_{t,pbm}$ and C_{pbm}

After the modulus of the TI model attained the laboratory value, this step then calibrates the UCS of the model. According to our calibration practice, in most cases this step does not need to consider the tensile and cohesion strength ($\sigma_{t,sj}$ and C_{sj}) of the bedding plane.

Firstly, this step begins by adjusting the UCS in the direction of perpendicular to bedding planes (UCS_0) by varying the tensile strength of the bedding ($\sigma_{t,pbm}$) and cohesion of the bedding (C_{pbm})

until the targeted laboratory UCS_0 was reached. Whether the $\sigma_{t,pbm}$ or C_{pbm} should be firstly varied depending on the cracks that are developing within the matrix. For example, if one finds the model fails by tension cracks, one should increase the $\sigma_{t,pbm}$ to increase the strength of the model; vice versa, if the model is failing in shear cracks, one should increase the C_{pbm} first. We observed that after the calibration in the first step, usually the $\sigma_{t,pbm}$ and C_{pbm} did not need to be adjusted drastically. This is because the bedding plane has a limited impact on the strength of the TI model with an inclination angle of 0° and 90° (Amadei and Goodman, 1982; Park et al., 2018).

Usually, when calibrating the UCS_0, this step also involves calibrating the UCS_{90}. In our calibration practice, we found that sometimes there was a slight deviation of UCS_{90} from the targeted value. One can solve this problem by varying the bedding plane tensile strength ($\sigma_{t,sj}$) and cohesion strength (C_{sj}).

Step 4: Calibration of the $\sigma_{t,sj}$ and C_{sj} in a model with a plane inclination angle of 45°

According to the analytical solution of an unconfined strength σ_1 expressed in Eq. 6-3 (Jaeger et al., 2007), the bedding planes strength parameters $\sigma_{t,sj}$ and C_{sj} affects the strength of the TI rock only when the inclination angle (β) does not equal 0° or 90°.

$$\sigma_1 = \frac{2C_w}{(1-tan\varphi_w\, cot\beta)\cdot sin2\beta} \qquad \text{Eq. 6-3}$$

where φ_w represents friction angle, C_w represents cohesion, and β is the inclination angle of bedding planes. Therefore, one can only use a TI model where $\beta \neq 0°$ or 90° for calibrating the strength parameters of the smooth joint contact model. This study used an inclination angle of 60° and adjusted the UCS_β of the TI model by iteratively varying the $\sigma_{t,sj}$ and C_{sj}. Whether $\sigma_{t,sj}$ or C_{sj} should be varied first depending on the crack developing at the weak planes as described in step 3.

6.4.1.2 Calibrated results of laminate BPM

With the proposed calibration procedure, this study calibrated the TI model to model the immediate shale roof. The UCS_0 of shale at this mine was 70.0 MPa (Esterhuizen et al., 2019). To get the UCS of the laminated BPM and the elastic modulus from both directions parallel and perpendicular to the bedding planes, the present research uses a shale with similar strength (Jin et al., 2018) for the calibration. This study tested the shale with an axial load applied parallel and perpendicular to the bedding plane respectively; Table 6- 3 gives the tested properties.

Table 6- 3 UCS and elastic modulus of the shale from directions parallel and perpendicular to the bedding planes (Jin et al., 2018)

$\beta, ^\circ$	E_β	UCS_β
0 (Perpendicular)	16.53 GPa	61.82 MPa
90 (Parallel)	36.96 GPa	57.39 MPa

The data in Table 6- 3 includes the laboratory results which must be scaled when applied to field-scale problems. Researchers have discussed the scale effect of rock mass for years. Tulu et al. (2018) used empirical scale equations obtained from abundant tests on US coal measure rocks. For example, they used a scale factor of 0.58 for the strength parameter for various kinds of rock mass, including coal, shale, and sandstone. For Young's modulus, they used Eq. 6-4 for sandstone and shale and Eq. 6-5 for limestone. In Eq. 6-4 and Eq. 6-5, the UCS is the laboratory scale value in MPa and the resultant elastic modulus is in GPa.

$$E = 0.143 \times UCS + 6.16 \quad \text{Eq. 6-4}$$

$$E = 0.1162 \times UCS + 15.24 \quad \text{Eq. 6-5}$$

Eq. 6-4 was obtained based on the laboratory test perpendicular to the bedding planes. Since the TI of shale was not considered in this equation. If using Eq. 6-4 for parallel direction (E_{90}), the value of parallel is even smaller than that of perpendicular (E_0) here, which is implausible since this would conflict with laboratory results. In fact, in the parallel direction, the weak planes have little effect on the elastic and strength properties of rock mass (Park and Min, 2015). One can envision the shale as a continuum such as limestone in this direction. Therefore, this study used Eq. 6-5, applicable for limestone. Table 6- 4 shows the calculation of the scaled elastic modulus and strength with an inclination angle of 0°and 90°.

Table 6- 4 Scaled parameters for the shale roof

	Laboratory scale		Field scale	
$\beta, ^\circ$	E_β	UCS_β	E_β	UCS_β
0 (Perpendicular)	16.53 GPa	61.82 MPa	15.00 GPa	35.86 MPa
90 (Parallel)	36.96 GPa	57.39 MPa	21.91GPa	33.29 MPa

We then followed the procedure proposed in section 6.4.1 to calibrate our laminated BPM.

After step 1, we generated a matrix with an elastic modulus (25.51 GPa) slightly higher than the *max*(E_0, E_{90}) (22.06 GPa), as shown in Fig. 6- 10. This step does not consider the strength UCS.

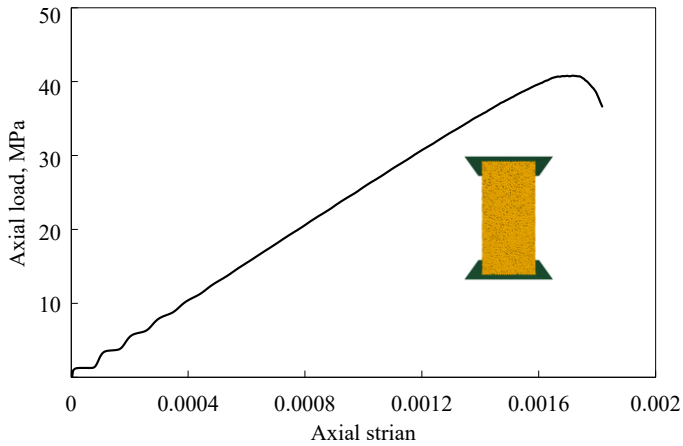

Fig. 6- 10 Generation of intact rock with elastic modulus (25.51 GPa) slightly higher than the max (E_0, E_{90})

After steps 2 and step 3, we calibrated the TI model as shown in Fig. 6- 11. The E_0, E_{90}, UCS_0, and UCS_{90} of the calibrated TI model are 15.86 GPa, 21.37 GPa, 34.49 MPa, and 34.0MPa respectively, which were in good agreement with the field scale parameters in Table 6- 4.

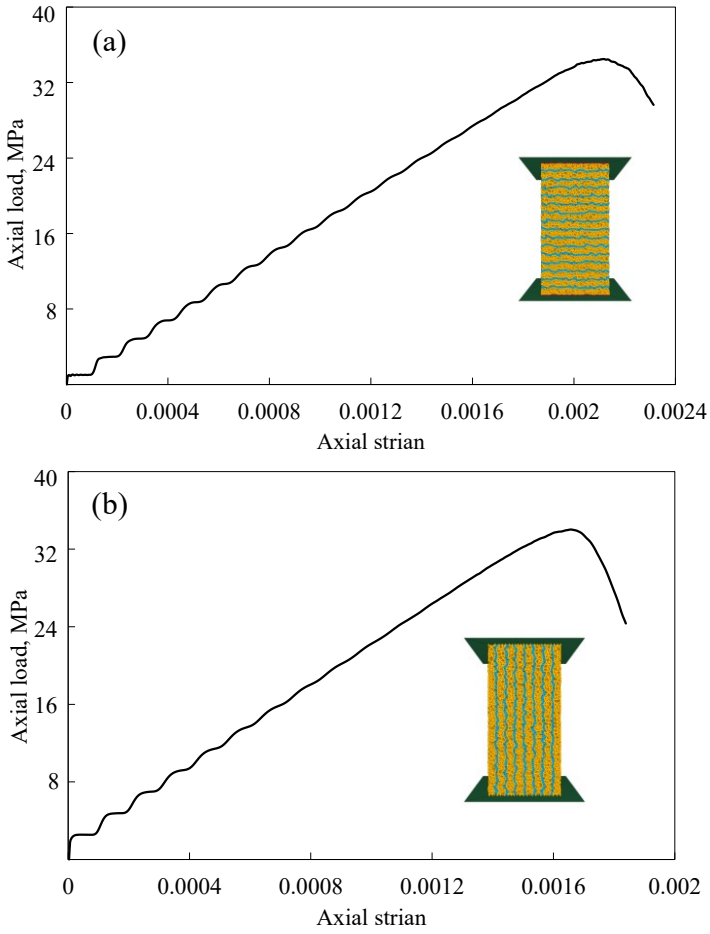

Fig. 6- 11 Calibrated TI model with an inclination of (a) 0˚ and (b) 90˚

6.4.2 Generation of the coupling panel

Based on the plane strain panel geometry shown in Fig. 6- 7, we coupled the calibrated TI laminated BPM into the continuum domain as the immediate roof of two entries near the #2 panel. We coupled the TI laminated BPM into the FDM model with a width of 35 m. The height of the BPM was slightly larger than the shale roof. It is important to note that the continuum material adjacent to the TI model was set to have the same E_0 with the TI model to ensure the applied in situ stress could transfer to the TI model.

This model fixed the left, right, and bottom boundaries of the FDM. It applied horizontal stress to the left and right boundaries and vertical stress to the top boundary to represent the overburden weight. Field measurement obtained the in situ stress, i.e. horizontal and vertical stress. Stress measurements conducted at the mine indicated a maximum horizontal stress of approximately 21.00 MPa oriented at N58E, and a minor horizontal stress of approximately 14.0 MPa. According to the layout of the entry, the angle (α) between the orientation of the maximum stress and the longitudinal axis of the test entry is approximately 32°, as shown in Fig. 6- 12.

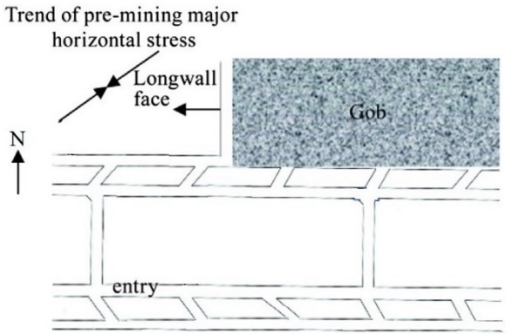

Fig. 6- 12 Direction of entries and horizontal stresses (modified form (Esterhuizen et al. 2019))

Therefore, the following equations resolved the horizontal principal stresses to the model boundary (Boresi and Schmidt, 1985):

$$\sigma_\alpha = \frac{\sigma_x+\sigma_y}{2} + \frac{\sigma_x-\sigma_y}{2} cos2\alpha = 15.9 \text{ MPa} \quad \text{Eq. 6-6}$$

$$\tau_\alpha = \frac{\sigma_x-\sigma_y}{2} sin2\alpha = 3.2 \text{MPa} \quad \text{Eq. 6-7}$$

Where $\alpha = 58°$.

The Pocahontas No. 3 seam overburden depth in the test coal mine varies from 430 to 732m (Esterhuizen et al. 2019). This model set the vertical stress as 12.0 MPa, corresponding to a depth of 500m.

The model simulated the support system by coupling cable elements into the BPM domain. This system installed four rows of bolts with a length of 1.8 m at a spacing of 1.2 m and two rows of cable with a length of 3.6 m as per Fig. 6- 7c in section 6.3.

6.4.3 Verification of the coupled panel

Filed observations at the test mine provide an opportunity to determine whether the developed numerical coupled model would satisfactorily replicate the rock mass response at this mine site. The coupled model simulated the panel through three steps. The varication was conducted during each step. Firstly, we calculated the model to equilibrium before development. We then compared the stress in the BPM to that in the FDM to ensure the boundary condition setup transferred to the TI laminated BPM successfully. Secondly, to simulate entry development, we excavated the entries and calculated them to equilibrium without a support system, and then compared the depth of the unstable roof and the yield depth in the ribs in the abutment pillar with field observation to further verify the model. Thirdly, we extracted the longwall panel in a supported model and calculated. We then compared the supported roof response with an unsupported roof to verify the performance of the support system. Lastly, we compared the BPM roof deformation after the #2 panel extraction with that measured in the field for model verification. The verification results are as follows.

After step 1, the measurement station in the BPM roof showed that the horizontal and vertical stress was 15.5 MPa and 11.0 MPa respectively, which matches well with the preset in situ stress σ_{xx}=15.9 MPa and σ_{zz}= 10.1 MPa. Step 2 simulated the developed model with and without a support system respectively. Fig. 6- 13 shows the displacement distribution of the coupled model and force distribution in the BPM immediate roof after development. The supported roof in Fig. 6- 13 also illustrates the simulation of the support system coupled into BPM material. The cable target link shows the perfect establishment of the link between the particles and cable. The porosity of the BPM caused the minor unlinked part.

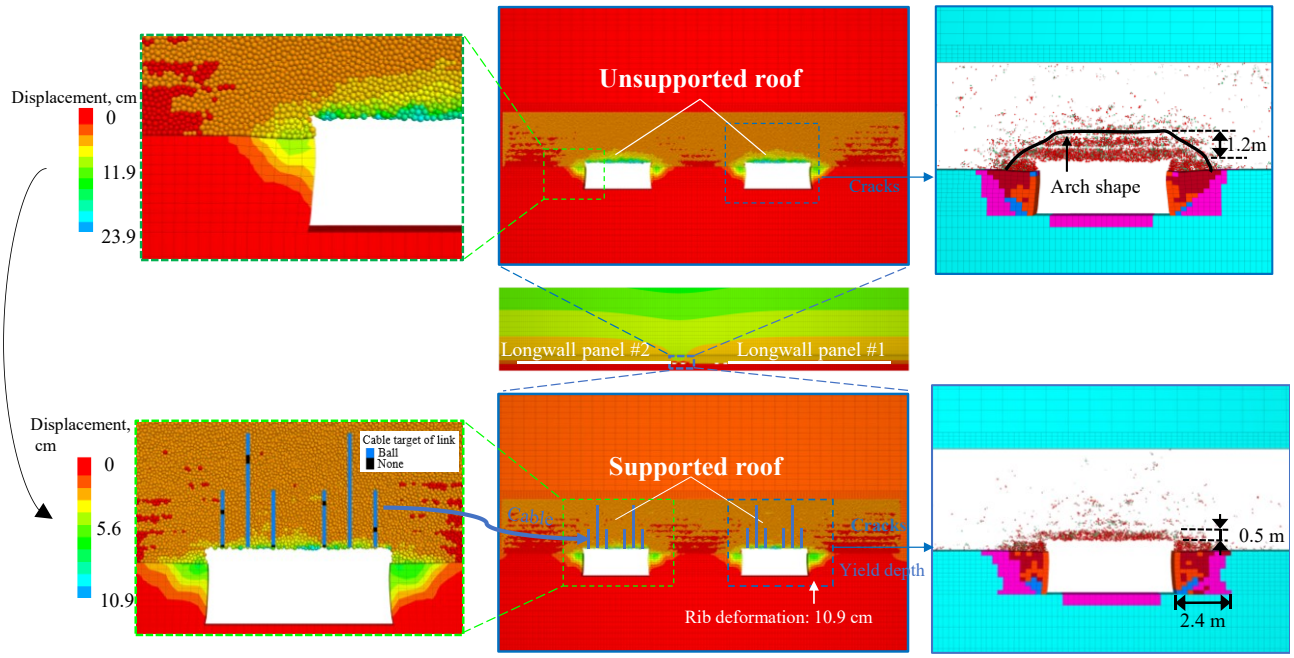

Fig. 6- 13 Displacement and crack distribution of supported and unsupported entry after development

As shown in the displacement distribution in Fig. 6- 13, in both the unsupported and supported model, the displacement is continuous between the BPM and continuum material, ensuring that the boundary conditions are continuously transferred to the BPM as the model is running. The unsupported roof has a maximum roof fall of 23.9 cm and the supported roof deformed 10.9 cm, verifying the simulated support system. The crack distribution in the BPM roof after excavation of the model in Fig. 6- 13 shows that the lower 1.2 m of the unsupported roof failed completely, which agrees well with the field observation. The supported roof is relatively intact since only 0.5 m of the BPM roof failed. In addition, the rib deformation and the yield depth of the rib after development were 10.9 cm and 2.4 m respectively in the model, both showing good agreement with measured results in the field.

Fig. 6- 14 shows roof deformation and the roof fracturing after extracting both panels. The extracted model has a maximum roof sag of 26.6 mm in the model, which agrees well with the measured results. The fractured part of the roof occurs mainly above the entry and extends to the top boundary of the TI laminated BPM. Fig. 6- 15 shows the comparison of roof deformation at various depths of the model between the modeling results and measured results after extracting both panels. As illustrated in Fig. 6- 15, the shape of the displacement curves of the measured and simulated results are quite close. The maximum roof sag, 30 mm as measured at the mine site, occurred on day 8 of monitoring, while the maximum roof sag of the model is 27mm. In addition,

Fig. 6- 14b shows that the displacement curve is smooth at the interface between BPM and the continuum, verifying the displacement consistency in both the BPM domain and continuum domain. In general, simulated results matched well with field measured data and provided a satisfactory estimate of roof response for the defined geology, loading conditions, and support system. Table 6- 5 and Table 6- 6 list the detailed parameters used for the continuum and BPM in the coupling model respectively.

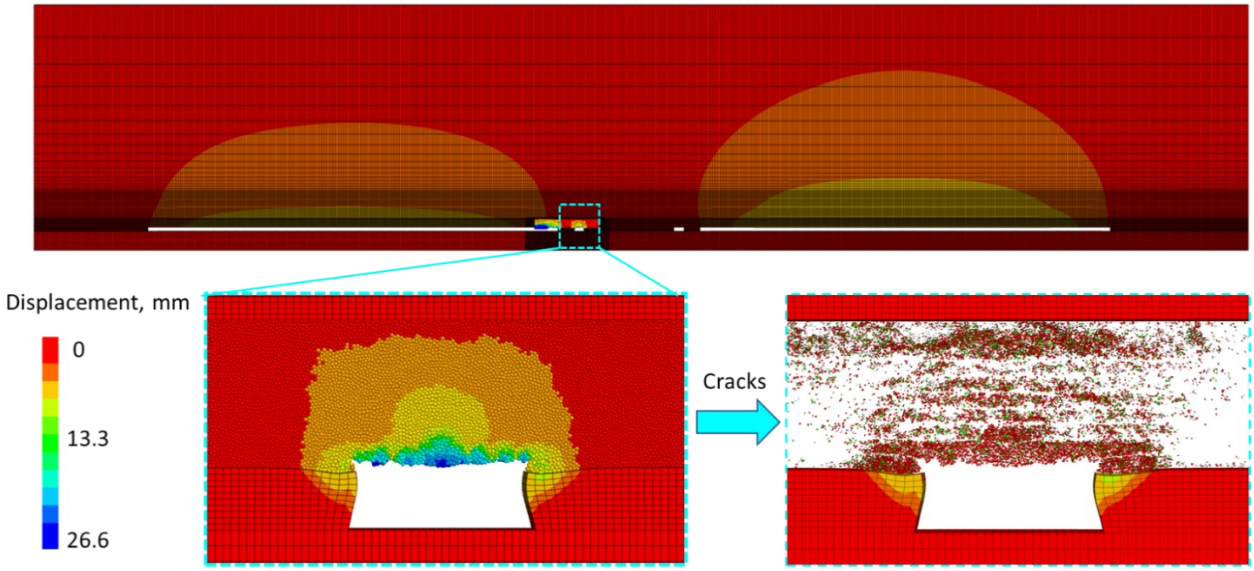

Fig. 6- 14 Roof deformation after panels are extracted

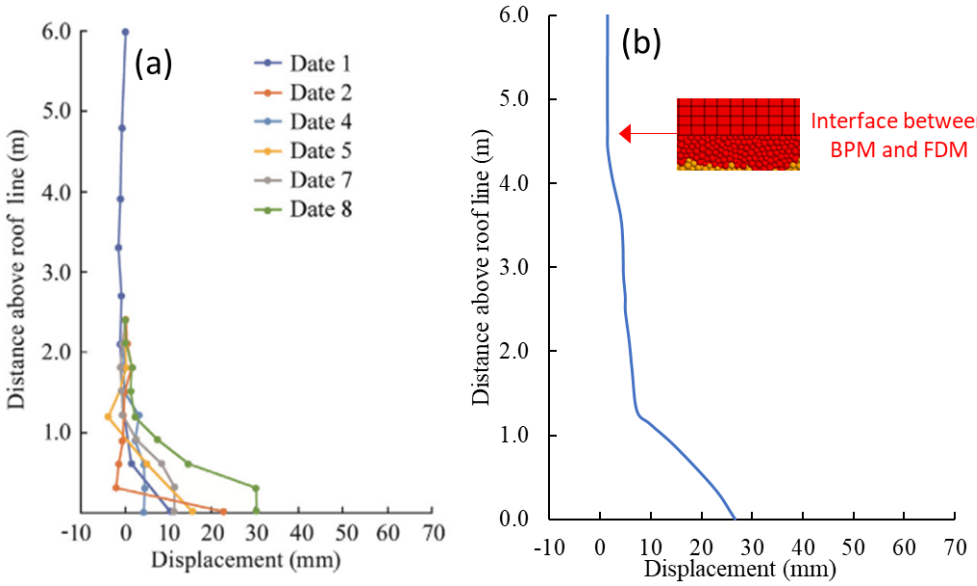

Fig. 6- 15 Roof sag comparison between (a) field measured results (Esterhuizen et al., 2019) and (b) modeling results

Table 6- 5 Calibrated micro parameters of continuum in the TI model

Strata	Bulk ,GPa	Shear ,GPa,	Cohesion, MPa	Friction angle, °	Tension ,MPa
Strong sandstone	15.12	11.03	11.88	48	2.32
Weak sandstone	7.56	5.50	5.94	40	1.16
Gray shale	11.34	5.72	6.13	48	2.30
Laminated sandstone	10.87	7.5	6.55	35	5.1
Coal	7.55	3.36	4.58	20	6.7

Table 6- 6 Calibrated micro parameters in the TI laminated

Constitutive model	Micro parameter	Value
Parallel bonded model	Particle size, mm	5-7.5
	Effective modulus, E_{pbm}, GPa	1.848
	Stiffness ratio, K_{pbm} ($k_{s,\ pbm}/k_{n,\ pbm}$)	1.0
	Tensile strength, $\sigma_{t,\ pbm}$, GPa	7.348
	Cohesion, C_{pbm}, MPa	34.22
	Friction angle, μ_{pbm}, °	25
Smooth joint contact model	Normal stiffness, $k_{n,sj}$, GPa/m	0.6
	Shear stiffness, $k_{s,\ sj}$, GPa/m	4.177
	Tensile strength, $\sigma_{t,\ sj}$, GPa	35
	Cohesion, C_{sj}, GPa	50
	Friction angle, μ_{sj}, °	31

6.5 Effect of bedding plane parameters

Using the verified coupling model above, we conducted a series of simulations to systematically analyze the sensitivity of bedding plane strength and the cohesion-to-tensile ratio of the bedding plane on the response of laminated roof under various loading conditions caused by development and panel extraction.

6.5.1 Effect of bedding plane strength

This study analyzed the effect of bedding plane strength by the reduction in cohesion and tensile strength of the bedding plane simultaneously. The declining gradient was 1.0, 0.82, 0.64, 0.46, 0.28, and 0.10. In each case, this study analyzed the roof responses under the three loading conditions listed above in comparison. The roof response included the roof deformation, fracturing mechanism (shear or tension), and the broken bond location in the roof. Fig. 6- 16 lists the simulation study contents. The fracturing mechanism observation can demonstrate how the roof (shear or tension) fractures when subjected to different loading conditions. The broken bond location observation can tell us whether the bedding planes or beddings are failing.

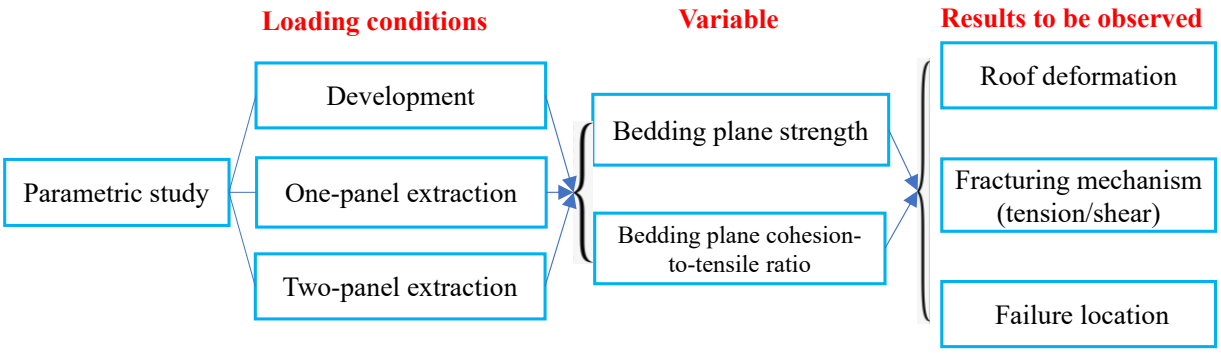

Fig. 6- 16 Parametric study contents of laminated roof using coupling models

Fig. 6- 17 showed the maximum roof sag variations with different bedding plane strengths under loading conditions of development, one-panel extraction, and two-panel extraction. Fig. 6- 17 shows that whatever the strength ratio is, the curve of development is significantly higher than that of two-panel extraction and one-panel extraction. In addition, the extraction of the second panel caused a slightly higher roof sag than that of one-panel extraction. For example, when the strength is 1.0, the roof sags under these three loading conditions are 32.0 cm, 7.0 cm, and 1.0 cm respectively. This demonstrates that with a certain bedding plane strength, the development of the entry caused most roof sag. The extraction of the first panel caused a very minor roof sag which can be neglected from an engineering perspective. This is because the designed pillar system worked well to protect the monitored entry. This simulated result is similar to that measured by the U.S. Bureau of Mines at the Cyprus Plateau Starpoint No. 2 Mine, near Price, UT (Signer and Jones, 1990). Their measured results showed that the one-panel extraction caused a roof sag of approximately 0.8 cm while the two-panel extraction caused a roof sag of approximately 15.0 cm, which was much larger. Also, they monitored the maximum roof bolt load caused by development and longwall panel. Their results showed that the development caused load was higher than that of the panel extraction caused load, which agrees with the phenomenon that development caused the largest roof sag here.

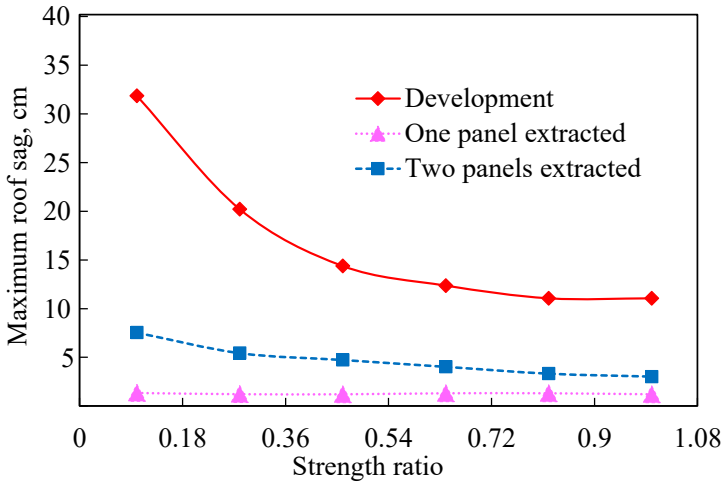

Fig. 6- 17 Effect of bedding plane strength on roof sag under different loading conditions

In addition, all three curves decrease with an increase in the strength ratio in Fig. 6- 17, signifying that higher bedding plane strength increased the stability of the laminated roof. The trend is extremely significant in the case of development. Lastly, the curves became flat when the strength ratio became higher, demonstrating that the decreasing rate of the roof sag decreased when the strength ratio increased. For example, when the strength ratio changes from 0.1 to 0.28, the decreasing rate is 65.0 cm per unit of strength ratio change (from 32.0 cm to 20.0 cm), while the decreasing rate is zero when the strength ratio ranges from 0.82 to 1.0. Therefore, one can conclude that the laminated roof sag is more sensitive to the bedding plane strength when the strength is low.

To further illustrate the effect of the bedding plane strength on the fracturing mechanism of the laminated roof, Fig. 6- 18 introduces the percentage of tensile cracks in the laminated roof. The figure compares the crack percentage under different loading conditions to aid in understanding the sensitivity of the fracturing mechanism to extraction-caused loading conditions. Fig. 6- 18a shows that the increase of the bedding plane strength causes a slight increase in tensile crack percentage in the laminated roof. This effect is more pronounced when the strength ratio is low as shown in Fig. 6- 18a, wherein the black dashed line is steeper when the strength ratio ranges from 0.1 to 0.64. However, this effect is overall a gentle one, since the tensile crack percentage only increases from 84.7% to 89.8% when the bedding plane strength ratio changes from 0.1 to 1.0. In addition, Fig. 6- 18b and Fig. 6- 18c shows these trends occurring in all mining stages, illustrating that loading conditions caused by mining stages did not show a pronounced influence on the fracturing mechanism.

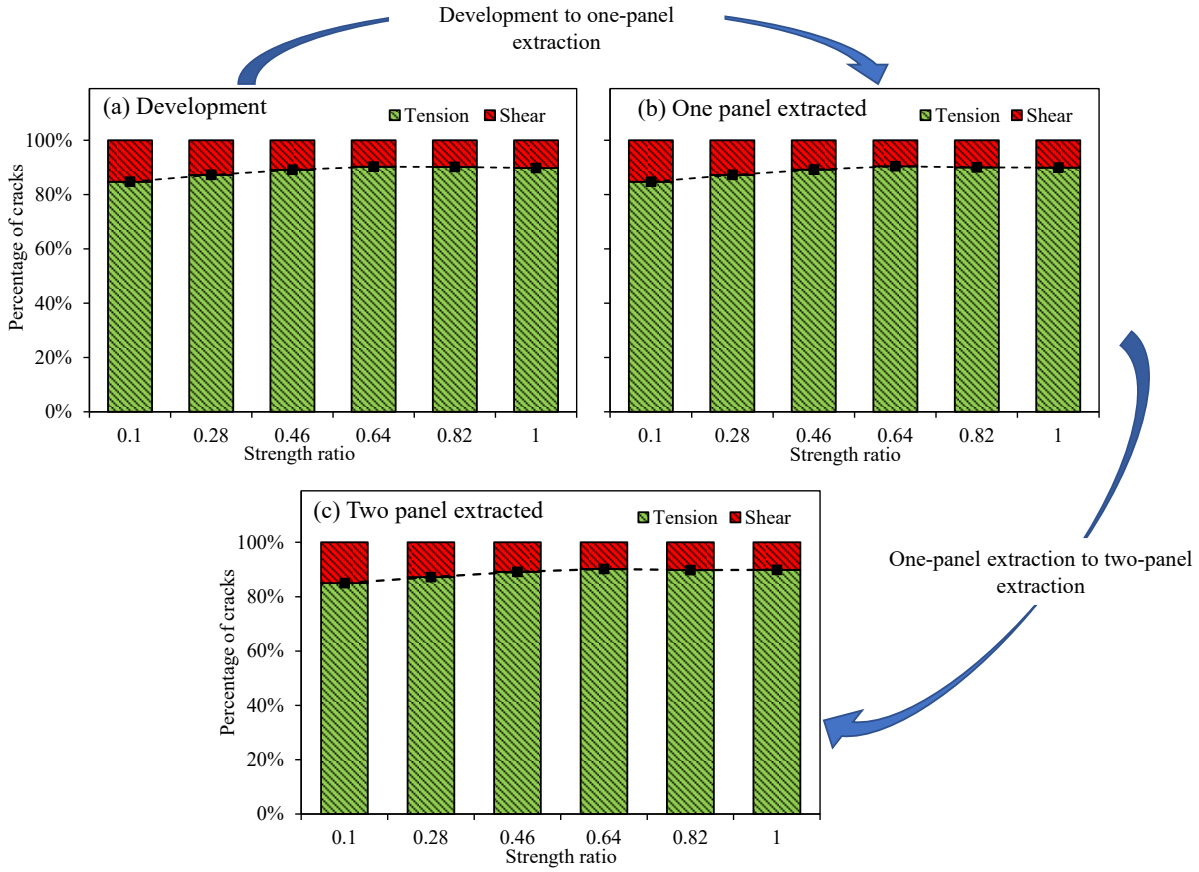

Fig. 6- 18 Effect of bedding plane strength on percentage of cracks under loading conditions of (a) development, (b) one-panel extraction, (c) two-panel extraction (red columns represent shear cracks in immediate roof, green columns correspond to tensile cracks, black dashed lines signify trend of cracks changing with bedding plane strength)

Fig. 6- 19 shows the variation of percentage of broken bonds in the beddings and bedding planes with different bedding plane strengths. This variation can reveal the failure location (in the bedding or along the bedding plane) inside the laminated roof. This study compares the three different loading conditions introduced by mining activities. Fig. 6- 19a shows that the increment of the strength ratio introduces a significant drop of broken bonds in bedding planes, which is understandable based on common knowledge surrounding this phenomenon. Surprisingly, though the fluctuation is gentle in the percentage of broken bonds in beddings, it drops slightly when the bedding plane strength ratio increases. The possible explanation is that the increment of the bedding plane strength increases the laminated roof strength as a whole structure, which causes both the broken bedding planes and broken beddings to decrease simultaneously. Also, the decreasing rate of the broken bonds is significantly higher when the bedding plane strength ratio is low, signifying that the stability of the laminated degenerates rapidly when the bedding planes

are fairly weak. In addition, the broken bond percentage does not vary remarkably under different loading conditions, which agrees well with the cracking mechanism in the last paragraph.

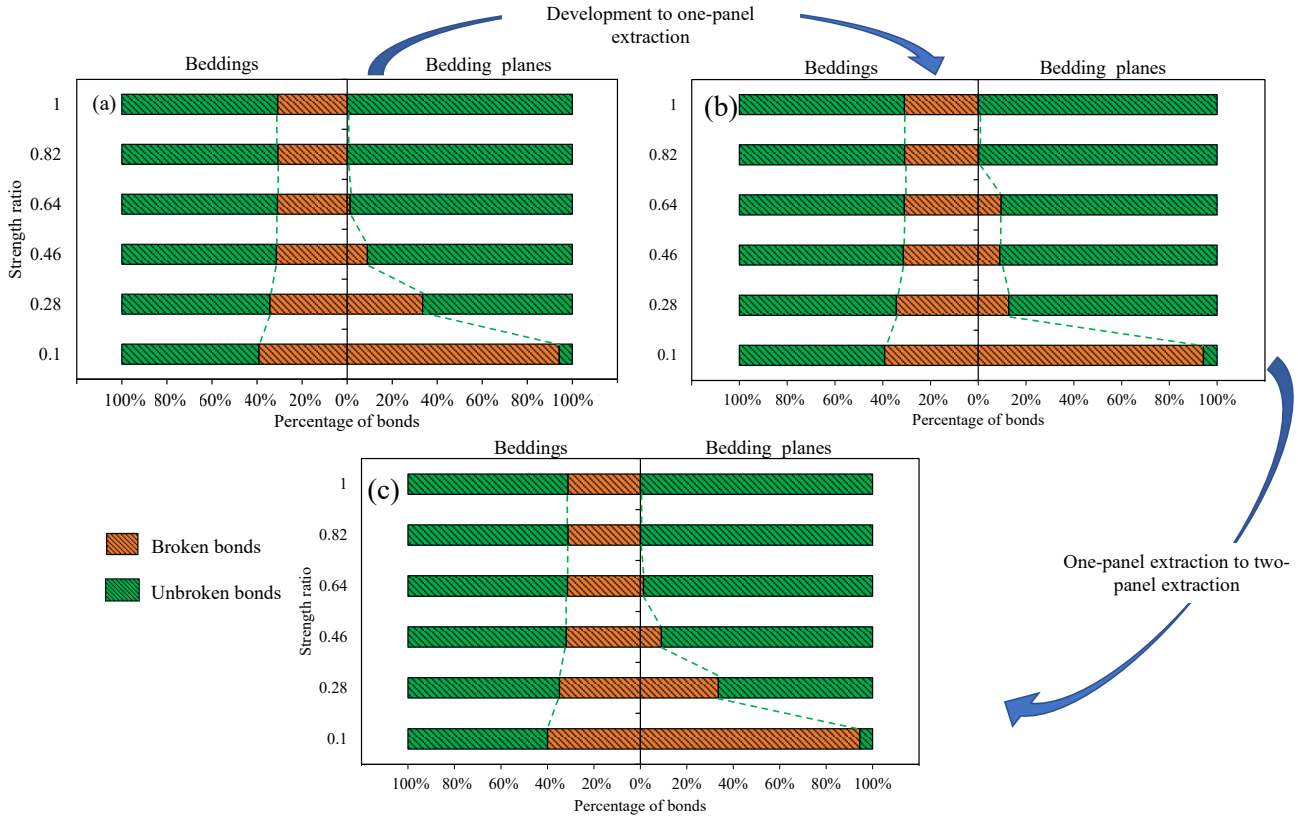

Fig. 6- 19 Effect of bedding plane strength on percentage of broken bonds of both bedding planes and beddings under loading condition of (a) development, (b) one-panel extraction, and (c) two-panel extraction (Orange bars represent bonds remaining unbroken, green bars represent broken bonds. Bars on left side correspond to beddings, bars on right side correspond to bedding planes. Blue dashed lines represent changing trend of broken bond percentage)

6.5.2 Effect of the cohesion-to-tensile ratio

As depicted previously in Table 6- 2, the strength parameters of the bedding plane include cohesion and tensile strength. Researchers have observed that the ratio of the cohesion-to-tensile ratio poses an effect on not only the shale strength but also on the shale failure mode in Brazilian and flexural tests (Chong et al., 2017; Dou et al., 2019a). The present section investigated the effect of the cohesion-to-tensile ratio of the bedding plane on the laminated roof of an underground coal mine entry by varying the smooth joint cohesion while keeping the tensile strength constant at 23.0 MPa. The coupled models adopted seven cohesion-to-tensile ratios: 0.2, 0.4, 0.6, 0.8, 1.0, 1.2, and 1.4. This section investigated the roof sag, cracking mechanism, and broken bonds in each case under the three different loading conditions induced by development and panel extraction.

Fig. 6- 20 to Fig. 6- 22 show the variations of the maximum sag, percentage of tensile cracks, and percentage of broken bonds with different cohesion-to-tensile ratios of bedding plane. These figures only present the data obtained from the development condition, since the percentage of tensile cracks and broken bonds do not vary significantly under different loading conditions.

Fig. 6- 20 to Fig. 6- 22 show that each variation is quite similar to the effect of bedding plane strength. The maximum roof sag decreases when the cohesion-to-tensile ratio decreases. Additionally, the variations, including roof sag, percentage of tensile cracks, and broken bonds, are relatively sensitive when the cohesion-to-tensile ratio is low.

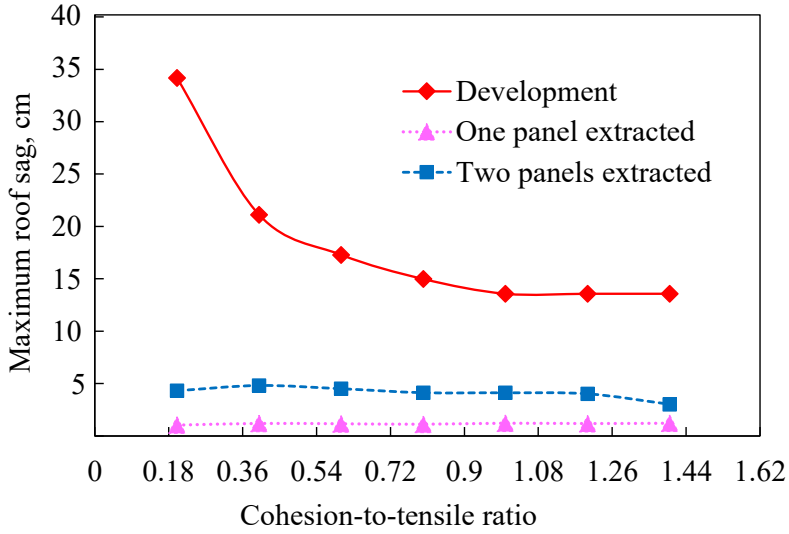

Fig. 6- 20 Effect of bedding plane cohesion-to-tension ratio on roof sag under different loading conditions

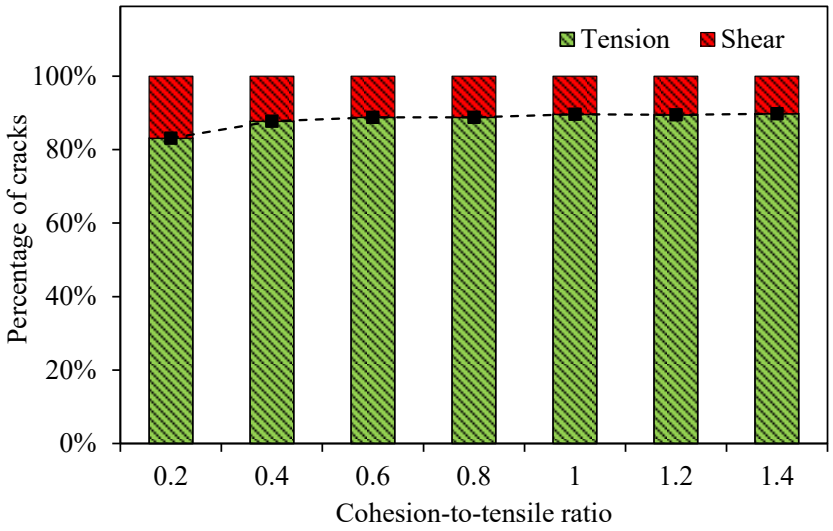

Fig. 6- 21 Effect of bedding plane cohesion-to-tension ratio on percentage of cracks under loading condition of development (legends and marks have the same meaning as in Fig. 6- 18)

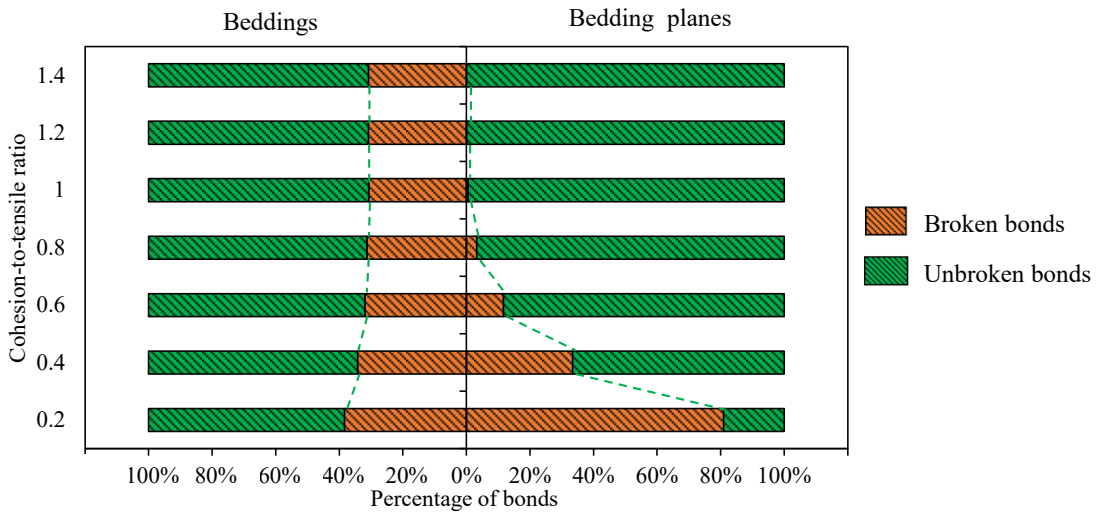

Fig. 6- 22 Effect of bedding plane cohesion-to-tension ratio on percentage of broken bonds of both bedding planes and beddings under loading condition of development (legends and marks have the same meaning as in Fig. 6- 19)

The above analysis concluded that both bedding plane strength and cohesion-to-tensile ratio posed a pronounced effect on the laminated roof response, including roof deformation, cracking mechanism, and cracking location. To identify which factor imposes a more significant effect on the roof response, we compared the variation of roof sag, unboned bond percentage of beddings, and bedding planes under development conditions as shown in Fig. 6- 23.

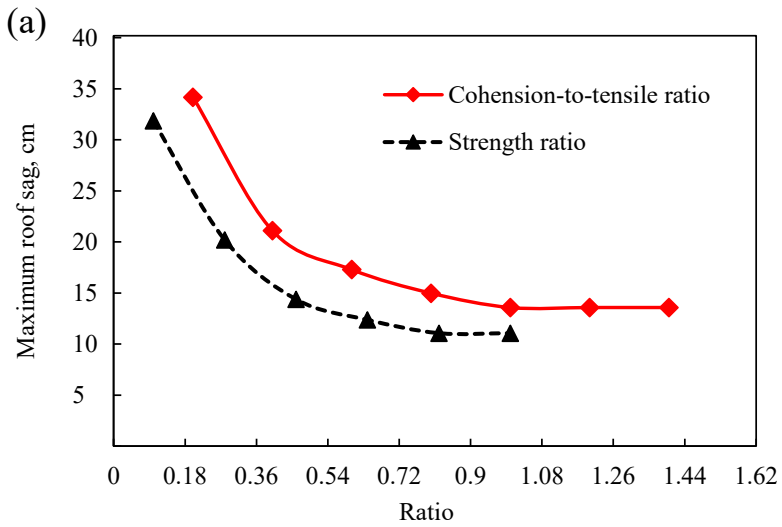

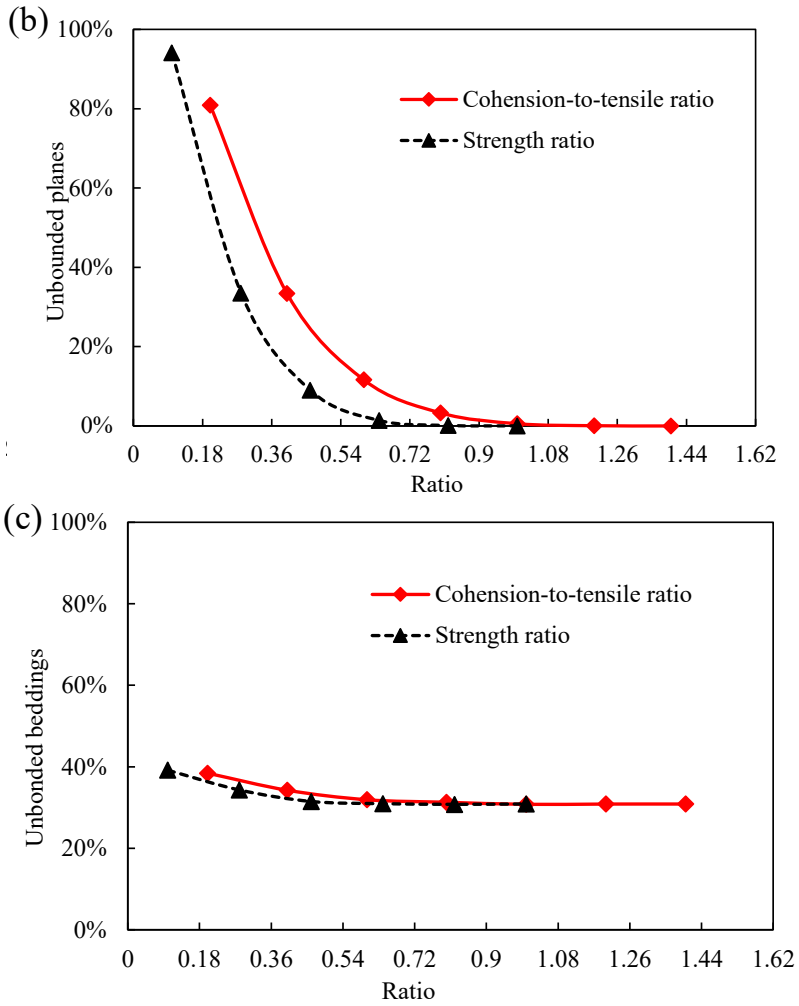

Fig. 6- 23 Comparison of (a) roof sag, (b) unbonded planes, and (c) unbonded beddings when changing bedding plane strength and cohesion-to-tensile ratio respectively under a development condition

Fig. 6- 23 shows that both curves shared a similar trend, verifying that either simultaneously reducing the cohesion and tensile strength or only reducing the cohesion changes the roof response in a similar way. However, we also observed a difference. Fig. 6- 23a shows that the curve obtained from simultaneously reducing cohesion and tensile strength is lower than that obtained by only reducing the cohesion strength, indicating that reducing the cohesion and tensile strength simultaneously decreased the roof bearing capacity more significantly than only reducing the cohesion strength of the bedding plane. When comparing Fig. 6- 23b and Fig. 6- 23c, one can observe that simultaneously reducing the bedding plane cohesion and tensile strength causes more damage in the bedding plane than reducing the cohesion only while the bedding damage does not change significantly.

6.6 Conclusions

To incorporate the effect of bedding plane properties on the laminated roof response under loading conditions caused by mining activities, we created a panel-scale model coupling DEM and FDM with PFC3D and FLAC3D respectively. This strategy achieved the mining-induced conditions required to observe laminated BPM response under a large-scale panel extraction at an affordable computational cost. The BPM presented our area of interest, laminated roof, for the convenience of observing fracturing behavior, while the continuum material replicated the rest of the model.

To validate the coupling strategy, a laboratory-scale test, the uniaxial compressive test was simulated with two distinct coupling logic, wall-zone coupling logic and ball-zone coupling logic. This study first calibrated both BPM and the continuum to match Berea sandstone behavior by comparing their Young's modulus and UCS with Berea sandstone. Then, it coupled the BPM and the continuum material. The BPM was sited in the central portion, and the continuum reproduced the rest part of the uniaxial compressive specimen. The results showed that coupling logic can simulate the rock behavior well by transferring the load applied to the continuum to the BPM. The macro stiffness played a key role in successfully achieving stress-strain consistency in these two distinct materials.

We then used the wall-zone coupling method to generate the panels-scale coupling model. We established the geological setting based on a US longwall coal mine. The model used laminated BPM incorporating beddings and bedding planes to replicate the shale roof of the monitored entries while using continuum for the rest of the panel scale model. As there is no efficient way to generate a laminated BPM replicating laminated rock as of yet, this study proposed a systematic calibration procedure to generate the laminated BPM. We then verified the coupled model by comparing its roof deformation, rib yield depth, and failed roof depth after development and panel extraction with field data. The results showed that the surrounding rock response of the coupled model agrees well with the field data.

We investigated the effect of bedding planes on the laminated roof response with the verified coupled model. This investigation changed the plane strength and cohesion-to-tensile ratio in order to observe the roof deformation, fracturing mechanism, and failure location in the laminated roof in comparison. The results show the development of the entry caused the larger roof deformation than the extraction of the panel. Increment of the bedding plane strength increases the laminated

roof strength as a whole structure, which alleviates damage to both bedding planes and broken beddings. In addition, the roof deformation is more sensitive when the bedding strength is low. Reducing the bedding plane strength also caused more shear tensile cracks in the laminated roof, and this effect is sensitive with low bedding strength. Also, observation of failure location showed that reducing the bedding plane strength increased the damage of both bedding planes and beddings by decreasing the bearing capacity of the lamination structure. Also, this effect is more sensitive when the bedding plane strength is low. Reducing the cohesion-to-tensile ratio showed a similar trend to that obtained by reducing bedding plane strength. However, simultaneously reducing the cohesion and tensile strength decreased the roof bearing capacity more significantly than only reducing the cohesion strength of the bedding plane.

CHAPTER 7 CONCLUSIONS AND RECOMMENDED FUTURE STUDIES

7.1 Conclusions

As a leading factor of roof falls in US underground coal mines, researchers have studied laminated roof failure for decades. However, limited studies are focusing on the effect of lamination properties on the failure behavior of the laminated rock/roof. Field observations indicate that bedding plane spacing and bedding plane strength can affect laminated roof failure characteristics. After excavation, cutter roof and delamination failure usually occur in the thinly laminated roof with weak bedding planes. Observations have shown that failure modes are different in the field when the bedding plane strength varies. When the bedding plane strength is weak, the failure is characterized by a nearly vertical failure plane. In contrast, a dome-shape cavity occurs when the laminas are strongly bonded by the bedding planes. However, the effect of lamination properties on the geomechanical behaviors of laminated rock/roof is much more complex than the failure modes observed in the field. This is because the geomechanical behavior of laminated rock/roof involves various rock mechanics factors, including lamination properties, cracking process, and sensitivity to stress conditions. Aiming to solve these problems, this study proposed a laboratory method to implement tests on synthetic laminated rocks with various bedding plane strengths subjected to various stress conditions, including biaxial and triaxial stress conditions. The study also observed the delamination process on a laboratory scale laminated rock. Finally, the study adopted the FDM-DEM coupling method to replicate the extraction-caused abutment pressure for the first time and investigated its influence on the geomechanical behavior of laminated roof with different lamination properties. This dissertation draws the following conclusions from the studies performed throughout this process:

- The biaxial compressive strength of synthetic laminated rock increase with the increment of their bedding plane strength.
- Increasing the bedding plane strength introduces the transition of the failure mode from typical laminated rock-like characteristics to intact rock-like characteristics. The transition includes failure pattern, failure location, and failure plane angle.

- The application of confining stress constrains the effect of bedding plane strength on the synthetic laminated rock strength and modulus. On the other hand, high confining stress crushes the grains along the bedding planes and reduce the bedding plane strength.
- The duration of the failure process before reaching the biaxial compressive strength decreased with the increase of the bedding plane strength. However, the threshold stress level to initiate failure increased with bedding plane strength.
- The laminated roof stability increased with the bedding plane strength, and the matrix that comprised the beddings determined the maximum possible strength of the laminated roof. A high bedding plane strength will develop larger stress at a fixed depth.
- Increase in the support pressure increased the strength of the laminated roof. The effect is also sensitive to bedding plane spacing.
- The delamination of an unconfined laminated rock begins on the inside beddings instead of the outer ones.
- Cutter roof propagation and delamination initiated at the intersections of the roof and ribs. Before the roof fall, separate failed zones in this specimen will form, i.e. outer failed zone and inner failed zone. These zones are separated by several intact laminas between them. The separate failed zones connect with each other as the intact laminas weaken and finally create a massive failure.
- DEM-FDM coupled simulation showed that reduction in the bedding plane strength caused more tensile cracks and decreased the bearing capacity of the laminated roof. The roof deformation, therefore, increased during the mine development, one and two-panel extraction. This effect was more sensitive when the bedding plane strength was low.

Finally, from this research it is concluded that the intrinsic influential factors significantly affect the behavior of laminated roof in underground coal mines. Based on these findings, bedding plane strength and stress conditions should be considered before designing a support system.

7.2 Recommended future studies

This study approached the geomechanical behavior of laminated rock with respect to the influence of lamination properties and stress conditions with experimental and laboratory methods, respectively. The geomechanical behaviors include strength, failure mode, deformability, and

fracturing process. The study considered these research problems at both the laboratory scale and field scale. However, several studies must occur in the future to continue this investigation.

First, researchers should use true triaxial tests to study the laminated rock behavior. This study only conducted pseudo-triaxial tests; the true triaxial stress conditions will likely result in different impacts on the laminated rock failure and its dependence on the lamination properties.

In addition, future research may develop a laboratory platen to replicate a support system applied to the synthetic laminated roof to better probe the sensitivity of the effect of lamination properties on laminated rock behavior. The bolt supporting system not only applies to confining stress to the roofline but also acts as a structure to improve bedding plane cohesion stress, which is a much more complex scenario than the triaxial platen used in this study. Therefore, a platen that can realize actual bolt support could provide more realistic data to understand the interaction of lamination properties and the support system.

Reference

Abousleiman R, Walton G, Sinha S. Understanding roof deformation mechanics and parametric sensitivities of coal mine entries using the discrete element method. Int J Min Sci Technol 2020;30:123–9. https://doi.org/10.1016/j.ijmst.2019.12.006.

Aggson JR. Coal mine floor heave in the beckley coalbed, an analysis. US Bur Mines Rep Invest 1978. https://doi.org/10.1016/0148-9062(78)91069-0.

Ai D, Zhao Y, Wang Q, Li C. Experimental and numerical investigation of crack propagation and dynamic properties of rock in SHPB indirect tension test. Int J Impact Eng 2019;126:135–46. https://doi.org/10.1016/j.ijimpeng.2019.01.001.

Amadei B. The Influence of Rock Anisotropy on the Plan of Constructions. 1982. https://doi.org/10.20431/2454-8693.0501004.

Amadei B, Goodman RE. The influence of rock anisotropy on stress measurements by overcoring techniques. Rock Mech Felsmechanik Mécanique Des Roches 1982;15:167–80. https://doi.org/10.1007/BF01240588.

Arora S., Mishra B. Investigation of the failure mode of shale rocks in biaxial and triaxial compression tests. Int J Rock Mech Min Sci 2015;79:109–23. https://doi.org/10.1016/j.ijrmms.2015.08.014.

Arora Shrey, Mishra B. Investigation of the failure mode of shale rocks in biaxial and triaxial compression tests. Int J Rock Mech Min Sci 2015;79:109–23. https://doi.org/10.1016/j.ijrmms.2015.08.014.

ASTM C192/C192M. Standard Practice for Making and Curing Concrete Test Specimens in the Laboratory. Am Soc Test Mater 2016:1–8. https://doi.org/10.1520/C0192_C0192M-19.

Bai Q, Tu S. Numerical observations of the failure of a laminated and jointed roof and the effective of different support schemes: a case study. Environ Earth Sci 2020;79. https://doi.org/10.1007/s12665-020-08935-2.

Bajpayee TS, Pappas DM, Ellenberger JL. Roof Instability: What Reportable Noninjury Roof Falls in Underground Coal Mines Can Tell Us. Prof Saf 2014;59:57–62.

Barron K, Baydusa A. A theory of cutter roof failure and its application. CIM Bull 1999;92:45–9.

Bauer E. Cutter Roof Failure: Six Case Studies in the Northern Appalachian Coal Basin. 1990.

Becker JB. A combined field, laboratory, and numerical study of cutter roof failure in Carroll hollow mine, Carroll county, Ohio. 2013.

Boresi AP, Schmidt RJ. Advanced Mechanics of Materials, Fourth Edition. New York: 1985.

Breugnot A, Lambert S, Villard P, Gotteland P. A Discrete/continuous Coupled Approach for Modeling Impacts on Cellular Geostructures. Rock Mech Rock Eng 2016;49:1831–48. https://doi.org/10.1007/s00603-015-0886-8.

Centers for Disease Control and Prevention. Mine and Mine Worker Charts. Natl Inst Occup Saf Heal 2021. https://wwwn.cdc.gov/niosh-mining/MMWC (accessed March 17, 2021).

Cherian BV V, Higgins-Borchardt S., Bordakov GA. A, Yunuskhojayev A., Al-Jalal Z., Mata D., et al. The Impact of Laminated Rock on Hydraulic Fracture Propagation in Unconventional Resources. Day 2 Tue, June 10, 2014, SPE; 2014, p. 9–11. https://doi.org/10.2118/SPE-169960-MS.

Chiu CC, Wang TT, Weng MC, Huang TH. Modeling the anisotropic behavior of jointed rock mass using a modified smooth-joint model. Int J Rock Mech Min Sci 2013;62:14–22. https://doi.org/10.1016/j.ijrmms.2013.03.011.

Chiu CC, Weng MC, Huang TH. Modeling rock joint behavior using a rough-joint model. Int J Rock Mech Min Sci 2016;89:14–25. https://doi.org/10.1016/j.ijrmms.2016.08.001.

Chong Z, Li X, Hou P, Wu Y, Zhang J, Chen T, et al. Numerical Investigation of Bedding Plane Parameters of Transversely Isotropic Shale. Rock Mech Rock Eng 2017;50:1183–204. https://doi.org/10.1007/s00603-016-1159-x.

Clifford B. The assessment of ground control risk and support integrity in coal mine roadways. 2004.

Coggan J, Gao F, Stead D, Elmo D. Numerical modelling of the effects of weak immediate roof lithology on coal mine roadway stability. Int J Coal Geol 2012;90–91:100–9. https://doi.org/10.1016/j.coal.2011.11.003.

Conshohocken W. Standard Test Method for In Situ Determination of Direct Shear Strength of Rock. vol. 90. 1995. https://doi.org/10.1520/D4554-12.

Cundall PA, Strack ODL. A discrete numerical model for granular assemblies. Géotechnique 1979;29:47–65. https://doi.org/10.1680/geot.1979.29.1.47.

Dai F, Chen R, Iqbal MJ, Xia K. Dynamic cracked chevron notched Brazilian disc method for measuring rock fracture parameters. Int J Rock Mech Min Sci 2010;47:606–13. https://doi.org/10.1016/j.ijrmms.2010.04.002.

Dou F, Wang JG, Zhang X, Wang H. Effect of joint parameters on fracturing behavior of shale in notched three-point-bending test based on discrete element model. Eng Fract Mech 2019a;205:40–56. https://doi.org/10.1016/j.engfracmech.2018.11.017.

Dou F, Wang JG, Zhang X, Wang H. Effect of joint parameters on fracturing behavior of shale in notched three-point-bending test based on discrete element model. Eng Fract Mech 2019b;205:40–56. https://doi.org/10.1016/j.engfracmech.2018.11.017.

Eichhubl P, Hooker JN, Laubach SE. Pure and shear-enhanced compaction bands in Aztec Sandstone. J Struct Geol 2010;32:1873–86. https://doi.org/10.1016/j.jsg.2010.02.004.

Einstein HH, Hirschfeld RC. Model studies on mechanics of jointed rock. J Soil Mech Found Div 1973;99:d.

Esterhuizen GS, Bajpayee TS. Horizontal stress related failure in bedded mine roofs - Insight from field observations and numerical models. 46th US Rock Mech. / Geomech. Symp. 2012, vol. 1, 2012, p. 68–77.

Esterhuizen GS, Gearhart DF, Klemetti T, Dougherty H, van Dyke M. Analysis of gateroad stability at two longwall mines based on field monitoring results and numerical model analysis. Int J Min Sci Technol 2019;29:35–43. https://doi.org/10.1016/j.ijmst.2018.11.021.

Esterhuizen GS, Tulu IB, Bajpayee TS. Application of a brittle failure model to assess roof stability in coal mine entries. 51st US Rock Mech. / Geomech. Symp. 2017, vol. 3, 2017, p. 1665–74.

Felippa CA, Park KC. Staggered transient analysis procedures for coupled mechanical systems: Formulation. Comput Methods Appl Mech Eng 1980;24:61–111. https://doi.org/10.1016/0045-

7825(80)90040-7.

Feng G, Kang Y, Wang X, Hu Y, Li X. Investigation on the Failure Characteristics and Fracture Classification of Shale Under Brazilian Test Conditions. Rock Mech Rock Eng 2020;53:3325–40. https://doi.org/10.1007/s00603-020-02110-6.

Gadde M, Peng S. Effect of in-situ stresses on the stability of coal mine development workings. Proc 23rd Int Conf Gr Control Min 2004:92–102. https://doi.org/10.33915/etd.1348.

Gadde M, Rusnak J, Honse J, Peng SS. On rock failure criteria for coal measure rocks. 26th Int. Conf. Gr. Control Mining, Morgantown, USA, 2007, p. 361–9.

Gadde MM, Peng SS. Numerical simulation of cutter roof failure under weak roof conditions. 2005 SME Annu. Meet. Got Min. - Prepr., Salt Lake City, Utah.: 2005, p. 459–69.

Gao F. Simulation of failure mechanisms around underground coal mine openings using discrete element modelling. 2013.

Gao F, Stead D. Discrete element modelling of cutter roof failure in coal mine roadways. Int J Coal Geol 2013;116–117:158–71. https://doi.org/10.1016/j.coal.2013.07.020.

Gao F, Stead D, Kang H. Simulation of roof shear failure in coal mine roadways using an innovative UDEC Trigon approach. Comput Geotech 2014;61:33–41. https://doi.org/10.1016/J.COMPGEO.2014.04.009.

Garg P. Behaviour of Laminated Roof under High Horizontal Stress. West Virginia University, 2018.

Garg P, Hedayat A, Griffiths D V. Numerical Simulation of Fracture Initiation in Barre Granite using an Experimentally Validated XFEM Model. OnePetro; 2020.

Ghabraie B, Ren G, Ghabraie K, Xie YM. A Study on Truss Bolt Mechanism in Controlling Stability of Underground Excavation and Cutter Roof Failure. Geotech Geol Eng 2013;31:667–82. https://doi.org/10.1007/s10706-013-9617-7.

Gholaminejad A, Mahboubi A, Noorzad A. Encased stone columns: coupled continuum – discrete modelling and observations. Geosynth Int 2020;27:581–92. https://doi.org/10.1680/jgein.20.00017.

Gholaminejad A, Mahboubi A, Noorzad A. Combined DEM-FDM modelling of encased stone column. E3S Web Conf 2019;92:16012. https://doi.org/10.1051/e3sconf/20199216012.

Hadi MNS, Yuan JS. Experimental investigation of composite beams reinforced with GFRP I-beam and steel bars. Constr Build Mater 2017;144:462–74. https://doi.org/10.1016/j.conbuildmat.2017.03.217.

Haeri H, Shahriar K, Marji MF, Moarefvand P. Experimental and numerical study of crack propagation and coalescence in pre-cracked rock-like disks. Int J Rock Mech Min Sci 2014;67:20–8. https://doi.org/10.1016/j.ijrmms.2014.01.008.

He C, Chen D, Xiao J, Lu L, Guo Z. Experimental study of crack propagation and failure around a horseshoe tunnel during nearby blasting. Int J Rock Mech Min Sci 2021;139:104628. https://doi.org/10.1016/j.ijrmms.2021.104628.

He J, Afolagboye LO. Influence of layer orientation and interlayer bonding force on the mechanical behavior of shale under Brazilian test conditions. Acta Mech Sin 2018;34:349–58. https://doi.org/10.1007/s10409-017-0666-7.

Hedayat A, Pyrak-Nolte LJ, Bobet A. Detection and quantification of slip along non-uniform frictional bedding planes using digital image correlation. Geotech Test J 2014;37. https://doi.org/10.1520/GTJ20130141.

Heidari M, Khanlari GR, Kaveh MT, Kargarian S. Predicting the uniaxial compressive and tensile strengths of gypsum rock by point load testing. Rock Mech Rock Eng 2012;45:265–73. https://doi.org/10.1007/s00603-011-0196-8.

Heng S, Guo Y, Yang C, Daemen JJK, Li Z. Experimental and theoretical study of the anisotropic properties of shale. Int J Rock Mech Min Sci 2015;74:58–68. https://doi.org/10.1016/j.ijrmms.2015.01.003.

Hill JL. Cutter roof failure :an overview of the causes and methods for control. Washington D.C.: USBM IC 9094; 1986.

Hoek E, Martin CD. Fracture initiation and propagation in intact rock – A review. J Rock Mech Geotech Eng 2014;6:287–300. https://doi.org/10.1016/J.JRMGE.2014.06.001.

Huo Y, Song X, Zhu D. Numerical Investigation of Top-Coal Migration in the First Coal-Drawing Process by an FDM–DEM Coupling Method. Energies 2020;13:5493. https://doi.org/10.3390/en13205493.

Indraratna B, Ngo NT, Rujikiatkamjorn C, Sloan SW. Coupled discrete element-finite difference method for analysing the load-deformation behaviour of a single stone column in soft soil. Comput Geotech 2015;63:267–78. https://doi.org/10.1016/j.compgeo.2014.10.002.

Itasca. PFC 6.00 2018.

Itasca Consulting Group I. PFC | US Minneapolis 2019.

Jaeger JC. Shear Failure of Anistropic Rocks. Geol Mag 1960a;97:65–72. https://doi.org/10.1017/S0016756800061100.

Jaeger JC. Shear Failure of Anistropic Rocks. Geol Mag 1960b;97:65–72. https://doi.org/10.1017/S0016756800061100.

Jaeger JC. The frictional properties of joints in rock. Geofis Pura e Appl 1959;43:148–58. https://doi.org/10.1007/BF01993552.

Jaeger JC, Cook NG, Zimmerman R. Fundamentals of rock mechanics, 4th edition. 2009.

Jaeger JC, Cook NG, Zimmerman R. Fundamentals of Rock Mechanics. fourth ed. Oxford: Blackwell publishing, Oxford; 2007.

Jeremic ML. Coal mine roadway stability in relation to lateral tectonic stress - western canada. Min Eng 1981;33:704–9. https://doi.org/10.1016/0148-9062(81)90605-7.

Jia L, Chen M, Jin Y, Jiang H. Numerical simulation of failure mechanism of horizontal borehole in transversely isotropic shale gas reservoirs. J Nat Gas Sci Eng 2017;45:65–74. https://doi.org/10.1016/j.jngse.2017.05.015.

Jia M, Liu B, Xue J, Ma G. Coupled three-dimensional discrete element–finite difference simulation of dynamic compaction. Acta Geotech 2020:1–17. https://doi.org/10.1007/s11440-020-01055-y.

Jin Z, Li W, Jin C, Hambleton J, Cusatis G. Anisotropic elastic, strength, and fracture properties of Marcellus shale. Int J Rock Mech Min Sci 2018;109:124–37.

https://doi.org/10.1016/J.IJRMMS.2018.06.009.

Kaiser PK, Diederichs MS, Martin CD, Sharp J, Steiner W. Underground works in hard rock tunnelling and mining. ISRM Int. Symp. 2000, IS 2000, OnePetro; 2018.

Kent FL, Coggan JS, Altounyan PFR. Investigation into factors affecting roadway deformation in the Selby coalfield. Geotech Geol Eng 1998;16:273–89. https://doi.org/10.1023/A:1008828832473.

Kushwaha A, Murali Mohan G, Singh SK, Sheorey PR. Effect of in situ horizontal stresses on roadway stability. J Mines, Met Fuels 2003;51:134–42.

Kuznetsov SV, Trofimov VA. Formation of tension and delamination areas in a long excavation's roof. J Min Sci 2012;48:789–97. https://doi.org/10.1134/s1062739148050036.

Lambert C, Coll C. Discrete modeling of rock joints with a smooth-joint contact model. J Rock Mech Geotech Eng 2014;6:1–12. https://doi.org/10.1016/j.jrmge.2013.12.003.

Li Q, Gao ZH, Xu WL, Wang K, Liu S, Ran GF, et al. Experimental research on the dynamic propagation process of mode I cracks in the rock under directional fracture blasting using the strain gauge method. Eng Fract Mech 2020;235:107113. https://doi.org/10.1016/j.engfracmech.2020.107113.

Liu G, Lu W, Lou Y, Pan W, Wang Z. Interlayer shear strength of Roller compacted concrete (RCC) with various interlayer treatments. Constr Build Mater 2018;166:647–56. https://doi.org/10.1016/J.CONBUILDMAT.2018.01.110.

Liu H, Meng X, Zhang H, Nie H, Zhang C, Li Y. The dynamic crack propagation behavior of mode I interlaminar crack in unidirectional carbon/epoxy composites. Eng Fract Mech 2019;215:65–82. https://doi.org/10.1016/j.engfracmech.2019.05.004.

Ma X, Haimson BC. Failure characteristics of two porous sandstones subjected to true triaxial stresses. J Geophys Res Solid Earth 2016;121:6477–98. https://doi.org/10.1002/2016JB012979.

Ma X, Rudnicki JW, Haimson BC. Failure characteristics of two porous sandstones subjected to true triaxial stresses: Applied through a novel loading path. J Geophys Res Solid Earth 2017;122:2525–40. https://doi.org/10.1002/2016JB013637.

Ma Y, Sheng Q, Zhang G, Cui Z. A 3D Discrete-Continuum Coupling Approach for Investigating the Deformation and Failure Mechanism of Tunnels across an Active Fault: A Case Study of Xianglushan Tunnel. Appl Sci 2019;9:2318. https://doi.org/10.3390/app9112318.

Manouchehrian A, Marji MF. Numerical analysis of confinement effect on crack propagation mechanism from a flaw in a pre-cracked rock under compression. Acta Mech Sin Xuebao 2012;28:1389–97. https://doi.org/10.1007/s10409-012-0145-0.

Mark C. Longwall mine design for control of horizontal stress. Prepr. - Soc. Min. Eng. AIME, 1991a.

Mark C. Horizontal stress and its effects on longwall ground control. Min Eng 1991b;43:1356–60. https://doi.org/10.1016/0148-9062(92)94118-b.

Mark C, Molinda GM. Development and application of the coal mine roof rating (CMRR). Proc. Int. Work. rock mass Classif. Undergr. Min., Pittsburgh, PA: 2007, p. 95–109.

Mark C, Molinda GM. Evaluating roof control in underground coal mines with the coal mine roof rating. Proc 13th Int Conf Gr Control Mining, Morgantown, WV, 1994 1994:252–60. https://doi.org/10.1016/0148-9062(95)99821-e.

Mark C, Molinda GM, Burke LM. Preventing falls of ground in coal mines with exceptionally low-strength roof: two case studies. 23rd Int. Conf. Gr. Control Min., 2004a.

Mark C, Molinda GM, Burke LM. Preventing falls of ground in coal mines with exceptionally low-strength roof: two case studies. 23rd Int. Conf. Gr. Control Min., 2004b.

Mark C, Molinda GM, Dolinar DR. Analysis of Roof Bolt Systems. 20th Int. Conf. Gr. Control Min., 2001, p. 218–25.

Mark C, Stephan RC, Agioutantis Z. Analysis of Mine Roof Support (AMRS) for US Coal Mines. Mining, Metall Explor 2020. https://doi.org/10.1007/s42461-020-00301-x.

Meyer LHI, Stead D, Coggan JS. Three dimensional modelling of the effects of high horizontal stress on underground excavation stability. 9th ISRM Congr., 1999, p. 411–6.

Molinda G, Mark C. Ground failures in coal mines with weak roof. Electron J Geotech Eng 2010;15 F:1–42.

Morgan SP, Einstein HH. The effect of bedding plane orientation on crack propagation and coalescence in shale. 48th US Rock Mech / Geomech Symp 2014 2014;3:1580–9.

Munoz H, Taheri A, Chanda EK. Pre-Peak and Post-Peak Rock Strain Characteristics During Uniaxial Compression by 3D Digital Image Correlation. Rock Mech Rock Eng 2016;49:2541–54. https://doi.org/10.1007/s00603-016-0935-y.

Murphy MM. Shale Failure Mechanics and Intervention Measures in Underground Coal Mines: Results From 50 Years of Ground Control Safety Research. Rock Mech Rock Eng 2016;49:661–71. https://doi.org/10.1007/s00603-015-0861-4.

Ngo NT, Indraratna B, Rujikiatkamjorn C. Load-Deformation Behavior of a Stone Column Using the Coupled DEM-FDM Method. Geotech. Struct. Eng. Congr. 2016 - Proc. Jt. Geotech. Struct. Eng. Congr. 2016, American Society of Civil Engineers (ASCE); 2016, p. 1618–26. https://doi.org/10.1061/9780784479742.137.

Ngo T, Indraratna B. Mitigating ballast degradation with under-sleeper rubber pads: Experimental and numerical perspectives. Comput Geotech 2020;122:103540. https://doi.org/10.1016/j.compgeo.2020.103540.

O'Sullivan C. Particulate Discrete Element Modelling. 2011. https://doi.org/10.1201/9781482266498.

Oh J, Li Y, Mitra R, Canbulat I. A Numerical Study on Dilation of a Saw-Toothed Rock Joint Under Direct Shear. Rock Mech Rock Eng 2017;50:913–25. https://doi.org/10.1007/s00603-016-1142-6.

Orford J. Alcoholism and marriage. The argument against specialism. J Stud Alcohol 1975;36:1537–63. https://doi.org/10.15288/jsa.1975.36.1537.

Park B, Min KB. Bonded-particle discrete element modeling of mechanical behavior of transversely isotropic rock. Int J Rock Mech Min Sci 2015;Complete:243–55. https://doi.org/10.1016/J.IJRMMS.2015.03.014.

Park B, Min KB, Thompson N, Horsrud P. Three-dimensional bonded-particle discrete element modeling of mechanical behavior of transversely isotropic rock. Int J Rock Mech Min Sci 2018;110:120–32. https://doi.org/10.1016/J.IJRMMS.2018.07.018.

Potyondy DO. Material-Modeling Support for PFC. Itasca Webinar: 2019.

Potyondy DO. Simulating Perforation Damage With a Flat-Jointed Bonded-Particle Material. 51st US Rock Mech. Symp. Am. Rock Mech. Assoc., American Rock Mechanics Association; 2017.

Potyondy DO, Cundall PA. A bonded-particle model for rock. 2004. https://doi.org/10.1016/j.ijrmms.2004.09.011.

Saadat M, Taheri A. A numerical approach to investigate the effects of rock texture on the damage and crack propagation of a pre-cracked granite. Comput Geotech 2019;111:89–111. https://doi.org/10.1016/j.compgeo.2019.03.009.

Sarfarazi V, Haeri H. A review of experimental and numerical investigations about crack propagation 2016;18:235–66. https://doi.org/10.12989/cac.2016.18.2.235.

Schreier H, Orteu JJ, Sutton MA. Image correlation for shape, motion and deformation measurements: Basic concepts, theory and applications. Springer US; 2009. https://doi.org/10.1007/978-0-387-78747-3.

Shan Q, Jin Y, Tan P, Zhang R. Experimental and numerical investigations on the vertical propagation of hydraulic fractures in laminated shales. J Geophys Eng 2018;15:1729–42. https://doi.org/10.1088/1742-2140/aac12f.

Sheorey PR. A theory for In Situ stresses in isotropic and transverseley isotropic rock. Int J Rock Mech Min Sci 1994;31:23–34. https://doi.org/10.1016/0148-9062(94)92312-4.

Sherizadeh T, Kulatilake PHSW. Assessment of roof stability in a room and pillar coal mine in the U.S. using three-dimensional distinct element method. Tunn Undergr Sp Technol 2016;59:24–37. https://doi.org/10.1016/j.tust.2016.06.005.

Shi C, Zhao C, Yang Y, Guo Y, Zhang X, Feng Y. Macro-meso dynamic analysis of railway transition zone: Hybrid DEM/FDM simulation and experimental validation. Soil Dyn Earthq Eng 2020;135:106191. https://doi.org/10.1016/j.soildyn.2020.106191.

Shi Q, Mishra B. Discrete Element Modeling of Delamination in Laboratory Scale Laminated Rock. Mining, Metall Explor 2020;37:1–14. https://doi.org/10.1007/s42461-020-00302-w.

Shi Q, Xu G, Wang D, Li Z, Liu W, Wang X. Chain pillar optimization at a longwall coal mine

based on field monitoring results and numerical model analysis. Arab J Geosci 2021;14:1–8. https://doi.org/10.1007/s12517-021-08843-0.

Signer SP, Jones SD. A case study of grouted roof bolt loading in a two-entry gateroad. In: Syd S. Peng, editor. 9th Int. Conf. Gr. Control Min., Morgantown, WV: 1990, p. 35–41.

Souici A, Berthet JF, Li A, Rahal N. Behaviour of both mechanically connected and bonded steel-concrete composite beams. Eng Struct 2013;49:11–23. https://doi.org/10.1016/j.engstruct.2012.10.014.

Su Wen H, Peng SS. Cutter roof and its causes. Min Sci Technol 1987;4:113–32. https://doi.org/10.1016/S0167-9031(87)90240-4.

Su Wen H, Peng SS. Cutter roof and its causes. vol. 4. 1987.

Swift GM, Reddish DJ. Underground excavations in rock salt. Geotech Geol Eng 2005;23:17–42. https://doi.org/10.1007/s10706-003-3159-3.

Tan X, Konietzky H, Frühwirt T, Dan DQ. Brazilian Tests on Transversely Isotropic Rocks: Laboratory Testing and Numerical Simulations. Rock Mech Rock Eng 2015;48:1341–51. https://doi.org/10.1007/s00603-014-0629-2.

Tran QA, Villard P, Dias D. Geosynthetic reinforced piled embankment modeling using discrete and continuum approaches. Geotext Geomembranes 2021;49:243–56. https://doi.org/10.1016/j.geotexmem.2020.10.026.

Tulu IB, Esterhuizen GS, Gearhart D, Klemetti TM, Mohamed KM, Su DWH. Analysis of global and local stress changes in a longwall gateroad. Int J Min Sci Technol 2018;28:127–35. https://doi.org/10.1016/j.ijmst.2017.11.015.

Wai Loong C, Asadul H, Ranjith PG, Akm S. Modelling of intact and jointed mudstone samples under uniaxial and triaxial compression. Arab J Geosci 2013;6:1639–46. https://doi.org/10.1007/s12517-011-0463-8.

Wang FD, Ropchan D, Sun M. Structural analysis of a coal mine opening in elastic multilayered material. 1974.

Wang F, Ropchan DM, Sun M. Structural Analysis of a Coal Mine Opening in Elastic Multilayered

Material. 1974. https://doi.org/10.1016/0148-9062(74)93198-2.

Wang F, Wang M, Mousavi Nezhad M, Qiu H, Ying P, Niu C. Rock Dynamic Crack Propagation under Different Loading Rates Using Improved Single Cleavage Semi-Circle Specimen. Appl Sci 2019;9:4944. https://doi.org/10.3390/app9224944.

Wang F, Wang M, Zhu Z, Deng J, Mousavi Nezhad M, Qiu H, et al. Rock Dynamic Crack Propagation Behaviour and Determination Method with Improved Single Cleavage Semi-circle Specimen Under Impact Loads. Acta Mech Solida Sin 2020;33:793–811. https://doi.org/10.1007/s10338-020-00186-9.

Wang X, Kang H, Gao F. Numerical study on the formation of pressure arch in bolted gravel plate. Comput Geotech 2021;130:103933. https://doi.org/10.1016/j.compgeo.2020.103933.

Wang Y, Peng SS. High horizontal stress effects on longwall gate entry stability. 15th Int. Conf. Gr. Control Min., 1996, p. 179–91.

Xi X, Wu X, Guo Q, Cai M. Experimental Investigation and Numerical Simulation on the Crack Initiation and Propagation of Rock with Pre-Existing Cracks. IEEE Access 2020;8:129636–44. https://doi.org/10.1109/ACCESS.2020.3009230.

Xiao SP, Belytschko T. A bridging domain method for coupling continua with molecular dynamics. Comput Methods Appl Mech Eng 2004;193:1645–69. https://doi.org/10.1016/J.CMA.2003.12.053.

Xing HZ, Zhang QB, Ruan D, Dehkhoda S, Lu GX, Zhao J. Full-field measurement and fracture characterisations of rocks under dynamic loads using high-speed three-dimensional digital image correlation. Int J Impact Eng 2018;113:61–72. https://doi.org/10.1016/j.ijimpeng.2017.11.011.

Xu Y, Cai M. Numerical study on the influence of cross-sectional shape on strength and deformation behaviors of rocks under uniaxial compression. Comput Geotech 2017;84:129–37. https://doi.org/10.1016/J.COMPGEO.2016.11.017.

Xu Z, Zhang L, Zhou S. Influence of encasement length and geosynthetic stiffness on the performance of stone column: 3D DEM-FDM coupled numerical investigation. Comput Geotech 2021;132:103993. https://doi.org/10.1016/j.compgeo.2020.103993.

Xue Y. Time-dependent deformation and associated failure of roof in Time-dependent deformation and associated failure of roof in underground mines underground mines. 2019.

Xue Y, Mishra B. Numerical Simulation of Size Effect of Laminated Rock. Procedia Eng., vol. 191, Elsevier Ltd; 2017, p. 984–91. https://doi.org/10.1016/j.proeng.2017.05.270.

Yang S-Q, Yin P-F, Huang Y-H. Experiment and Discrete Element Modelling on Strength, Deformation and Failure Behaviour of Shale Under Brazilian Compression 2019;52:4339–59. https://doi.org/10.1007/s00603-019-01847-z.

Yang X, Jing H, Chen K. Numerical simulations of failure behavior around a circular opening in a non-persistently jointed rock mass under biaxial compression. Int J Min Sci Technol 2016;26:729–38. https://doi.org/10.1016/j.ijmst.2016.05.027.

Yang ZY, Chen JM, Huang TH. Effect of joint sets on the strength and deformation of rock mass models. Int J Rock Mech Min Sci 1998;35:75–84. https://doi.org/10.1016/S1365-1609(98)80024-5.

Zhang J, Wang Z, Ju X, Shi Z. Simulation of flexural performance of layered ECC-concrete composite beam with fracture mechanics model. Eng Fract Mech 2014;131:419–38. https://doi.org/10.1016/j.engfracmech.2014.08.016.

Zhang K, Yang T, Bai H, Pathegama Gamage R. Longwall Mining–Induced Damage and Fractures: Field Measurements and Simulation Using FDM and DEM Coupled Method. Int J Geomech 2018;18:04017127. https://doi.org/10.1061/(ASCE)GM.1943-5622.0001040.

Zhang P, Van Dyke M, Su D, Esterhuizen E, Trackemas J. Roof failure in longwall headgates – Causes, risks, and prevention. 52nd U.S. Rock Mech. Symp., Seattle, Washington: 2018.

Zhao Y, Zhang L, Wang W, Pu C, Wan W, Tang J. Cracking and Stress–Strain Behavior of Rock-Like Material Containing Two Flaws Under Uniaxial Compression. Rock Mech Rock Eng 2016;49:2665–87. https://doi.org/10.1007/s00603-016-0932-1.

Zhou J, Zhang L, Pan Z, Han Z. Numerical investigation of fluid-driven near-borehole fracture propagation in laminated reservoir rock using PFC2D. J Nat Gas Sci Eng 2016;36:719–33. https://doi.org/10.1016/j.jngse.2016.11.010.

Zhou XP, Wang YT. Numerical simulation of crack propagation and coalescence in pre-cracked rock-like Brazilian disks using the non-ordinary state-based peridynamics. Int J Rock Mech Min Sci 2016;89:235–49. https://doi.org/10.1016/j.ijrmms.2016.09.010.

Zipf RK. Numerical modeling procedures for practical coal mine design. Proc. 41st U.S. Rock Mech. Symp. - ARMA's Golden Rocks 2006 - 50 Years Rock Mech., 2006.